FACULTY
OF MATHEMATICS
AND PHYSICS
Charles University

DOCTORAL THESIS

RNDr. Roman Tesař

Type-II thin film superconductors studied by terahertz radiation

Department of Low Temperature Physics

Supervisor of the doctoral thesis:	prof. RNDr. Ladislav Skrbek, DrSc.
Study programme:	Physics
Study branch:	4F3 – Physics of Condensed Matter and Materials Research

Prague 2018

I declare that I carried out this doctoral thesis independently, and only with the cited sources, literature and other professional sources.

I understand that my work relates to the rights and obligations under the Act No. 121/2000 Sb., the Copyright Act, as amended, in particular the fact that the Charles University has the right to conclude a license agreement on the use of this work as a school work pursuant to Section 60 subsection 1 of the Copyright Act.

In Prague, August 24, 2018

RNDr. Roman Tesař

Acknowledgements

First of all, I would like to thank my supervisor Ladislav Skrbek for his kind and patient guidance throughout the duration of my doctoral studies, and for his precious help and steady encouragement to finish the work. This work would not have been possible without support and help of my colleagues and coworkers from the Institute of Physics CAS. I am grateful to Jan Koláček for discussing various aspects of superconductivity and for his valuable advice on the topic of the presented thesis. I also want to thank Michal Šindler for performing the numerical simulations, help with transmission measurements, and for programming the data acquisition software. His collaboration with the Terahertz and ultra-fast spectroscopy group enabled to gather important experimental data, which facilitated interpretation of our FIR/THz measurements. Vít Novák is acknowledged for supplying a two-dimensional electron gas GaAs sample and Y. T. Wang from NCTU in Taiwan for providing an YBCO/LAO sample. Also the technical staff of the Institute of Physics is greatly acknowledged, M. Zíka for adapting the electronics and J. Stöckel for manufacturing a rotating analyzer mount. Workers from the mechanical workshop in FZU Cukrovarnická are commended for producing sample holders and various optics holders and adapters. Last but not least I am grateful to my family for supporting me throughout my studies.

Title: Type-II thin film superconductors studied by terahertz radiation
Author: RNDr. Roman Tesař
Department: Department of Low Temperature Physics
Supervisor: prof. RNDr. Ladislav Skrbek, DrSc.
Consultant: RNDr. Jan Koláček, CSc.

Abstract: Utilization of type-II superconductors for future practical applications such as fluxonics requires detailed knowledge of their physical properties, especially at high frequencies within the THz spectral region. We have investigated interactions of thin-film NbN samples deposited on Si substrate and of a high quality epitaxial film of the NbN superconductor grown on a birefringent R-cut sapphire substrate with monochromatic linearly polarized laser beam both below and above the critical temperature T_c. For photon energies lower than the optical gap, detailed measurements of transmission in zero field provide BCS-like temperature curves with a pronounced peak below T_c which disappears as the energy of incident radiation is increased above the gap. In externally applied magnetic fields up to 10 T oriented perpendicularly to the sample, i.e., in the Faraday experimental geometry, the temperature behavior of transmission is modified because the gap is suppressed and vanishes at the upper critical field and, additionally, the presence of quantized vortices changes the shape of the temperature curves. In the parallel Voigt geometry, significant differences are found between transmitted intensities of beams linearly polarised parallel with and perpendicular to the direction of applied magnetic field that fixes the vortex axes direction in the superconducting thin NbN film. A thorough analysis of the data, especially of the temperature and frequency dependence of the complex conductivity of the type-II superconductor has been performed in frame of the developed models, accounting for birefringent properties of the substrate. A precise polarization converting device fully tunable in a broad range of THz frequencies has been designed, developed and tested. It is now fully functioning for linear-to-circular polarization conversion and available for magneto-optical experiments with a FIR/THz gas laser source. It was used for measurements of the transmission of the circularly polarized THz beam through superconducting YBaCuO thin films in magnetic fields. The data reveal the presence of circular dichroism, most likely caused by the motion of the vortex lattice and allows one to estimate the effective vortex mass for this material.

Keywords: superconductivity, THz transmission, vortex mass, HTSC

Contents

1 Introduction

Since the discovery of superconductivity by Kamerlingh Onnes in 1911, great progress has been made both in experimental and theoretical research of this extraordinary physical phenomenon. The use of superconductors was mainly seen in the possibility of conducting electricity without loss. The breakthrough discovery of high-temperature superconductors (HTS) by Bednorz and Müller in 1986 has facilitated their employment in power engineering. Since 2008 several nitrogen-cooled superconducting lines have already been installed to transmit high power over short distances [1]. Superconducting transformers promise highly efficient and safe operation without fire and environmental risk. HTS magnets with liquid nitrogen as coolant may eventually replace low-temperature superconductor (LTS) coils in particle accelerators, thermonuclear fusion reactors, or wherever the consumption of liquid helium represents high costs. However, scientists are also looking for entirely new applications of the superconducting materials. Developing electronic elements for quantum computing based on vortex manipulation in type-II superconductors promises significant advances in the technology of the 21st century.

The concept of quantum computing appears in theory since 1980. In the last decades, the research focused on quantum gates, quantum coding, quantum algorithms, and quantum data storage is rapidly moving forward. But it is still a quantum bit (qubit) that forms the basic element of quantum electronics. Unlike a classical bit that holds either 0 or 1, the qubit can be in a superposition of both states

$$|\psi\rangle = \alpha\,|0\rangle + \beta\,|1\rangle\,, \tag{1.1}$$

where $|\alpha|^2$ and $|\beta|^2$ are probabilities that it is found in state $|0\rangle$ or $|1\rangle$, respectively. This is an essential feature inherent only to quantum-mechanical systems. As Feynman explained in his lecture in 1982, a quantum computer cannot be imitated by a classical computer, since there is a fundamental difference between them [2]. It is therefore clear that a physical representation of the quantum bit must be a quantum object. A variety of quantum systems are considered as qubit implementations, such as electron or nuclear spins, photons, quantum dots, Josephson junctions, etc. Top research in quantum electronic circuits is conducted at IBM, Intel, Google and D-Wave.[1] Figure 1.1 shows an example of superconducting quantum processors developed by Intel and Google. Most of the technologies employed are still based on superconducting Josephson junctions.

---

[1] Intel fabricated their 17-qubit chip and revealed a new 49-qubit superconducting test chip [3]. IBM provides online access to a commercial 20-qubit quantum device and develops a new generation of 50-qubit system [4]. Recently, Google has announced testing of a 72-qubit quantum processor [5]. D-Wave claims to have reached 2048 qubits, but it is doubtful whether their system is really a quantum computer [6].

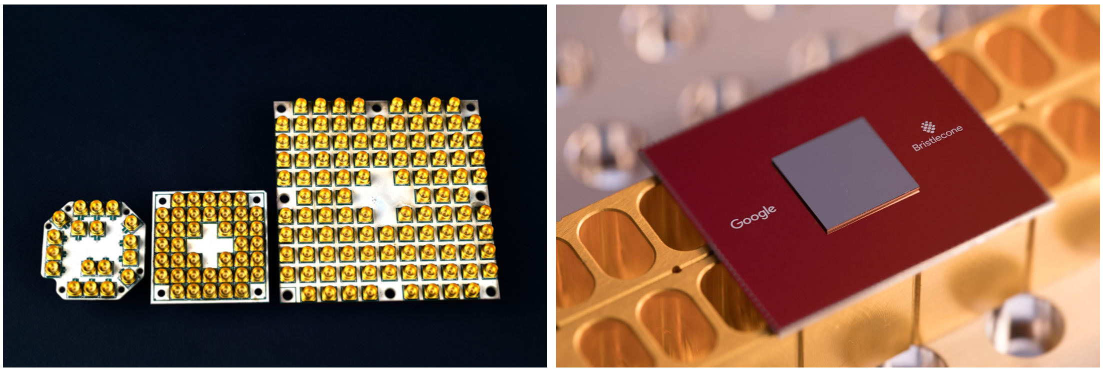

Figure 1.1: Superconducting quantum processors. Intel's chips with 7, 17 and 49 qubits (left). Google's Bristlecone 72-qubit chip (right). The pictures are taken from the official website of Intel and Google [3, 5].

The qubits are extremely sensitive to any noise or disturbance and therefore require operation at temperatures below 20 mK using a dilution refrigerator.

There are, however, other promising directions of applicability of superconductors. One example is to use the Abrikosov vortex in type-II superconductor as a suitable object for data storage [7]. This type of memory allows reading and writing information at high speeds and low power consumption. A single vortex memory cell is shown in Figure 1.2. The vortex pinned between two parallel Josephson junctions provides three distinct states: vortex (+1), antivortex (-1), and vortex free (0). Switching between the states is controlled by positive and negative current pulses that exceed a certain threshold level. Non-destructive reading of the written state is performed with an intermediate electric current. Moreover, the memory cell may be operated in a zero applied field because the vortex is generated just by a current pulse. Since the cell can carry only a quan-

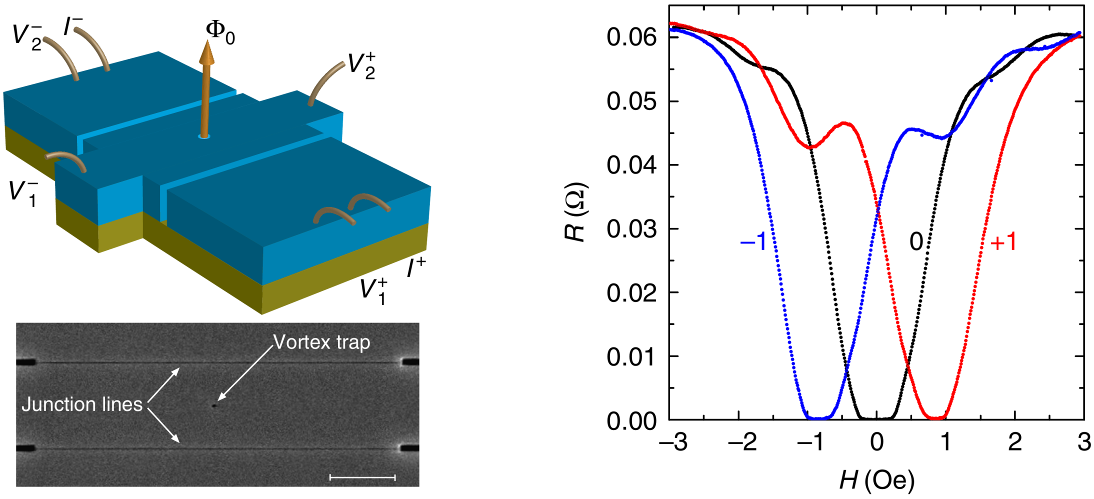

Figure 1.2: Single vortex memory cell (left) with a vortex trap and two planar Josephson junctions. The graph on the right shows the distinctly different behavior of the cell magnetoresistance in three quantum states of the memory. The pictures are taken from [7].

tized magnetic flux, it reveals a high durability and perfect reproducibility of stored information. The cell is considered as a non-volatile memory, because no extra energy is needed to maintain the data, except for the energy required to keep the low temperature of the system.

The above examples represent some important topics of *fluxonics*, a new branch of solid-state physics and engineering, based on formation, motion, and processing of quantum magnetic fluxes, which are called *fluxons*. Fluxon quantization allows to implement some functions that are almost unattainable with conventional semiconductor electronics. In addition, superconducting digital circuits can operate at very high clock frequencies with a very low power consumption due to zero resistance of superconductors [8].

There are, however, various problems that need to be solved before the practical application of fluxonics becomes a reality. In superconducting devices based on fluxon motion, the effective mass of a propagating vortex in a type-II superconductor would play an important role. Its exact value is still uncertain, and variance of several orders is reported [9–13]. Moreover, knowing how to determine the vortex mass has an overlap in other disciplines. For example, T. Simula [14] claims:

> “The inertial mass of a vortex may have relevance to many areas of physics including two-dimensional quantum turbulence, gravitational wave emission from neutron stars, topological quantum computing, and high-temperature superconductivity.”
>
> [14] T. Simula, Vortex mass in a superfluid, *Physical Review A* **97**, 023609 (2018).

The study of the Abrikosov vortex lattice by polarized terahertz radiation may contribute to deeper understanding the vortex dynamics in superconductors. Performing such experiments under well-defined laboratory conditions represents a formidable task and a challenging opportunity to contribute to the progress in utilizing the extraordinary properties of superconductors. Experimental determination of effective mass of a vortex in type-II superconductors is one of the main motivations that stimulated us to perform this work. The thesis is structured as follows. Following this short Introduction, Chapter 2 summarizes main features of superconductors, especially those of type II, where quantized vortices exist in externally applied magnetic field. Chapter 3 describes the main physical properties of electromagnetic waves, relevant to our work. In Chapter 4 we describe the experimental setup of our laboratory, and in Chapter 5 we focus on a newly designed and developed terahertz circular polarizer and verification of its functionality. Our transmission measurements, obtained results and their interpretation are described in Chapter 6, and we conclude in Chapter 7. The research presented in this thesis was published in several articles listed in the attachments. Reprints of the author’s articles relevant to the thesis are provided as attachments.

2 Superconductors

This chapter only briefly addresses some selected topics, such as the main difference between the normal and superconducting state, the structure and dynamics of quantized vortices, and the optical properties of superconductors, relevant for this thesis.

2.1 Normal and superconducting state

Some metals, such as gold, silver and copper, are good electrical conductors, but do not exhibit superconductivity even at very low temperatures. On the other hand, some materials with a slightly worse electrical conductivity become superconducting when cooled down to a critical temperature. The basic characteristics of the superconductor in its normal state is not very different from that of the normal conductor. However, after transition to the superconducting state, its properties dramatically change. Perfect dc conductivity, perfect diamagnetism, and the Meissner effect are the phenomena that cannot be observed with normal metals, but are typical manifestation of superconductivity.

As shown in Figure 2.1, the existence of the superconducting phase is restricted to a volume below the critical surface specified by the critical temperature T_c, critical magnetic field H_c, and critical electric current J_c. While in type-I superconductors the two phases are separated by a sharp boundary, in type-II there is a transitional area of mixed state, where the superconducting and normal phases coexist. It is a well-known fact that superconductivity of type-I is exhibited by some pure metals (Hg, Pb, Sn, Al, ...), but most of superconductors belong to the type-II.

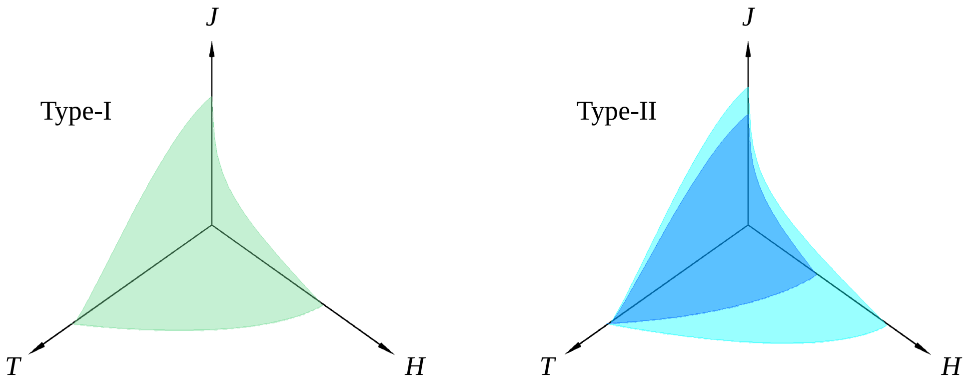

Figure 2.1: Phase diagrams of type-I and type-II superconductors. Critical surface computed from an approximate formula for the critical current [15].

There are two fundamental lengths associated with superconductivity – London penetration depth λ_{L} which describes exponential decay of magnetic field in superconductor interior, and coherence length ξ that corresponds to the shortest distance within which the macroscopic wavefunction (order parameter) can significantly alter. The ratio of the London penetration depth to the superconducting coherence length determines whether a superconductor is type-I or type-II.

$$\kappa = \frac{\lambda_{\mathrm{L}}}{\xi} = \begin{cases} < \dfrac{1}{\sqrt{2}}\,, & \text{type-I}\,, \\ > \dfrac{1}{\sqrt{2}}\,, & \text{type-II}\,. \end{cases} \tag{2.1}$$

Both ξ and λ_{L} contribute to the surface energy of superconductor. The surface energy between the normal and superconducting phase is positive when $\kappa < 1/\sqrt{2}$, while it is negative for $\kappa > 1/\sqrt{2}$. Abrikosov [16] predicted that in the case of negative surface energy, formation of cylindrical normal-state domains is energetically favorable. Therefore, in type-II superconductors, a magnetic field can partially penetrate the superconductor interior in a form of quantized magnetic flux lines called Abrikosov vortices. The mixed state of type-II superconductors exhibits two critical magnetic fields. The first, lower critical field H_{c1} occurs when vortices start to penetrate the material. The amount of vortices in the superconductor increases with increasing applied magnetic field. At the second, higher critical field H_{c2}, the vortex density becomes too large and the entire material becomes non-superconducting.

2.2 Quantized vortices and their dynamics

In isotropic superconductors, the vortices are oriented parallel to the applied magnetic field. The center of a vortex is in the normal state, while the shielding superconducting currents circulate on its outer side. The vortex radius is approximately equal to the coherence length ξ of the superconducting material. The vortices are arranged in a regular triangular array of magnetic flux lines called the Abrikosov vortex lattice. Magnetic flux that penetrates a superconductor is an integer multiple of the magnetic flux quantum

$$\Phi = BS = n\Phi_0\,, \tag{2.2}$$

where

$$\Phi_0 = \frac{h}{2e} \approx 2.067\,833\,831 \times 10^{-15}\,\mathrm{Wb} \tag{2.3}$$

is expressed via universal physical constants, the Planck constant h and the electron charge e. Number 2 in the denominator reflects the fact that the current in superconducting state is carried by Cooper pairs. Magnetic flux quantum Φ_0 is a material independent constant and represents a minimum magnetic flux which can be carried by a single Abrikosov vortex.

A magnetic hysteresis observed in type-II superconductors can be explained by a gradual penetration of vortices in its interior, for example, according to the

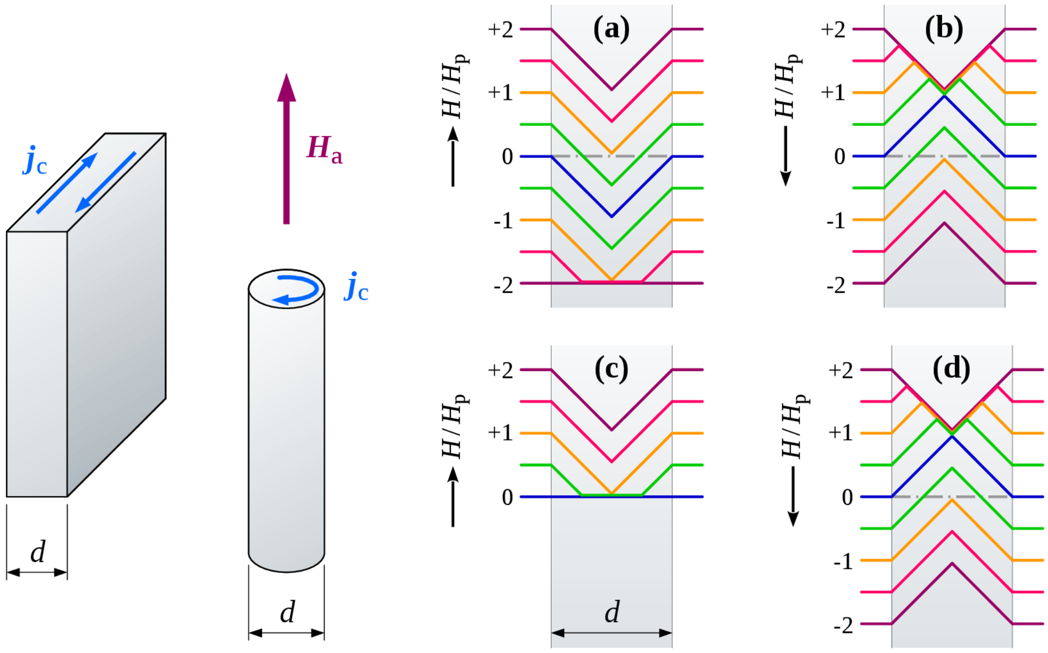

Figure 2.2: Type-II superconductor slab and cylinder in a parallel magnetic field. Screening loops are indicated by the electrical current density $\mathbf{j}_c$. The right panels show local-field profiles according to the Bean model [17, 18]. Field-cooled procedure followed by (a) increasing and (b) decreasing applied field. Zero-field-cooled procedure followed by (c) increasing and (d) decreasing applied field.

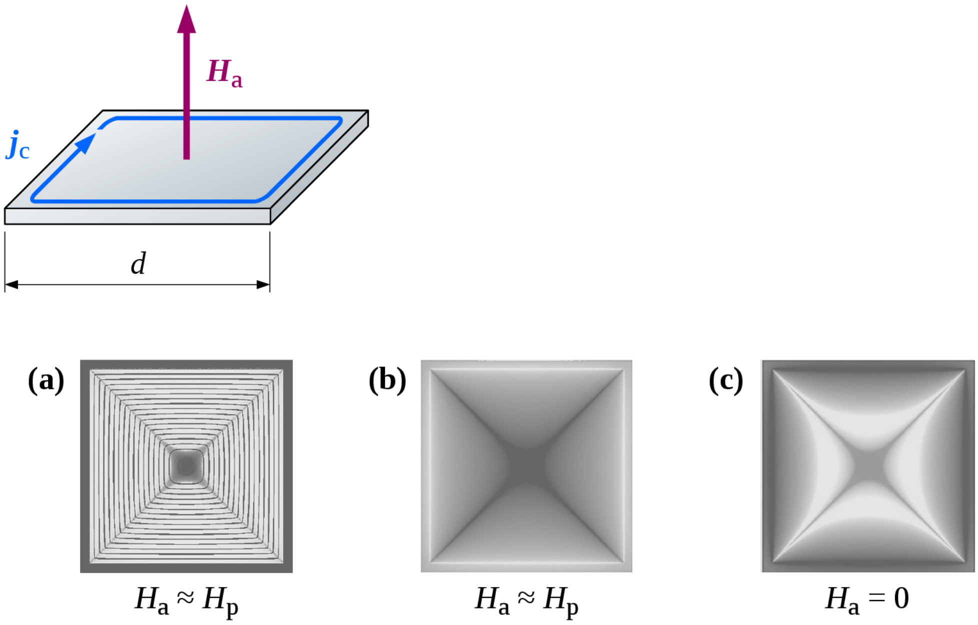

Figure 2.3: Square film of type-II superconductor in a perpendicular magnetic field. The bottom panels illustrate a nonuniform distribution of the electrical current (a) and the magnetic field (b, c) near the full penetration field (a, b) and in the subsequent remanent state (c) according to *Vestgården et al.* [19].

popular Bean model. In low magnetic fields ($H_\mathrm{a} < H_\mathrm{c1}$) the superconductor is in the Meissner state and a screening current flows below the surface. When the applied magnetic field exceeds the lower critical field H_c1, vortices begin to penetrate into the superconductor at its edge. A lossless screening current loop is formed bellow the surface with a current density j_c as shown in Figure 2.2 and 2.3. The vortices reach the center of the specimen at the so-called full penetration field H_p. When the applied magnetic field is subsequently reduced an reverse screening current is induced. In zero applied field a local remanent magnetic field is observed in the interior. Only when a reverse field is externally applied, the local magnetic field can reach zero.

In frame of the simple two-fluid model, conducting electrons are considered as a fluid composed of two fractions: a superconducting fluid with density n_s and a normal fluid with density n_n. Another structure formed in the type-II superconductors is the Abrikosov vortex lattice. All these three subsystems are subject to applied external fields and mutual interactions. Let us consider forces acting on a vortex, normal fluid and superconducting fluid. Relative motion of superconducting fluid and vortex lattice produces a transverse force, which is known as the Magnus force

$$\mathbf{F}_M^{(v)} = k_M n_s (\mathbf{v}_s - \mathbf{v}_v) \times \mathbf{z}\,, \tag{2.4}$$

where k_M is a constant, $\mathbf{v}_s$ is the velocity of the superconducting fluid, $\mathbf{v}_v$ is the vortex velocity, and $\mathbf{z}$ denotes a z-axis unit vector colinear with the vortex lines. The normal fluid slows down the vortex motion by a damping force

$$\mathbf{F}_d^{(v)} = -\eta \mathbf{v}_v\,, \tag{2.5}$$

where η is a viscosity coefficient. A pinning force proportional to a vortex displacement $\mathbf{r}_v$ may bound the vortex to a pinning center, which we write as

$$\mathbf{F}_p^{(v)} = -k_p \mathbf{r}_v\,, \tag{2.6}$$

where k_p is a pinning constant. The normal fluid component moving with velocity $\mathbf{v}_n$ in magnetic field $\mathbf{B}$ is subjected to the Lorentz force

$$\mathbf{F}_L^{(n)} = e\,(\mathbf{v}_n - \mathbf{v}_v) \times \mathbf{B}\,. \tag{2.7}$$

The flow of the normal component is damped similarly as in the Drude model by a damping force

$$\mathbf{F}_d^{(n)} = -\frac{m}{\tau_n}\mathbf{v}_n \tag{2.8}$$

where m is the electron mass and τ_n is a relaxation time.

The model of high-frequency vortex dynamics according to [20] includes mutual interactions between the subsystems based on the Newton's third law, and the equations of motion then write as

$$m\frac{\mathrm{d}\mathbf{v}_s}{\mathrm{d}t} = \mathbf{F}_M^{(s)} + e\mathbf{E}\,, \tag{2.9}$$

$$m\frac{\mathrm{d}\mathbf{v}_n}{\mathrm{d}t} = \mathbf{F}_L^{(n)} + \mathbf{F}_d^{(n)} + e\mathbf{E}\,, \tag{2.10}$$

$$m_v\frac{\mathrm{d}\mathbf{v}_v}{\mathrm{d}t} = \mathbf{F}_M^{(v)} + \mathbf{F}_L^{(v)} + \mathbf{F}_d^{(v)} + \mathbf{F}_p^{(v)}\,, \tag{2.11}$$

where **E** is electric field vector, and the reaction forces are expressed as

$$\mathbf{F}_M^{(s)} = -\frac{n_v}{n_s}\,\mathbf{F}_M^{(v)}\,, \tag{2.12}$$

$$\mathbf{F}_L^{(v)} = -\frac{n_n}{n_v}\,\mathbf{F}_L^{(n)}\,. \tag{2.13}$$

These equations are solved simultaneously and the conductivity σ can be obtained from the relation for the current density

$$\mathbf{j} = \sigma\mathbf{E} = (n_s\mathbf{v}_s + n_n\mathbf{v}_n)\mathbf{E}\,. \tag{2.14}$$

2.3 Optical properties of superconductors

Optical properties of superconductors cannot be explained by a simple two-fluid model, but a microscopic theory of superconductivity must be employed. The microscopic origin of the optical gap $2\Delta_0$ was clarified by the theory of Bardeen, Cooper and Schrieffer (BCS), which was later extended to a time-dependent electromagnetic interaction by Mattis and Bardeen. Other authors also considered contribution of impurities by introducing the electron scattering time τ. To capture the characteristics of both normal and superconducting state combining two fundamental models is inevitable. The normal state properties are conventionally described by the Drude model, while for the superconducting state the expressions obtained by *Zimmermann et al.* [21] can be adopted. The complex optical conductivity can be written as

$$\sigma(\omega,T,\tau) = \begin{cases} \sigma_\mathrm{s}(\omega,\tau,T,T_\mathrm{c},\Delta_0)\,, & \text{for } T < T_\mathrm{c}\,, \\ \\ \sigma_\mathrm{n}(\omega,\tau)\,, & \text{for } T \geq T_\mathrm{c}\,, \end{cases} \tag{2.15}$$

If we use $\exp(-i\omega t)$ convention for the time dependent part of harmonic electromagnetic waves, the normal state conductivity has the form

$$\sigma_\mathrm{n}(\omega,\tau) = \frac{\sigma_0}{1-i\omega\tau} \tag{2.16}$$

where ω is the photon frequency, σ_0 and τ is the temperature dependent dc conductivity and the relaxation rate, respectively. The expressions for evaluation σ_s are rather complicated and can be found in Ref. [21]. Relative complex permittivity, which is important for calculation of the optical properties, is in our sign convention expressed as

$$\varepsilon(\omega) = \varepsilon_\infty + \frac{i\sigma(\omega)}{\varepsilon_0\,\omega}\,, \tag{2.17}$$

where $\varepsilon_\infty \approx 1$. Figure 2.4 shows the temperature behavior of the complex conductivity calculated for several terahertz frequencies and one microwave frequency.

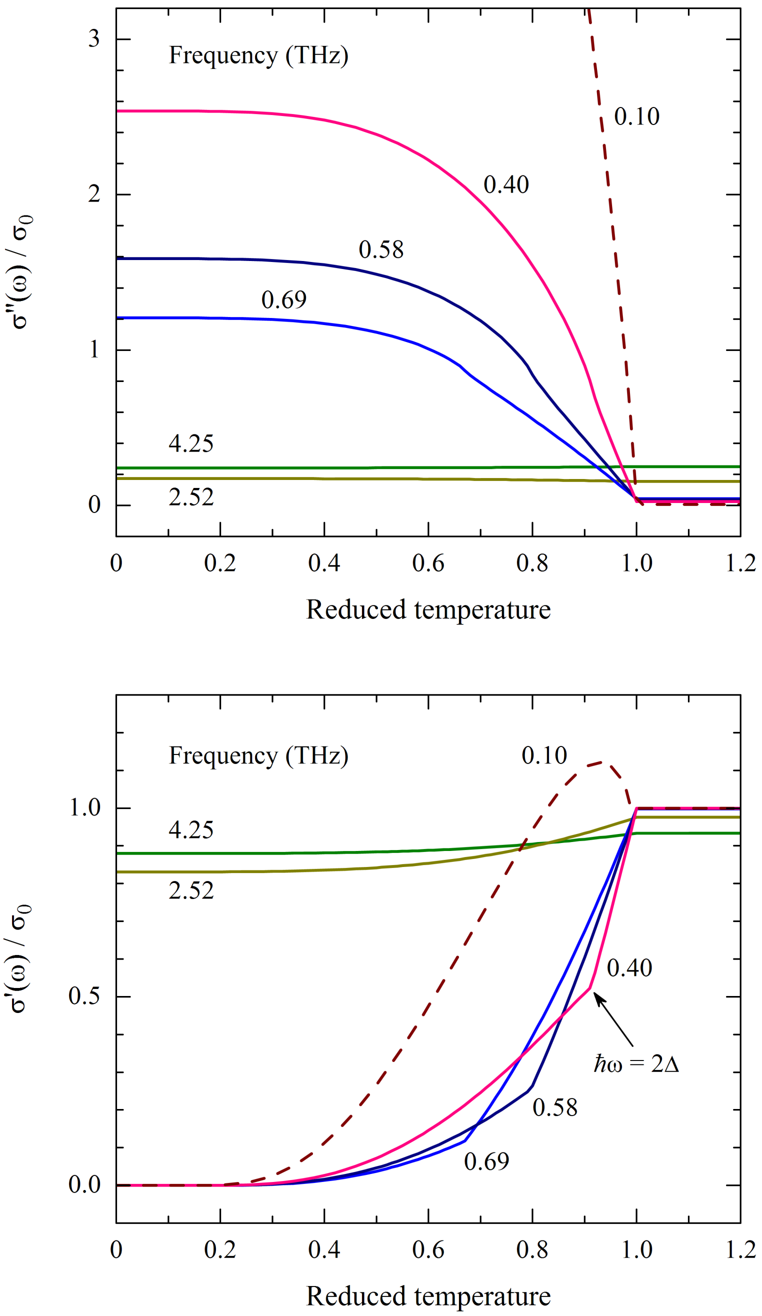

Figure 2.4: BCS complex conductivity $\sigma = \sigma' + i\sigma''$ as a function of reduced temperature T/T_c. Numerical calculation according to [21] were performed with the critical temperature $T_\mathrm{c} = 10.8\,\mathrm{K}$, normal state conductivity $\sigma_0 = 0.45 \times 10^6\,\Omega^{-1}\mathrm{m}^{-1}$, electron scattering time $\tau = 10\,\mathrm{fs}$, and BCS optical gap $2\Delta_0 = 3.53\,k_\mathrm{B}T_\mathrm{c}$.

3 Electromagnetic waves

In this Chapter, we avoid the textbook description of physical properties of electromagnetic waves and introduce only those aspects that are directly relevant to this work. The necessary conventions and quantities used at work are defined here, which is particularly important for the context of Chapter 5.

3.1 Polarization of a plane wave

Consider a polarized monochromatic plane wave of circular frequency ω traveling along the z-axis in the positive direction. The electromagnetic wave is described by the Cartesian components of the electric vector, one of which is delayed by a phase difference δ

$$\begin{aligned} E_x(t) &= E_{0x}\, e^{i(kz-\omega t)}, \\ E_y(t,\delta) &= E_{0y}\, e^{i\delta} e^{i(kz-\omega t)}, \end{aligned} \tag{3.1}$$

where E_{0x} and E_{0y} are real amplitudes,

$$k = |\mathbf{k}| = \frac{\omega}{c}\, n = \frac{2\pi}{\lambda}\, n \tag{3.2}$$

is the magnitude of the wave vector, c and λ are the speed of light and the wavelength in vacuum, and n is the refractive index of the medium. The time-dependent part $\exp(-i\omega t)$ of the electric vector (3.1) specifies the sign convention [22, 23] that is used throughout this work. In a loss medium, the wave vector as well as the refractive index are generally complex. The notation of the complex variables according to the adopted convention is then

$$\mathbf{k} = \mathbf{k}' + i\mathbf{k}'', \qquad n = n' + in'', \tag{3.3}$$

where the real and imaginary parts are designated by the prime and double prime symbols. The imaginary parts of the wave vector and refractive index are non-negative, i.e. $k'' \geq 0$ and $n'' \geq 0$.

The plane wave (3.1) has the following polarization states in relation to the phase delay δ and the real amplitudes:

$$\delta = \begin{cases} +\frac{\pi}{2} + 2m\pi,\ E_{0x} = E_{0y}, & \text{left-handed circular,} \\ -\frac{\pi}{2} + 2m\pi,\ E_{0x} = E_{0y}, & \text{right-handed circular,} \\ m\pi, & \text{linear,} \\ \text{otherwise} & \text{elliptic,} \end{cases} \tag{3.4}$$

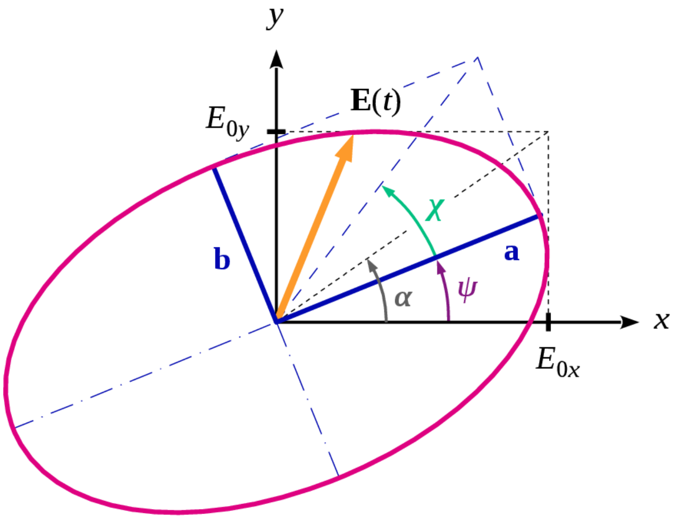

Figure 3.1: Polarization ellipse and definition of the auxiliary angle α, the orientation angle ψ, and the ellipticity angle χ.

where m is an integer number. At a certain point in the space, e.g. $z = 0$, the harmonic oscillations of the electric vector 3.1 describe a polarization ellipse in the xy-plane as indicated in Figure 3.1. Two alternative convention schemes appear in the literature to designate the sense of rotation of the electric vector [23]. Here, the observer looks in the direction of beam propagation. When the electric vector moves clockwise, the polarization is referred to as the right-handed, whereas the left-handed in the opposite case.

Further, it is convenient to introduce an auxiliary angle α, according to Figure 3.1, via a non-dimensional relative amplitude

$$\tan\alpha = \frac{E_{0y}}{E_{0x}}\,, \qquad \left(0 \leqq \alpha < \tfrac{\pi}{2}\right). \tag{3.5}$$

For a circularly polarized light, the relative amplitude is unity, and hence the auxiliary angle is 45°. Another characterization of the polarized radiation is the ellipticity, which is defined using the angle χ

$$\tan\chi = \pm\,\frac{b}{a}\,, \qquad \left(-\tfrac{\pi}{4} \leqq \chi \leqq \tfrac{\pi}{4}\right), \tag{3.6}$$

where a and b are the semi-major axis and semi-minor axis of the polarization ellipse [24]. The ellipticity of the linearly polarized wave is zero whereas it is equal to one for the circular polarization. Close to circular polarization the relative amplitude is approximately equal to the ellipticity of the polarized light

$$|\tan\chi| \approx \tan\alpha\,, \qquad \left(|\chi| \approx \alpha \approx \tfrac{\pi}{4}\right). \tag{3.7}$$

3.2 Plane waves in multilayer systems

A stack of N plane parallel layers placed between two media 0 and $N+1$ is shown in Figure 3.2. The j-th layer is characterized by its thickness d_j and refractive index n_j. Let all media be nonmagnetic materials such as $\mu_j = \mu_{\text{vac}}$. If a polarized plane wave falls upon the first layer at an angle θ_0, the angle of refraction θ_j, under which the wave propagates in the j-th layer, is given by the Snell's law. In general, both the indices and the angles of refraction may be complex numbers. Including the multiple reflections in the layers, the complex amplitudes of the reflected and transmitted waves are obtained as

$$r_{j-1} = \frac{r^F_{j-1} + r_j\, e^{2i\delta_j}}{1 + r^F_{j-1}\, r_j\, e^{2i\delta_j}}\,, \tag{3.8}$$

$$t_{j-1} = \frac{t^F_{j-1} t_j\, e^{i\delta_j}}{1 + r^F_{j-1}\, r_j\, e^{2i\delta_j}}\,, \tag{3.9}$$

where r^F_{j-1} and t^F_{j-1} are the Fresnel coefficients of the layer interface and

$$\delta_j = \frac{2\pi}{\lambda}\, n_j\, d_j \cos\theta_j\,, \tag{3.10}$$

is the phase shift introduced by the corresponding layer [25]. A specific shape of the Fresnel coefficients depends on the polarization of the incident beam. If the electric vector is orthogonal to the plane of incidence, the radiation is usually denoted as transverse-electric (TE) or s-polarized wave, whereas the designation

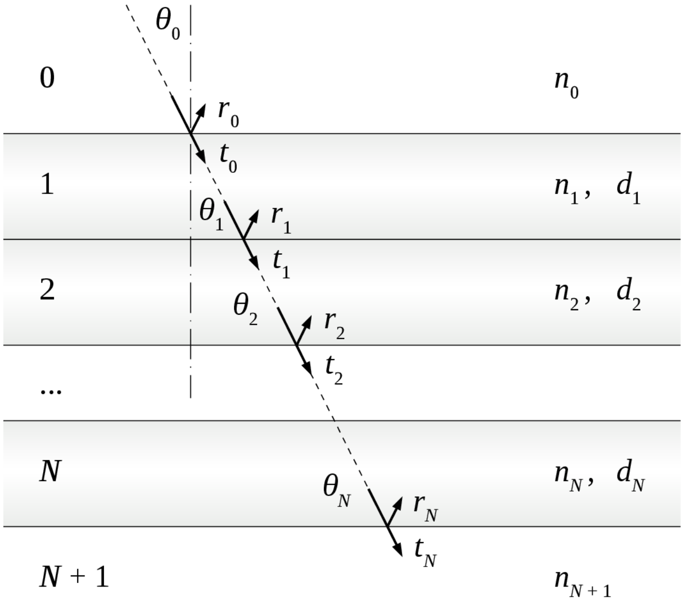

Figure 3.2: Sectional view of plane parallel layers. The arrows indicate the propagation of rays at the angles θ_j with respect to the normal to the surface. Multiple reflections between the layer boundaries are not shown for the sake of simplicity.

transverse-magnetic (TM) or p-polarized wave is used when the electric vector lies in the plane of incidence. The reflection and transmission Fresnel coefficients for the interface of nonmagnetic materials $j-1$ and j are written as

$$r_{j-1}^F = \begin{cases} \dfrac{n_{j-1}\cos\theta_{j-1} - n_j\cos\theta_j}{n_{j-1}\cos\theta_{j-1} + n_j\cos\theta_j} & (\perp, s, \mathrm{TE})\,, \\[2ex] \dfrac{n_j\cos\theta_{j-1} - n_{j-1}\cos\theta_j}{n_j\cos\theta_{j-1} + n_{j-1}\cos\theta_j} & (\parallel, p, \mathrm{TM})\,, \end{cases} \tag{3.11}$$

$$t_{j-1}^F = \begin{cases} \dfrac{2n_{j-1}\cos\theta_{j-1}}{n_{j-1}\cos\theta_{j-1} + n_j\cos\theta_j} & (\perp, s, \mathrm{TE})\,, \\[2ex] \dfrac{2n_{j-1}\cos\theta_{j-1}}{n_j\cos\theta_{j-1} + n_{j-1}\cos\theta_j} & (\parallel, p, \mathrm{TM})\,. \end{cases} \tag{3.12}$$

Evaluation of the recurrent relations 3.8 and 3.9 is performed by the Rouard's method starting from the bottom with the medium index $j = N+1$ and coefficients $r_N = r_N^F$ and $t_N = t_N^F$, and proceeding upwards to $j = 1$. The reflection and transmission coefficients of the entire layered structure are then

$$r \equiv \frac{E_r}{E_0} = r_0\,, \qquad t \equiv \frac{E_t}{E_0} = t_0\,, \tag{3.13}$$

where E_0, E_r, and E_t are complex amplitudes of the incident, reflected, and transmitted waves, respectively. When the electric vector makes an angle ϕ_0 with the plane of incidence, resolving the vector into components in plane and out of plane which are propagating independently leads to the resulting reflection and transmission coefficients

$$r = r_{0s}\sin\varphi_0 + r_{0p}\cos\varphi_0\,, \tag{3.14}$$

$$t = t_{0s}\sin\varphi_0 + t_{0p}\cos\varphi_0\,. \tag{3.15}$$

Density of the electromagnetic energy flow is given by the Poynting vector, which for the plane wave propagating in the j-th medium forward to the $(j+1)$-th medium takes a form

$$\mathbf{S}_j = \frac{1}{2}\Re\left\{\mathbf{E}_j \times \mathbf{H}_j^*\right\} = \Re\left\{\frac{\mathbf{k}_j^*}{2\mu_j\omega}\right\}\left(\mathbf{E}_j \cdot \mathbf{E}_j^*\right)\,, \tag{3.16}$$

where $\mathbf{E}_j$, $\mathbf{H}_j$, and $\mathbf{k}_j$ are the electric magnetic, and wave vectors of the beam, respectively. Projection of the Poynting vector onto the surface normal is then

$$P_j = \Re\left\{\frac{n_j\cos\theta_j}{2\mu_j c}\right\}|\mathbf{E}_j|^2\,, \tag{3.17}$$

Reflectance of the multilayer system is defined as a ratio of the reflected to incident light power

$$\mathcal{R} = |r|^2\,. \tag{3.18}$$

Transmittance is calculated in the same way, as a transmitted fraction of the incident light power. However, the real parts in 3.17 are not completely reduced so that

$$\mathcal{T} = \frac{P_{N+1}}{P_0} = \Re\left\{\frac{n_{N+1}\cos\theta_{N+1}}{n_0\cos\theta_0}\right\}|t|^2 \tag{3.19}$$

for the nonmagnetic media $j = 0$ and $j = N+1$. If the layered system is immersed in the same medium from both sides, the refractive indices n_0 and n_{N+1} are also the same, as well as the angles of the incident and transmitted beams, $\theta_{N+1} = \theta_0$, for reasons of symmetry. The transmittance is then reduced to

$$\mathcal{T} = |t|^2 \,. \tag{3.20}$$

The absorbance $\mathcal{A}$ can be evaluated from the law of conservation of energy

$$\mathcal{R} + \mathcal{T} + \mathcal{A} = 1 \,. \tag{3.21}$$

3.3 Interaction with metastructures

Properties of inhomogeneous materials may be approximated by various models. If the size of inhomogeneities is well below the wavelength of the light, or more precisely $|n|d \ll \lambda$, where n is the refractive index and d is the typical size of a local departure from homogeneity, the material may be viewed as homogeneous with an effective index of refraction n_{eff}. The simplest case is a medium composed of two homogeneous isotropic nonmagnetic materials having the relative permittivities $\varepsilon_a \neq \varepsilon_b$ and the relative permeabilities $\mu_a = \mu_b = 1$. The effective response to the electromagnetic field may be the same as for a homogeneous, albeit not necessarily isotropic, medium of relative permittivity tensor

$$\varepsilon_{\text{eff}} = \varepsilon_{\text{eff}}(\varepsilon_a, \varepsilon_b, a, b, \ldots) \,, \tag{3.22}$$

wherein its specific form stem from the geometrical configuration of the two materials. The effective refractive index is then calculated as

$$n_{\text{eff}} = \sqrt{\varepsilon_{\text{eff}}} \,, \tag{3.23}$$

Let us first consider a periodically stratified medium, as illustrated by Figure 3.3, composed of alternating thin layers of thickness a and b. Rytov [26] showed that, for sufficiently long wavelengths, this composite structure behaves as a uniaxial crystal with an optical axis perpendicular to the layers. According to his results, the approximate relations for the nonzero diagonal components of the effective permitivity tensor may be written as

$$\varepsilon_{xx} = \varepsilon_{yy} = f_a\,\varepsilon_a + f_b\,\varepsilon_b \,, \tag{3.24}$$

$$\frac{1}{\varepsilon_{zz}} = \frac{f_a}{\varepsilon_a} + \frac{f_b}{\varepsilon_b} \,, \tag{3.25}$$

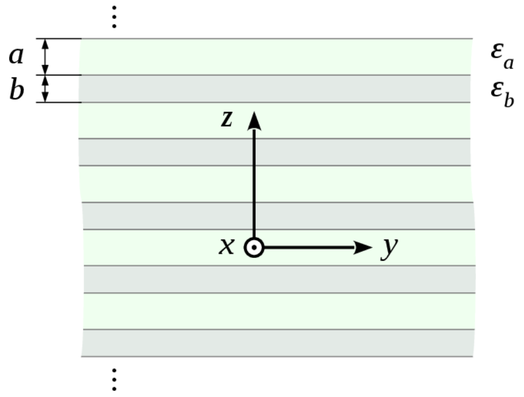

Figure 3.3: Periodically stratified medium. The x, y, z coordinates coincide with the principal axes of the composite. The optic axis is oriented in the z-direction.

where f_a and f_b denote fractions of material,

$$f_a = \frac{a}{a+b}\,, \quad f_b = \frac{b}{a+b}\,, \tag{3.26}$$

satisfy the sum rule condition

$$f_a + f_b = 1\,. \tag{3.27}$$

Another arrangement is displayed in Figure 3.4. Randomly distributed isotropic inhomogeneities are immersed in a continuous matrix medium. It is assumed that the inclusions are not percolated, and their volume fraction f_a is small compared to that of the filler f_b. Further, it is assumed that the particles are sufficiently distant from each other, so that their interactions may be neglected. The effective permittivity of such a system may be approximated by the Maxwell Garnett mixing equation [27, 28]

$$\frac{\varepsilon_{\text{eff}} - \varepsilon_b}{\varepsilon_{\text{eff}} + 2\varepsilon_b} = f_a\,\frac{\varepsilon_a - \varepsilon_b}{\varepsilon_a + 2\varepsilon_b}\,. \tag{3.28}$$

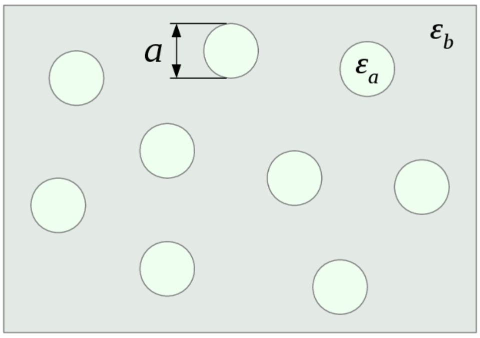

Figure 3.4: Inclusions dispersed in a homogeneous matrix medium.

whence

$$\varepsilon_{\text{eff}} = \varepsilon_{\text{MG}} = \varepsilon_b \, \frac{(1+2f_a)(\varepsilon_a - \varepsilon_b) + 3\varepsilon_b}{(1\;-f_a)(\varepsilon_a - \varepsilon_b) + 3\varepsilon_b} \,. \tag{3.29}$$

Although equation 3.28 was originally derived for spheres of the same size, the result depends on their diameter only through the volume fraction f_a. It can therefore be expected that the Maxwell Garnett theory is applicable more generally, even to inhomogeneities of nonuniform shapes and sizes randomly dispersed in the matrix. The inclusions, however, must be separated by the filler and must be small compared to the wavelength.

Bruggeman's approach is based on symmetrization of the Maxwell Garnett equation 3.28 by replacing the permitivity of the matrix medium with an effective value of the whole system, $\varepsilon_b = \varepsilon_{\text{eff}}$, and rewriting its right hand side for two types of inclusions

$$0 = f_a \, \frac{\varepsilon_a - \varepsilon_{\text{eff}}}{\varepsilon_a + 2\varepsilon_{\text{eff}}} + f_b \, \frac{\varepsilon_b - \varepsilon_{\text{eff}}}{\varepsilon_b + 2\varepsilon_{\text{eff}}} \,. \tag{3.30}$$

From two mathematical solutions of quadratic equation 3.30 only the following one is physically meaningful

$$\varepsilon_{\text{eff}} = \varepsilon_{\text{BG}} = \tfrac{1}{4}\left(\beta + \sqrt{\beta^2 + 8\varepsilon_a\varepsilon_b}\right), \tag{3.31}$$

where

$$\beta = (2\varepsilon_a - \varepsilon_b)f_a + (2\varepsilon_b - \varepsilon_a)f_b \,. \tag{3.32}$$

The Bruggeman mixing formula is invariant under the interchange of a and b media and therefore applicable for percolating inclusions when the volume fractions of both components become comparable.

The Maxwell Garnett mixing equation 3.28 may be generalized taking into account inclusions of ellipsoidal shape oriented in the same manner. If the coordinate system is chosen so that the ellipsoids have their principal axes along the x, y, and z directions, the mixing equation writes as

$$\frac{\varepsilon_{\text{eff}} - \varepsilon_b}{\varepsilon_b + L(\varepsilon_{\text{eff}} - \varepsilon_b)} = f_a \, \frac{\varepsilon_a - \varepsilon_b}{\varepsilon_b + L(\varepsilon_a - \varepsilon_b)} \,, \tag{3.33}$$

where $L = L_{xx}$, L_{yy}, L_{zz} are the ellipsoid depolarization factors for the corresponding diagonal components of the effective permittivity tensor. The depolarization factors satisfy conditions $0 \le L \le 1$ and $L_{xx} + L_{yy} + L_{zz} = 1$. Their values for some special cases of ellipsoids are listed in Table 3.1.

	L	ε_{eff}
spheres	$L_{xx} = \frac{1}{3}$	$\varepsilon_{xx} = \varepsilon_b \frac{(1+2f_a)(\varepsilon_a - \varepsilon_b)+3\varepsilon_b}{(1-f_a)(\varepsilon_a - \varepsilon_b)+3\varepsilon_b}$
	$L_{yy} = \frac{1}{3}$	$\varepsilon_{yy} = \varepsilon_{xx}$
	$L_{zz} = \frac{1}{3}$	$\varepsilon_{zz} = \varepsilon_{xx}$
long rods	$L_{xx} = \frac{1}{2}$	$\varepsilon_{xx} = \varepsilon_b \frac{(1+f_a)(\varepsilon_a - \varepsilon_b)+2\varepsilon_b}{(1-f_a)(\varepsilon_a - \varepsilon_b)+2\varepsilon_b}$
	$L_{yy} = \frac{1}{2}$	$\varepsilon_{yy} = \varepsilon_{xx}$
	$L_{zz} = 0$	$\varepsilon_{zz} = f_a \varepsilon_a + f_b \varepsilon_b$
thin disks	$L_{xx} = 0$	$\varepsilon_{xx} = f_a \varepsilon_a + f_b \varepsilon_b$
	$L_{yy} = 0$	$\varepsilon_{yy} = \varepsilon_{xx}$
	$L_{zz} = 1$	$\varepsilon_{zz} = \left(\frac{f_a}{\varepsilon_a} + \frac{f_b}{\varepsilon_b}\right)^{-1}$

Table 3.1: Depolarization factors and effective permittivity.

4 Experimental arrangement

Most of experimental results presented in this thesis is based on measurements performed in the unique experimental Laboratory of Far-InfraRed Magnetospectroscopy (FIRM) purposefully built over about a decade in the Institute of Physics CAS, Cukrovarnická street in Prague. The author of this thesis was either fully in charge or took a substantial part in subsequent developments that led to its current state, see the illustrative photo in Figure 4.1 The equipment for magneto-optical studies of thin film superconductors consists of optical, cryogenic and electronic sections. The experimental arrangement is here described in detail, except for the terahertz circular polarizer, which will be reported in a separate chapter. Although mainly commercially available components were employed to build the setup, it was necessary to adapt them to the needs of the experiment. Only the most relevant modifications, the author made to the existing instruments, are mentioned. Figure 4.2 shows a schematic drawing of the current experimental arrangement for the circular polarization transmission measurements [29]. A previously used layout can be found in [30].

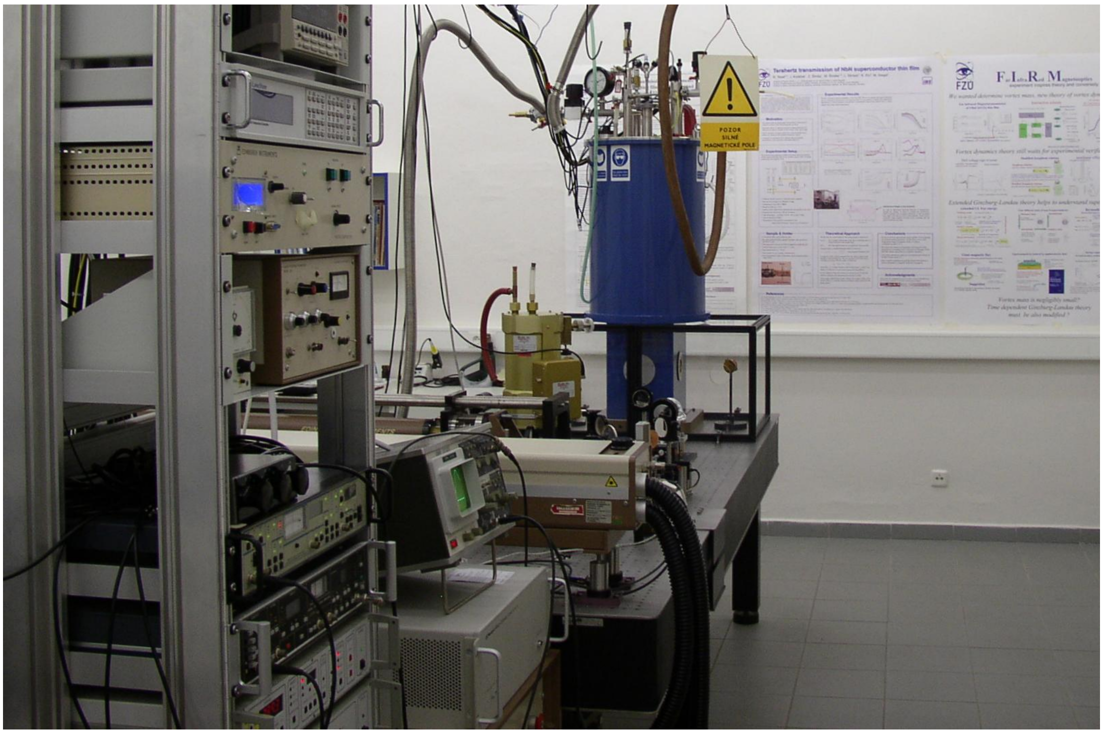

Figure 4.1: The overall view of the Laboratory of far-infrared magneto-optics with the optical helium bath cryostat in the middle.

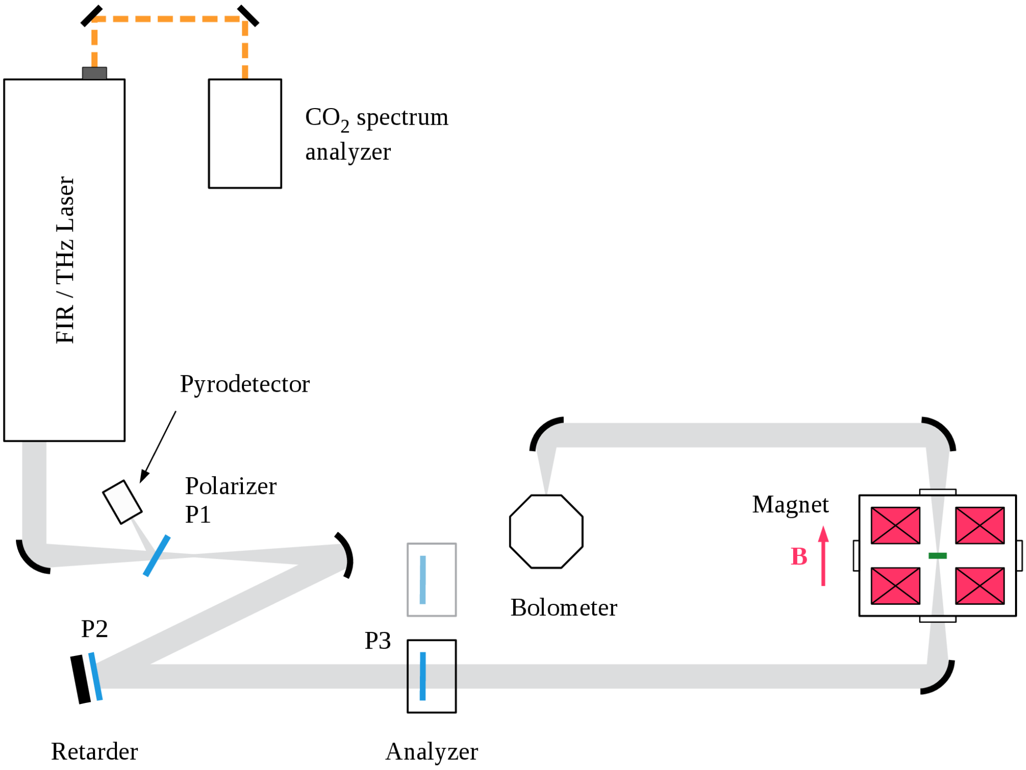

Figure 4.2: Schematic drawing of the magneto-optical experiment (not to scale). The rotating analyzer mount may be removed from the optical path as indicated by the faded colors. The scheme displays the Faraday configuration of the magnetic field. For measurements in the Voigt configuration, the magnet is swiveled by 90°.

4.1 FIR/THz laser source

An important part of the experimental setup displayed in Figure 4.2 is a FIR/THz laser, model FIRL-100 manufactured by Edinburgh Instruments Inc. The laser emits a coherent, linearly polarized, monochromatic radiation at discrete wavelengths from 40 µm up to 1.2 mm with the maximum output power about 120 mW on the strongest line. Excitation energy required for laser operation is delivered by optical pumping from a carbon dioxide laser, which is an integral component of the FIRL-100 system.

CO$_2$ section

The embeded CO$_2$ laser provides almost 80 infrared lines in two emission bands around wavelengths 9.4 and 10.4 µm corresponding to specific transitions between different vibrational modes of the CO$_2$ molecule [31]. Both vibrational bands are divided in two branches depending on the type of accompanying rotational transition. If the rotation quantum number J changes during the vibrational transition by $\Delta J = +1$, the R-branch designation is used, whereas the transitions with $\Delta J = -1$ are assigned to the P-branch. The CO$_2$ laser lines are conventionally labeled by the numbers '9' or '10', the letters 'P' or 'R', and the value of 'J' to indicate the vibrational band, the rotational branch, and the rotational quantum number of the lower state, respectively. For instance, the 9P16 label specifies transition in the P-branch of the 9.4 µm vibrational band with the lower state rotational quantum number $J = 16$.

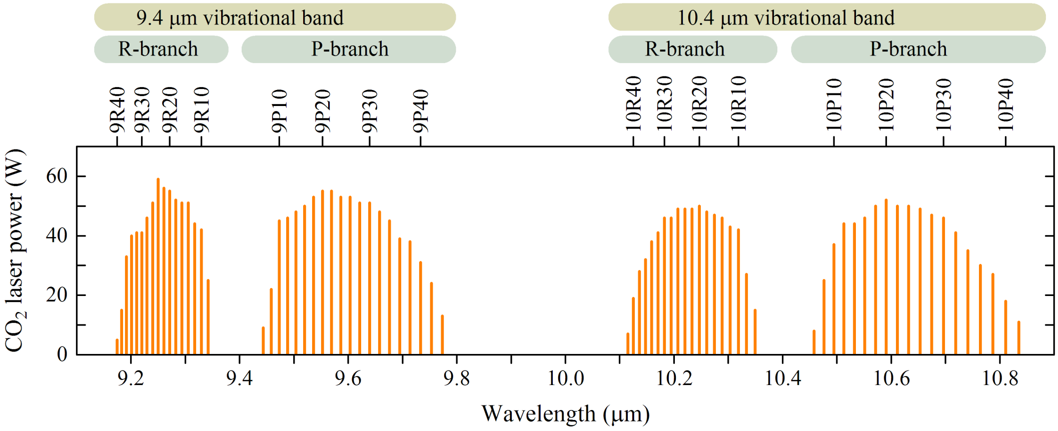

Figure 4.3: Infrared emission lines from the tunable CO_2 laser.

The CO_2 lines are selected by a water-cooled diffraction grating placed at the end of the laser cavity. The resonator length can be finely tuned by a thermally compensated piezo ceramic transducer (PZT) attached to the output coupler. The laser is fitted with ZnSe Brewster windows at both ends of a glass discharge tube to provide linear polarization in vertical direction. The laser is operated in a flow-through mode with a standard gas mixture composition of 7% CO_2, 18% N_2, and 75% He. A high voltage power supply allows modulation of the discharge current using an external signal generator with the repetition frequency up to 1 kHz. The stability of the laser output is mainly determined by the temperature stability of the cooling system, and by the stability of the current flowing through the discharge tube. When the laser is operated in the pulsed mode, it is necessary to adjust the settings of the gas pressure, discharge current, repetition rate, and pulse width, which together affect the stability of the discharge. In the continuous wave (cw) mode of operation, the maximum power is more than 50 W on the strongest lines providing optimized conditions. The output beam of the CO_2 laser is coupled into the FIR laser cavity via steering mirrors and a ZnSe focusing lens. A sliding mirror mechanism enables redirecting the CO_2 radiation outside the FIRL-100 housing for beam diagnostic purposes as indicated in Figure 4.2 by a dash line.

FIR section

Optically-pumped far-infrared lasers are based on rotation transitions of polar organic molecules in the gas phase [32, 33]. Inverse population of rotational states is achieved by absorption of infrared (IR) excitation photons with energy close to a specific vibration-rotation transition of the lasing molecules as indicated in Figure 4.4. The excited state decays in accordance with its lifetime by a pure rotational transition while emitting the energy in a form of far-infrared (FIR) photon. Subsequently, the excited molecules must dissipate their remaining energy by some non-radiative relaxation process and return to the ground state of vibrations. The FIR emission can be polarized either in parallel or perpendicular to polarization of the IR optical pumping.

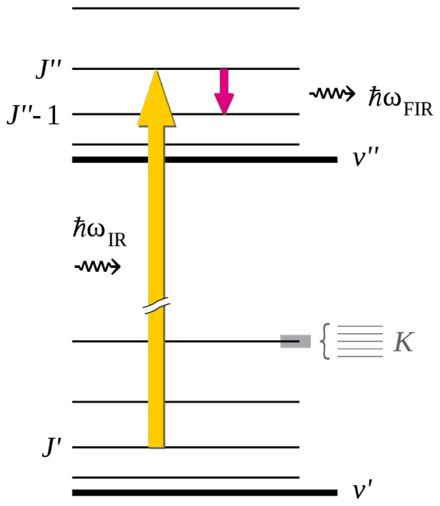

Figure 4.4: Molecular energy levels employed in the FIR laser emission. Vibrational and rotational states are denoted by quantum numbers v and J, respectively. Additional energy sublevels are only indicated regardless of other quantum numbers K, M, etc.

Extensive lists of far-infrared laser lines are available in the literature for various gases including their isotopic isomers [34, 35]. The most commonly used chemical substances are methyl alcohol and formic acid along with isotopically-substituted compounds. *Moruzzi et al.* [36] published a thorough survey of the microwave and infrared transitions of the methanol molecule CH_3OH including some theoretical aspects, experimental absorption spectra, and an updated list of 576 known methanol FIR laser lines sorted by CO_2 pump lines. There are several other reviews of far-infrared laser lines produced by methanol and its isotopomers [37–39]. Apart from methanol, some reports include also other molecules as HCOOH, CH_3F etc. [35, 40]. From more than 5000 FIR laser lines of various molecules, only a few transitions are exploited in our experiments as listed in Table 4.1.

The FIRL-100 system forms a single compact unit with some structural elements shared by both CO_2 and FIR lasers. The FIRL-100 assembly is thermally and mechanically stabilized by 5 invar rods. An integral water cooling ensures stable operating temperature of the laser tubes, cavity optics, and flowing gaseous media. The FIR subsystem is fitted with a special dichroic output coupler, which transmits the generated far-infrared radiation but blocks the CO_2 pumping frequency. The output coupler is mounted on a linear translation stage that controls the length of the FIR resonator. The stage is actuated by a micrometer screw coupled with a stepper motor shaft via a timing belt and pulley mechanism.

Several conditions must be satisfied to achieve a successful laser action. The FIR laser cavity is filled with the gain medium – an operating gas at low pressure.

The CO_2 laser is properly tuned to deliver the infrared radiation not only with photons of an appropriate pump energy, but also with a sufficiently high power above the pump threshold. The FIR resonator is scanned to find positions of constructive interference and longitudinal modes of the laser cavity. Figure 4.5 shows a typical record of the FIR cavity scanning for the FIR line 570.6 µm. When the cavity length is adjusted to satisfy the resonant condition, all other relevant settings are optimized to obtain maximum output power. Besides the optical pumping parameters, particularly the appropriate FIR gas pressure is essential.

Modification of the FIRL-100 system

The design of some FIRL-100 components by Edinburgh Instruments Inc. is rather obsolete and deserves improvement. The main weakness is the positioning system of the FIR output coupler. The stepper motor with the timing belt gear provides a sufficiently fine incremental motion of the translation stage, but with considerable backlash and no feedback. The micrometer screw is difficult to access, and visual reading of the displacement is troublesome and inaccurate. It is clear that the resonator scan as shown in Figure 4.5 can hardly be obtained in this way.

Gain medium molecule	**FIR laser line**				**Rel.† polar.**	**Rel.‡ power**	**CO_2 pump line**
	λ µm	ν THz	λ^{-1} cm^{-1}	$\hbar\omega$ meV			
CH_3OH	39.924 *	7.50910	250.5	31.1	$\perp$	M	9P34
CH_3OH	70.512	4.25167	141.8	17.6	$\perp$	VS	9P34
CH_3OH	96.522	3.10594	103.6	12.8	$\|\|$	VS	9R10
CH_3OH	118.834	2.52278	84.2	10.4	$\perp$	VVS	9P36
CH_3OH	145.252	2.06394	68.8	8.5	$\|\|$	M	10R32
CH_3OH	164.783	1.81931	60.7	7.5	$\perp$	S	9R10
HCOOH	311.554	0.96225	32.1	4.0	$\|\|$	W	10R22
HCOOH	393.631	0.76161	25.4	3.1	$\|\|$	M	9R18
HCOOH	418.613	0.71616	23.9	3.0	$\|\|$	M	9R22
HCOOH	432.631	0.69295	23.1	2.9	$\|\|$	M	9R20
HCOOH	458.523	0.65382	21.8	2.7	$\perp$	W	9R38
HCOOH	513.016	0.58437	19.5	2.4	$\|\|$	S	9R28
CH_3OH	570.569	0.52543	17.5	2.2	$\|\|$	VS	9P16
HCOOH	742.572	0.40372	13.5	1.7	$\|\|$	W	9R40
$^{13}CH_3F$	1221.79 *	0.24537	8.2	1.0	$\|\|$	W	9P32

† Relative polarization of the FIR emission with respect to the CO_2 pump polarization, i.e. parallel ($\|$) or perpendicular ($\perp$). ‡ Relative power of the FIR line expressed in a guidance scale as W = weak, M = medium, S = strong, VS = very strong, and VVS = very very strong. * Line not observed in our experimental setup.

Table 4.1: Emission lines from the FIR molecular gas laser. Further details and additional laser lines can be found in [34–40].

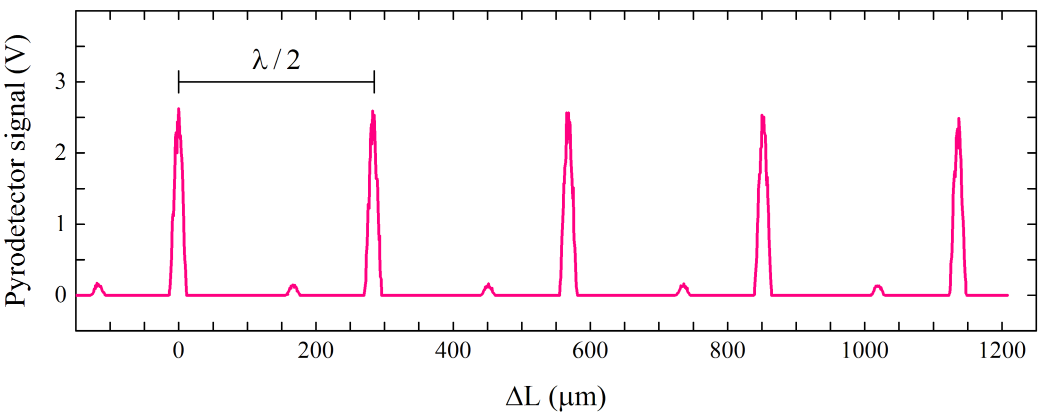

Figure 4.5: FIR cavity scan. Output power as a function of the resonator length change ΔL for the line 570.6 µm.

The problem of the missing feedback was solved by adding an independent position reading. The most suitable position sensor appears to be an absolute optical encoder from Renishaw plc, which consists of a coded scale and an ultra fast reading head. The head takes digital pictures of the code engraved on the scale, analyses the photos, calculates the current position, and transmits the result using a serial communication protocol. A unique scale pattern enables to determine the absolute position immediately after activation without homing to a reference point.

A low-expansion nickel alloy RELA scale was used for its good thermal stability and high accuracy. A piece about 20 mm long was cut off and glued directly to the stainless steel flange of the FIR output coupler. A high speed RESOLUTE readhead was attached to an adjacent invar rod and aligned with the RELA scale. The readhead does not touch the scale and therefore does not constitute any obstacle to the flange movement. The head employs the unidirectional BiSS serial protocol for fast acquiring position data, but a BiSS-USB adapter from iC-Haus GmbH is available for communication with the computer.

4.2 Optical path

Figure 4.2 displays the arrangement of the optical path using the light gray color to indicate the FIR laser beam. The beam is controlled by various parabolic, spherical, and flat mirrors. A linear wire-grid polarizer P1 defines the polarization of the radiation incident on a tunable phase retarder that is described in the next chapter as mentioned earlier. Part of the beam reflected from the polarizer is measured by a pyroelectric detector to monitor the laser power. The light reflected from the phase retarder passes through the rotating analyzer to the bolometer. The analyzer mount is attached to a sliding rail and can be easily inserted into the optical path for the phase retardance diagnostics and removed for the sample measurement. The laser beam is focused on a sample using a gold coated off-axis parabolic mirror and the transmitted radiation is collected to the

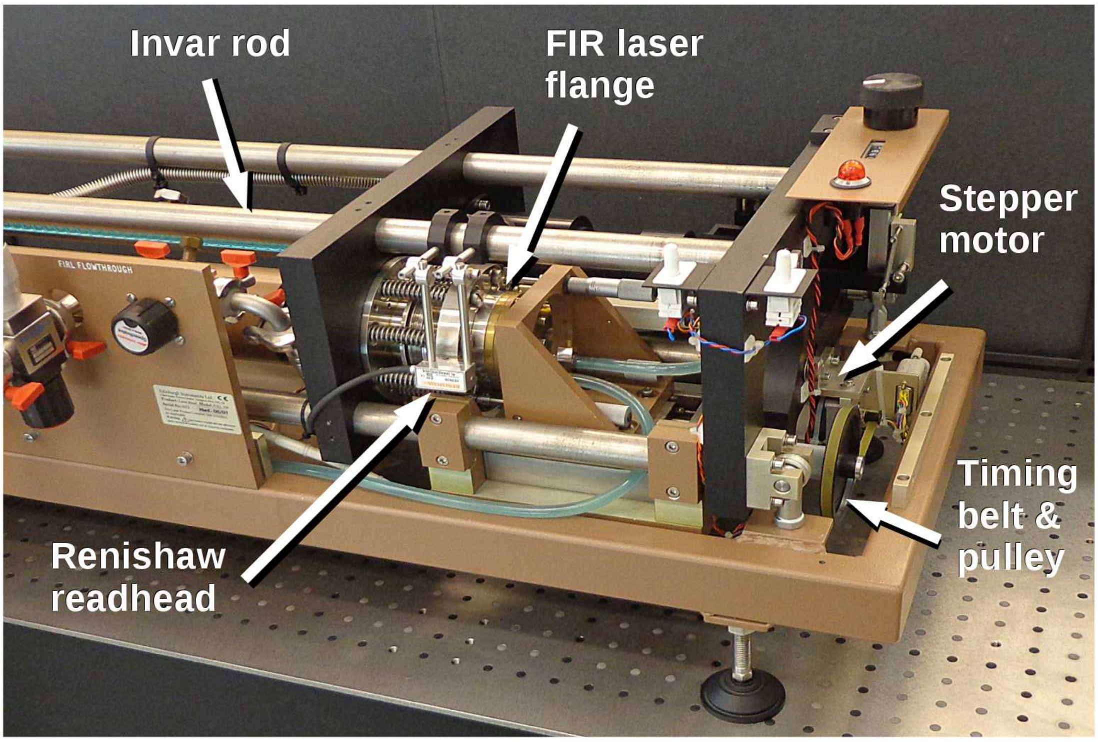

Figure 4.6: FIRL-100 without the top cover. In the foreground one can see the FIR laser, behind which is the CO_2 laser.

bolometer detector. Relative sample transmission is evaluated as the bolometer to pyrodetector signal ratio. This method effectively eliminates any possible time instability in the laser power. The relative transmission is usually normalized to some reference point on the measured curves.

There are two light detectors used in the setup, both operating on the principle of thermal detection of absorbed infrared radiation. This means that the measured quantity is the light power, not the amplitude of incident radiation. Another consequence is that modulation of the incident light is required for proper operation. The light must be chopped with a dark period long enough to allow restoring the thermal equilibrium of the radiation absorbing element. The modulated changes in temperature are converted to a voltage signal, which is measured by the lock-in detection method. The mechanism of conversion in the bolometer detector is based on temperature dependence of the electrical resistance. In the pyroelectric detector, however, the temperature dependence of electrical polarization is exploited. As already mentioned, the beam modulation is performed directly in the FIR laser source. In most experiments, a frequency of 300 Hz and a pulse width of approximately 1 ms appear to be an appropriate modulation settings.

A composite silicon bolometer from Infrared Laboratories, Inc. is an extremely sensitive helium cooled detector. The bolometer element is attached to a cold plate inside a small liquid helium dewar shielded by liquid nitrogen. The dewar is fitted with a vacuum window made of wedged polyethylene, a FIR long wave pass filter, and a Winston cone light collector with an entrance aperture of 12.7 mm.

The bolometer operates at a temperature of 4.2 K, which is ensured by thermal contact to the liquid helium bath. The first stage of the preamplifier requires an operating temperature of 60 K, whereas the second stage works at ambient temperature outside the dewar.

As shown in the upper part of Figure 4.2, the CO_2 pump beam may be redirected outside the FIRL-100 housing. For greater safety, the beam is guided within black anodized aluminum tubes and focused on the input slit of the CO_2 Laser Spectrum Analyzer from Macken Instruments, Inc. The spectrum analyzer is a simple calibrated grating spectroscope, which displays a dark bar on a thermal sensitive screen illuminated by a UV lamp. A calibrated scale attached to the screen enables identification of the CO_2 rotational-vibrational laser transitions between 9.1 and 11.3 µm. This information is sometimes very important for verification of the IR pumping frequency when tuning the FIR laser line.

4.3 Cryogenic section

The sample is placed in the Spectromag SM4000-11 from Oxford Instruments plc, an optical cryostat with a split pair of superconducting coils cooled by liquid helium. The design of the superconducting magnet enables magneto-optical measurements in both Faraday and Voigt configurations. This alternation, however, requires turning the cryostat by 90 degrees. For an easy change of the field configuration, a simple non-magnetic rotation base was fabricated from two epoxy fiberglass plates and a brass slide bearing. Two pairs of optical windows provide access to the sample in directions parallel and perpendicular to the horizontally oriented magnetic field. The mylar window material is transparent in a wide range of infrared and far-infrared wavelengths. A sliding sample rod allows manual translation of the sample in the vertical direction and rotation around the vertical axis. The superconducting coils may be energized in both field polarities using a bipolar current source. The magnet provides field up to 10 T and maximum sweep rate of 1 T/min in normal operation mode. Enhanced field of 11 T is achievable with a lambda point refrigerator.

The sample temperature can be controlled from 3 K to 300 K by a dynamic cooling and heating. Liquid helium flows from the main bath through a needle valve and evaporates in a heat exchanger at the bottom of the sample space. A flow rate of helium vapor can be dynamically adjusted via a temperature controller or set manually to a constant value. Experience shows that the constant flow rate guarantees more stable cooling conditions. A copper block near the sample holder is fitted with a resistor heater and a field independent Cernox temperature sensor for an accurate temperature control and measurement.

Various non-magnetic optical sample holders are available from Oxford Instruments Inc. The holders are made of oxygen-free high thermal conductivity copper and electroplated with rhodium for surface hardening and better corrosion resistance. However, the hole diameters are larger than the usual sample dimensions of 10 × 10 mm and therefore manufacturing of cover plates with apertures of 8 mm or less is required. A special holder was designed to monitor the dc

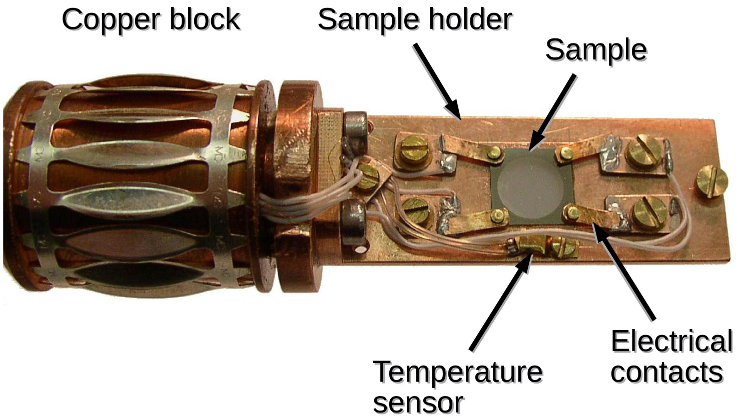

Figure 4.7: Home-made sample holder with four electrical contacts.

resistance of the sample simultaneously with the transmission measurement. An additional calibrated Cernox temperature sensor can be placed very close to the sample as shown in Figure 4.7. The electrical leads of the sensor are thermally anchored on the sample holder and on the sample rod. An Apiezon N grease is recommended to improve thermal contacts at cryogenic temperatures. A small amount of Apiezon N should always be used for a better heat transfer when joining the copper block and the sample holder. The grease is usually applied in a thin layer just to fill the unevenness of the adjacent surfaces. Apiezon N can also be used in a small area at the corners of the sample substrate. The grease is readily removable in non-polar hydrocarbon solvents such as n-hexan, n-heptan, etc. A good thermal contact is helpful for a reliable measurement of sample temperatures below 20 K where the thermal diffusivity of the helium exchange gas becomes considerably small compared to the pure copper.

5 Terahertz circular polarizer

As already mentioned in the Introduction, the study of Abrikosov vortex lattice by polarized terahertz radiation may contribute to deeper understanding the vortex dynamics in superconductors. Performing such experiments under well-defined conditions requires an effective and reliable control of the polarization states. This chapter presents detailed description of design and construction of a wire-grid terahertz circular polarizer together with an original tuning method based on the lock-in signal analysis. A theoretical signal of a dual-phase lock-in amplifier is derived and compared to experimentally acquired data. The main sections of the chapter include, with some minor changes, the author's work submitted to *Review of Scientific Instruments* [29].

5.1 Polarization conversion methods

In many optical and magneto-optical experiments, various types of polarizers are employed to ensure the conversion of light into a predetermined polarization state. A common task is to create circularly polarized light from a linearly polarized laser beam. This can be achieved by introducing a phase delay of odd multiples of $\pi/2$ between two perpendicular Cartesian components of the electric vector. Although a conventional quarter-wave plate [24] is suitable for this purpose, its use is limited to a narrow spectral line for which it has been designed. This disadvantage is partially eliminated by achromatic quarter-wave plates fabricated from several layers of different birefringent materials, which exhibit compensated dispersion and approximately constant retardance in a broader spectral range [41]. A promising technique of manipulating the polarization state is the exploitation of remarkable properties of metamaterials. It has been shown that a helix-structured metamaterial transmits one orientation of circular polarization, whereas the other one is blocked [42]. Various other conventional and unconventional methods have been suggested to generate circularly polarized terahertz waves [43–61]. Some of these techniques provide polarization states that are well circular within a narrow band around the design frequency, while others yield rather elliptic polarization over a broad band.

Linear to circular polarization conversion, however, can be achieved in a much simpler way, even in a broad bandwidth. An example is a circular polarizer composed of a wire-grid linear polarizer and a translation mirror which provides a continuously tunable phase retardance [43–51]. The first devices have been developed for experiments in the millimeter waves where a free-standing wire grid driven by a manual micrometer screw provides sufficient performance and accuracy. With decreasing wavelengths, it is necessary to reduce the diameter and spacing of the wires. Towards the far-infrared (FIR), mid-infrared, and beyond, one can reach a size limit where the fabrication of wires is extremely difficult without a supporting substrate. The presence of an additional support layer, however, dramatically alters the response of the system so that reliable checking of the adjusted polarization state becomes inevitable. Although the theoretical principle of the circular polarizer has long been known, a number of questions arise in its practical application that require a careful analysis of the problem. We therefore cover both the theoretical background and the experimental procedures necessary for successful operation of such an apparatus. The proposed approach allows for use wire grids deposited on a substrate instead of expensive and fragile free-standing grids, and, moreover, enables to extend the function of the device to shorter wavelengths.

5.2 Wire-grid phase retarder

Let us first discuss a simplified case which helps us understand how the phase delay may be controlled. We consider the configuration of a free-standing wire-grid linear polarizer with a parallel flat mirror at a distance d behind it. We assume that the grid exhibits perfect reflectance and transmittance along two orthogonal axes, and there is no interference between the grid and the mirror. Let a linearly polarized plane wave fall onto the grid at an angle of θ_0. If the direction of polarization forms an angle α_0 with the wires, the electric vector is resolved into two orthogonal components, as shown in Figure 5.1, and the incident wave is divided into two independent waves, which can be treated separately. The wave with the component parallel with the wires is reflected from the metallic surface while the other wave freely proceeds to the mirror and after reflection it propagates back and leaves the grid with a phase delay of

$$\delta = \frac{2\pi}{\lambda} 2d \cos\theta_0 \,. \tag{5.1}$$

The electric vector of the plane wave emerging from the phase retarder may be written in the complex components (3.1) and the phase difference δ adjusted by the retarder gives the resulting polarization state according to (3.4). In the ideal case we have described, there is no absorption and no phase difference in the

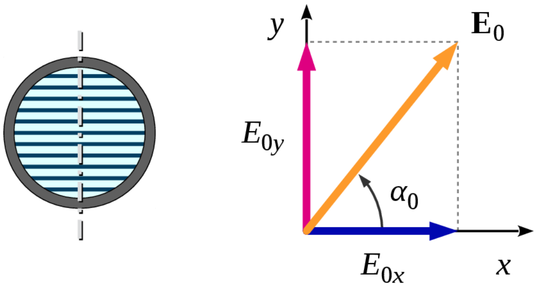

Figure 5.1: Resolution of the electric vector into reflected and transmitted components at the wire-grid polarizer. The transmission axis of the polarizer is orthogonal to the wires and is shown dot-dashed.

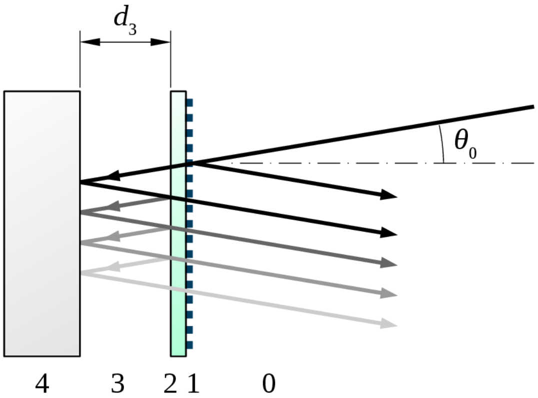

Figure 5.2: Schematic drawing of the wire-grid phase retarder: 0, 3 – free space; 1, 2 – linear polarizer (1 – wire grid, 2 – HDPE substrate); 4 – gold mirror; θ_0 – angle of incidence. For the sake of simplicity, multiple reflections are drawn only between the substrate and mirror interfaces.

electric vector components except that given by the variation in the optical path $2d\cos\theta_0$. The relative amplitude (3.5) remains unaffected, and the angles α and α_0 are identical.

We now consider a more realistic description, which involves optical properties of the wire-grid polarizer along with multiple reflections in the system. The structure of the phase retarder is shown schematically in Figure 5.2. We suppose that the wires are deposited on a transparent substrate of defined thickness and refractive index; the substrate is separated from the metal mirror by a distance d_3. The reflection coefficients r_x and r_y of the layered system are calculated independently for each component of the electric vector

$$E_{0x} = |r_x|\, E_0 \cos\alpha_0\,, \tag{5.2}$$

$$E_{0y} = |r_y|\, E_0 \sin\alpha_0\,, \tag{5.3}$$

where α_0 is the angle included by the wires and the electric vector $\mathbf{E}_0$ of the incident beam. The phase difference between the components is then

$$\delta = \arg\left(\frac{r_y}{r_x}\right) = -i\ln\left(\frac{r_y}{r_x}\frac{|r_x|}{|r_y|}\right)\,. \tag{5.4}$$

A simple way to obtain the reflection coefficients is to use the reiterative formula (3.8). The refractive indices of the materials related to the individual layers are available in the literature [62, 63]. The wire-grid, however, shows an optical anisotropy, which may be characterized by a couple of refractive indices n_{1x} and n_{1y}. There are several ways to estimate them from the effective medium theory as shown in Section 3.3. However, care must be taken to select the correct coordinate system. Obviously, the refractive index along the reflecting axis n_{1x} will result in values typical for metallic materials, whereas the index along the transmitting axis n_{1y} will be more like dielectric.

5.3 Rotating analyzer

If we place an analyzer between the phase retarder and the detector, only the projection of the electric vector (3.1) on the polarization axis is transmitted [24] as shown in Figure 5.3

$$E(t,\theta,\delta) = \left[E_{0x}\cos\theta + E_{0y}e^{i\delta}\sin\theta\right] e^{i(kz-\omega t)}, \tag{5.5}$$

Intensity of the transmitted light is then

$$\begin{aligned} I(\theta,\delta) = |E(t,\theta,\delta)|^2 = \\ = E_{0x}^2\cos^2\theta + E_{0y}^2\sin^2\theta + 2E_{0x}E_{0y}\cos\theta\sin\theta\cos\delta. \end{aligned} \tag{5.6}$$

When the analyzer rotates with angular frequency Ω, the intensity depends on time through the angle θ as

$$\theta(t) = \Omega t. \tag{5.7}$$

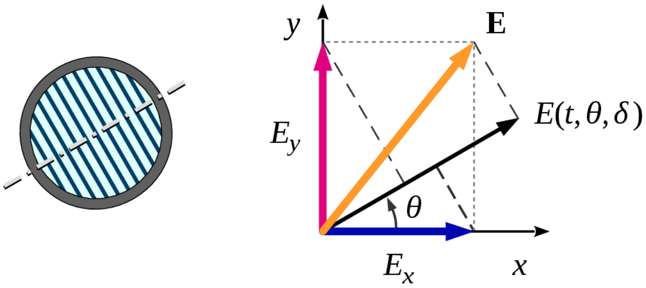

Figure 5.3: Projection of electric vector components on the transmitting axis of the analyzer (dot-dashed).

The exact value of the phase delay δ introduced by the retardance device is not always known, but it is evident that it can be determined directly from the light intensity measurement at several values of the analyzer angle θ using equation (5.6). Such a procedure is, however, not very suitable for accurate tuning of the desired retardance. Instead, a method is proposed for scanning δ and analyzing the lock-in amplifier signal. The phase delay is considered to be an independent variable controlled by the position of the translation mirror. As we will see later, for a real device the relationship between δ and mirror displacement is monotonic, albeit not necessarily linear. Moreover, the measured distance could be biased by an unknown offset. The rotating analyzer generates an alternating signal which is recognized by the phase-sensitive detection method. Scanning the mirror distance and analyzing the lock-in amplifier output offers possibility of accurate adjustment of the phase retardance δ as described in the following sections.

5.4 Lock-in signal analysis

As mentioned earlier, modulation of the light is indispensable for successful application of the phase-sensitive detection method [64]. We consider a response to the analyzer rotation only on fundamental and higher harmonic frequencies equal to $\Omega_{\rm L} = n\Omega$ $(n = 1, 2, 3, ...)$. Using a dual phase lock-in amplifier, we obtain a signal vector via two orthogonal components, *in-phase* and *quadrature*

$$X_{\rm L} = \lim_{T\to\infty} \frac{1}{T}\int_0^T \sin(n\Omega t + \phi_{\rm L})\, I(\theta(t), \delta)\,{\rm d}t\,, \tag{5.8}$$

$$Y_{\rm L} = \lim_{T\to\infty} \frac{1}{T}\int_0^T \cos(n\Omega t + \phi_{\rm L})\, I(\theta(t), \delta)\,{\rm d}t\,, \tag{5.9}$$

where $\phi_{\rm L}$ is the adjustable phase angle and $I(\theta(t), \delta)$ is the modulated light intensity (5.6). In practice it is necessary to perform the integration over a sufficiently long time interval which spans several cycles so that $\Omega T \gg 1$. Exact evaluating of the signal components above requires a careful treatment of indeterminate forms. Most of the terms vanish in the long time limit except for those containing expressions

$$\frac{\sin[\phi_{\rm L} + (n-2)\Omega T] - \sin\phi_{\rm L}}{(n-2)\Omega T} = \begin{cases} \mathcal{O}(T^{-1}) & \text{for } n \neq 2\,, \\ \cos\phi_{\rm L} & \text{for } n = 2\,, \end{cases} \tag{5.10}$$

$$\frac{\cos[\phi_{\rm L} + (n-2)\Omega T] - \cos\phi_{\rm L}}{(n-2)\Omega T} = \begin{cases} \mathcal{O}(T^{-1}) & \text{for } n \neq 2\,, \\ -\sin\phi_{\rm L} & \text{for } n = 2\,, \end{cases} \tag{5.11}$$

where the symbol $\mathcal{O}$ denotes the asymptotic behavior of a function. As the averaging time T approaches infinity, these terms provide non-zero values only for $n = 2$. The components of the resulting signal detected on twice the fundamental frequency $\Omega_{\rm L} = 2\Omega$ are of the form

$$X_{\rm L} = \frac{1}{4}(E_{0x}^2 - E_{0y}^2)\cos\phi_{\rm L} - \frac{1}{2}E_{0x}E_{0y}\sin\phi_{\rm L}\cos\delta\,, \tag{5.12}$$

$$Y_{\rm L} = \frac{1}{4}(E_{0x}^2 - E_{0y}^2)\sin\phi_{\rm L} + \frac{1}{2}E_{0x}E_{0y}\cos\phi_{\rm L}\cos\delta\,. \tag{5.13}$$

These relations contain both the variable phase difference δ introduced by the retarder and the arbitrary phase shift $\phi_{\rm L}$ between the signal and reference channels of the lock-in amplifier. Rewriting the signal vector in polar coordinates

$$R_{\rm L} = \sqrt{X_{\rm L}^2 + Y_{\rm L}^2}\,, \tag{5.14}$$

$$\tan\Theta_{\rm L} = \frac{Y_{\rm L}}{X_{\rm L}}\,, \tag{5.15}$$

the $\phi_{\rm L}$ parameter completely disappears in the expression for the signal magnitude

$$R_{\rm L} = \frac{1}{4}\sqrt{(E_{0x}^2 - E_{0y}^2)^2 + 4E_{0x}^2E_{0y}^2\cos^2\delta}\,, \tag{5.16}$$

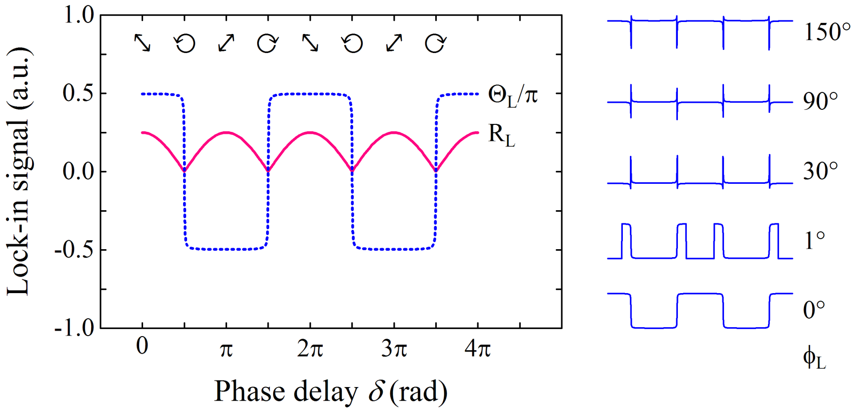

Figure 5.4: Theoretical lock-in signal as a function of phase retardance δ. The magnitude R_L and phase angle Θ_L of the signal vector were calculated for the relative amplitude $\tan\alpha = 0.99$ and the lock-in phase $\phi_\mathrm{L} = 0$. The right panel shows Θ_L for several values of ϕ_L.

but it remains in the expression for the signal angle

$$\tan\Theta_\mathrm{L} = \frac{(E_{0x}^2 - E_{0y}^2)\sin\phi_\mathrm{L} + 2E_{0x}E_{0y}\cos\phi_\mathrm{L}\cos\delta}{(E_{0x}^2 - E_{0y}^2)\cos\phi_\mathrm{L} - 2E_{0x}E_{0y}\sin\phi_\mathrm{L}\cos\delta}\,. \tag{5.17}$$

Let's see how the polarization states could be determined from the measured curves. In the case when the real amplitudes of the electric vector are mathematically equal, $E_{0x} = E_{0y}$ and $\tan\alpha = 1$, which is desirable for a circular polarization adjustment, but hardly achievable experimentally, we get a constant signal angle

$$\Theta_\mathrm{L} = \arctan(-\cot\phi_\mathrm{L}) = \phi_\mathrm{L} - \frac{\pi}{2}\,. \tag{5.18}$$

In Figure 5.4 we plot the theoretical lock-in signal as a function of retardance δ for the amplitudes close to the condition of circular polarization ($\tan\alpha = 0.99$). It is obvious that the signal magnitude is periodic and oscillates between the maximum and minimum values:

$$R_{\mathrm{L,max}} = \frac{1}{4}(E_{0x}^2 + E_{0y}^2)\,, \tag{5.19}$$

$$R_{\mathrm{L,min}} = \frac{1}{4}|E_{0x}^2 - E_{0y}^2|\,. \tag{5.20}$$

We note that the magnitude function reaches its minimum at odd multiples of $\pi/2$, while the phase angle undergoes a sharp change of sign. Those are exactly the points for which the light is circularly polarized, however, left or right handedness cannot be uniquely identified if we are not able to assign the absolute values of δ to them because of unknown instrumental offset. The shape of the phase angle curve strongly depends on the arbitrary parameter ϕ_L, as illustrated in the right panel of Fig. 5.4, so this signal component is not very helpful. In spite of that, the magnitude itself provides enough information to distinguish between the linear, circular and elliptic polarization states. As can be seen from relations (3.4) and Figure 5.4, the adjacent minima correspond to the opposite sense of circular

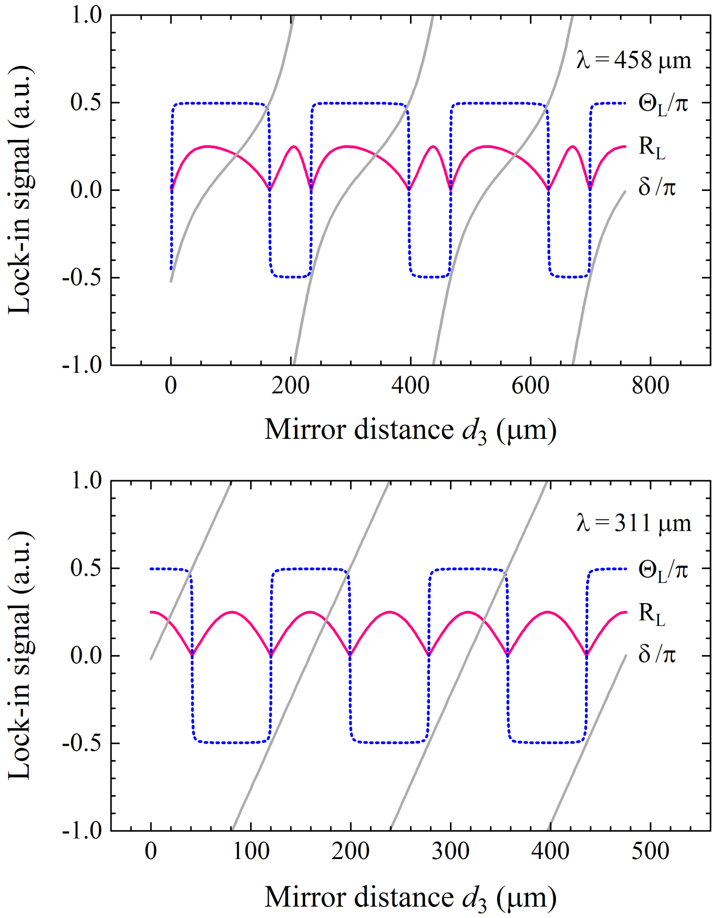

Figure 5.5: Theoretical lock-in signal together with the phase retardance as a function of mirror distance d_3 for two FIR/THz wavelengths 458 µm and 311 µm. The calculations take into account the layered structure shown in Figure 5.2 and reasonable parameter values ($\tan\alpha_0 = 0.99$, $\theta_0 = 10°$, $n_0 = n_3 = 1$, $d_1 = 200\,\mathrm{nm}$, $n_{1x} = 370 + 400\,i$, $n_{1y} = 3 + 0.00001\,i$, $d_2 = 100\,\mu\mathrm{m}$, $n_2 = 1.54$, $n_4 = 447 + 534\,i$). The optical properties of the materials are taken from the literature [62, 63], while the refractive indices of the wire grid are estimated from the effective medium theory [65].

polarization and the adjacent maxima to the linear polarizations perpendicular to each other, while elsewhere the polarization is elliptical.

Further, from the measured magnitude curves we can estimate how accurately the circular polarization is adjusted. Assuming $E_{0y} \leq E_{0x}$, we calculate the relative amplitude (3.5) of the electric vector components as

$$\tan\alpha = \sqrt{\frac{R_{\mathrm{L,max}} - R_{\mathrm{L,min}}}{R_{\mathrm{L,max}} + R_{\mathrm{L,min}}}}\,. \tag{5.21}$$

If a polarization ellipse is close to a circle, then the relative amplitude is approximately equal to the ellipticity (3.6) of the polarized light. For perfect circular polarization, the minimum of signal magnitude reaches zero and the ellipticity reaches unity.

The above signal analysis applies generally to the δ dependence, regardless of how the phase shift between the components (3.1) of the electric vector has been achieved. Assume now that the phase difference is controlled by the variable phase retarder via the mirror-grid separation. Ideally, as stated in Section 5.2, the retardance is a linear function of the mirror distance according to the relation 5.1. This means that we obtain the same pattern as in Figure 5.4 with equidistantly spaced extrema when scanning the mirror position. The situation is more complex for the wire-grid deposited on a transparent substrate (see Figure 5.2). Using the expressions (5.2, 5.3) and (3.8) we can evaluate the lock-in signal components (5.14, 5.15) and plot them, for reasonable values of parameters, as a function of d_3. Compared to the ideal case, the equidistant nature of the extrema is lost due to non-linear dependence of the phase retardance δ on the mirror distance d_3, as clearly seen in the upper panel of Figure 5.5. The exceptional quasi-equidistant behavior at the laser line 311 µm can be ascribed to a coincidence of $\lambda/2$ and the optical thickness of the substrate, so that $\delta_2 \approx \pi$. It should be noted that the metallic surfaces in the real system do not exhibit perfect reflectivity, which leads to partial absorption of the incident waves and to slight variations of the real amplitude (5.3) with the mirror position. Consequently, some relationships apply only approximately, such as $\alpha \approx \alpha_0$. The expression for the relative amplitude (5.21) is only approximate, since the signal minimum (5.20) and maximum (5.19) are measured at different mirror positions. In the presented calculations, however, the variations of the relative amplitude due to the absorption effects are below 0.2% and may be neglected.

5.5 Phase retarder construction

The experimental setup shown in Figure 4.2 incorporates three identical wire-grid linear polarizers commercially available from the Tydex Co [66]. The first polarizer P1, embedded in a manual rotation mount, ensures proper orientation of the electric vector of the radiation incoming to the retarder. The other two polarizers are mounted in the retarder and analyzer devices as indicated in Figure 4.2. The transmitting axes of the polarizers P1 and P2 make an angle of 45 degrees. The polarizers consist of a transmission aluminum grating with 1200 grooves per millimeter that is deposited on a high-density polyethylene (HDPE) substrate of 100 µm thickness. According to the manufacturer's specifications, the degree of polarization of transmitted power is greater than 99.5%, whereas the transmission of unwanted radiation is less than 0.1% across a wide range of wavelengths from 30 µm up to millimeter waves. The polarizers, as well as all other optics, are functional throughout the entire line spectrum produced by our laser source.

The retarder assembly is mounted on a base which provides out-of-plane tilting and in-plane rotation (see the photo in Figure 5.6). A golden mirror is firmly attached to a moving platform by a right-angle bracket while the polarizer P2 may be precisely positioned by a kinematic rotation mount to a parallel arrangement with the mirror. The parallelism of the mirror and the wire grid is adjusted using a visible laser diode. The optical elements are positioned so that the laser spot is

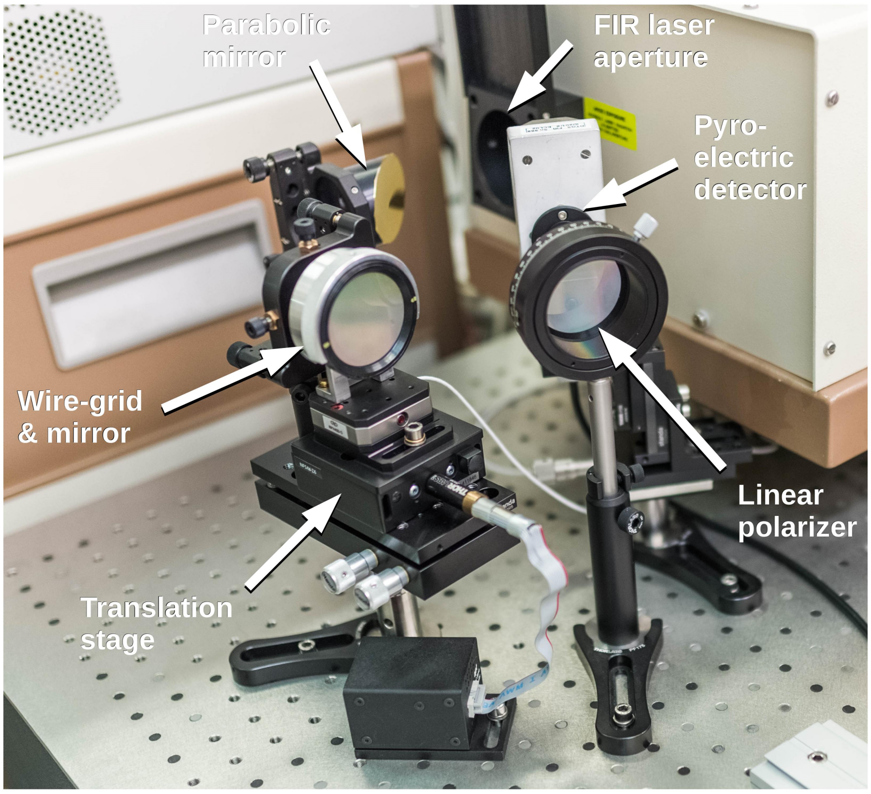

Figure 5.6: Tunable phase retarder on the optical table.

retro-reflected to the source within the precision of ±1.5 mm at the distance of 3.5 m. This procedure guarantees that a deflection from the parallel orientation is not greater than 1 mrad. Linear movement of the mirror is provided by a motorized translation stage with a backlash less than 5 µm, which is compensated by the motor controller software. An optical rotary encoder ensures minimum displacement resolution of 40 nm. Since any target position of the stage is always approached from the same direction, the most limiting factor of the motion system is the unidirectional repeatability, that has been estimated below 1 µm.

The wire-grid analyzer is secured to a home-made rotational mount which enables spinning with frequency of 6 Hz. The reference signal for the lock-in amplifier is supplied by a photodiode coupled with a LED source which is mechanically chopped by a rotating slotted disk. Although the reference pulse is generated once per cycle, we can still take advantage of the $2f$ detection mode provided by the lock-in amplifier and measure the signals at twice the input reference frequency.

5.6 Method of operation

With the rotating analyzer inserted into the optical path, we scan the mirror distance while measuring the lock-in signals R_L and Θ_L. As already stated in the previous sections, circular polarization occurs for the mirror position at the minimum of the magnitude signal. The relative amplitude (5.21) of the light incident on the retarder device is set to unity by the polarizer. However, on reflection the amplitude may be modified, since the components E_{0y} and E_{0x} are attenuated differently. In that case, the minimum of the magnitude signal does not reach zero. Nevertheless, we can set the mirror position at the signal minimum and turn the polarizer P1 slightly to get the signal as low as possible. Then we repeat the scan again and, using equation (5.21), we check the relative amplitude, which should ideally be equal to unity. An example of the experimental mirror scan for the laser wavelength 458 µm and 311 µm is plotted in Figure 5.7. The obtained high values of relative amplitude, about $0.97 - 0.99$, indicate that this method allows us to adjust polarization very close to the circular state.

Once the data are recorded, the analyzer mount may be removed from the optical path. Then we switch the lock-in reference frequency to normal operation mode and the reference input to the signal generator. Now we choose an appropriate mirror position depending on what state of polarization we require or we can switch between selected positions during the measurement.

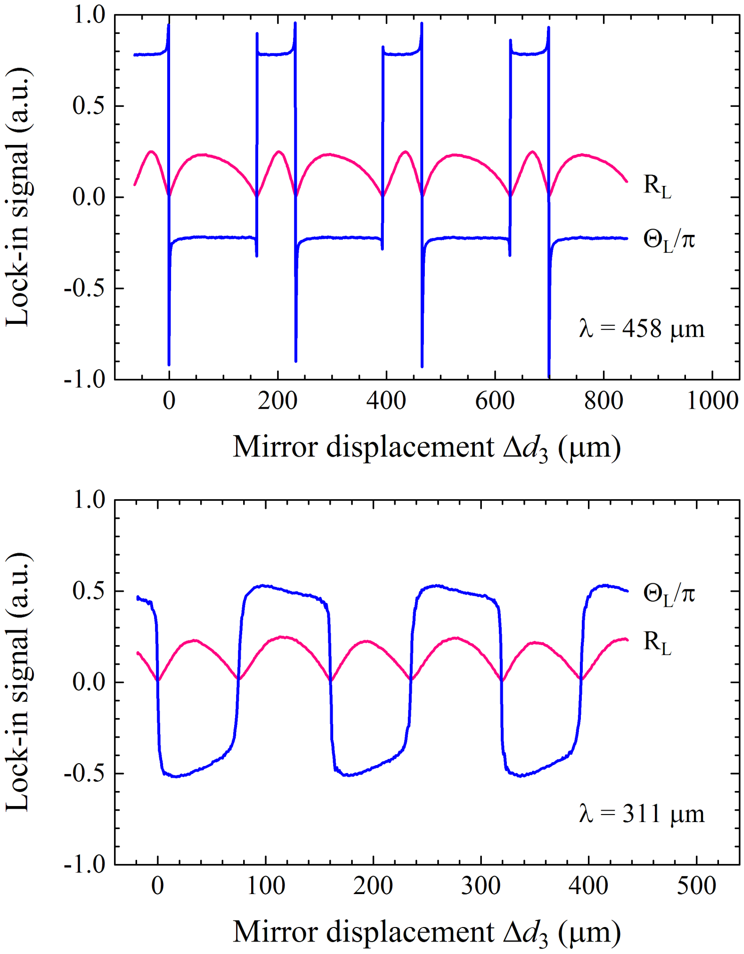

Figure 5.7: Measured lock-in signal as a function of mirror displacement Δd_3 at two FIR laser lines 458 µm and 311 µm. For each mirror scan, one position of minimum amplitude signal is selected as the origin of the coordinate axis ($\Delta d_3 = 0$). The approximate mirror-grid separation is $d_3 \approx 3 - 4\,\mathrm{mm}$.

5.7 Cyclotron resonance measurement

In order to test the performance of the tunable THz polarizer in practice, one needs a physical system for which the right and left-handed circularly polarized beams are eigenmodes, i.e. they are independent, and at the same time they exhibit significantly different optical properties in the THz range. A perfect candidate is a layer or multilayer of homogeneous isotropic materials which in a magnetic field reveals a single cyclotron resonance. In a magnetic field parallel with the k-vector, $B > 0$, the right-hand circular polarization (RHCP) is the cyclotron active component of the radiation, while the left-hand circular polarization (LHCP) causes a continuous background only. For $B < 0$, all signs are inverted and LHCP becomes cyclotron-active [67].

Here, we report cyclotron resonance measurements of a high-quality two-dimensional electron gas sample grown by molecular beam epitaxy of AlGaAs and GaAs multilayer structure on 0.5 mm thick undoped GaAs substrate. The substrate is a semi-insulating material with high resistivity ($10 \times 10^7\,\Omega\,\mathrm{cm}$) and low mobility of charge carriers ($5 \times 10^3\,\mathrm{cm}^2\,\mathrm{V}^{-1}\,\mathrm{s}^{-1}$). The gas of free electrons is accommodated in a GaAs quantum potential well of 30 nm thickness with 25 nm AlGaAs barriers on both sides. The electrons are delivered into the potential well from the surrounding layers of Si-doped $\mathrm{Al}_{0.3}\mathrm{Ga}_{0.7}\mathrm{As}$. Undoped AlGaAs continues 500 nm towards the substrate and 125 nm towards the surface. The surface of the structure is capped with 10 nm of GaAs. Important parameters of the electron gas, the two-dimensional electron mobility $\mu_{\mathrm{2D}} = 6 \times 10^5\,\mathrm{cm}^2\,\mathrm{V}^{-1}\,\mathrm{s}^{-1}$ and the sheet carrier concentration $n_{\mathrm{2D}} = 3 \times 10^{11}\,\mathrm{cm}^{-2}$, are estimated from the Hall resistivity measurements performed in a dark environment.

The transmission was measured for three different FIR/THz wavelengths using linearly and circularly polarized laser beams. The sample was placed in the optical cryostat and exposed to an ambient light background. The sample temperature was kept at 100 K while the magnetic field was swept in both positive and negative direction. In Figure 5.8 we only show the results for the $458\,\mu\mathrm{m}$ laser line obtained in the left and right-hand circularly polarized light. In both cases, transmission exhibits a sharp dip corresponding to the cyclotron resonance when the polarization component is cyclotron-active, and no visible dip when inactive. This demonstrates that the prepared polarization states are not a mixture of LHCP and RHCP states. Furthermore, transmissions for left and right-handed circularly polarized beams are nearly perfectly antisymmetric (see the lower inset in Figure 5.8). The effective electron mass estimated from the position of the transmission minimum, $m^* = 0.069\,m_{\mathrm{e}}$, is in a good agreement with the tabulated value $m^* = 0.067\,m_{\mathrm{e}}$ [68]. A detailed analysis of the transmission dependence on the magnetic field is not the primary objective of this study, and will be reported elsewhere. Additional transmission measurements using a linear polarization (not shown here) are consistent with the presented LHCP and RHCP data, and confirm the good performance of our tunable THz circular polarizer.

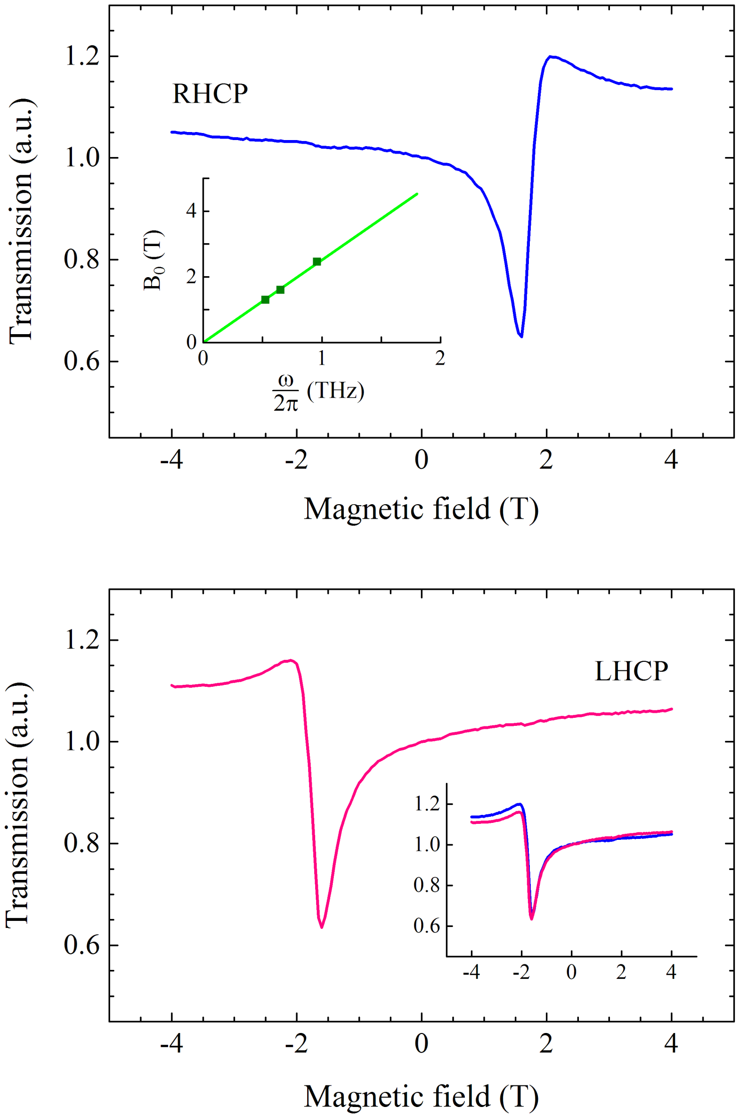

Figure 5.8: Transmission of a 2D electron gas in a GaAs/AlGaAs heterostructure measured at 100 K using a sharp FIR laser line 458 µm. Cyclotron resonance absorption occurs at magnetic field $B_0 = \pm 1.6$ T according to the sense of circular polarization. From the frequency dependence of the resonant field B_0 (see the upper inset) the electron effective mass is estimated as $m^* = 0.069\, m_\mathrm{e}$. In the lower inset, the magnetic field dependence of LHCP transmission is compared with the inverted RHCP curve ($B \to -B$).

6 Transmission experiments

The optical properties of superconductors are usually examined by measuring the spectra at several fixed temperatures or magnetic fields. Subsequent analysis of the spectral data provides the complex optical conductivity of the sample. However, the results reported in this chapter were gathered by a different method. A sharp FIR/THz laser line was tuned and the sample transmission was measured as a function of sweeping the temperature at a constant magnetic field. Similar experiments were done with a fixed temperature while sweeping the magnetic field. In contrast to standard spectroscopy methods, this approach provides a very detailed temperature and field dependence of the transmission, which can hardly be obtained by other techniques. Nevertheless, the complex optical conductivity cannot be retrieved solely from the transmission itself, and therefore a theoretical modeling of sample properties is required to interpret the experimental data. This minor deficiency of the presented method could be overcome by a planned extension of our experimental equipment with the Mach-Zender interferometer [47], which in addition to the transmitting intensity provides a phase shift of the transmitted wave. Although extraction of the complex conductivity from transmission and reflection measurements is also possible, this approach is easily applicable when the two quantities are comparable ($\mathcal{R} \approx \mathcal{T}$). However, this is not the case for superconducting films, due to their high reflectance ($\mathcal{R} \approx 1$) and low transmittance ($\mathcal{T} \ll 1$). For highly reflective films, a more accurate determination of complex conductivity is achieved from simultaneously measured transmission and phase shift data.

Transmission measurements of superconducting films are referred for various configurations of polarization and magnetic field. Some selected representative data related to linearly polarized radiation are presented in Section 6.2, but a more detailed analysis of the results can be found in the attached publications starting on page 77. Section 6.3 describes new, as yet unpublished measurements obtained with the developed circular polarizer.

6.1 Superconducting samples

It is well known that the properties of superconducting thin films can be influenced by many factors such as film thickness, material and substrate quality, method and conditions of preparation, etc. To eliminate these side effects and to capture the essential features of the studied superconducting films, samples of different type and different provenance were collected. Basic properties and characteristics of the samples were provided by their manufacturers. However, some additional parameters important for theoretical modeling of transmission were determined from supporting experiments performed in the laboratories

Film	T_c K	d_1 nm	Substrate	d_2 mm	Provenance	Ref.
NbN	10.8	80	Si †	0.25	Š. Beňačka	[69]
NbN	16	15	Al_2O_3 ‡	0.33	K. Ill'in	[30, 70–72]
$YBa_2Cu_3O_{7-\delta}$	87.6	107	$LaAlO_3$ *	0.50	Y. T. Wang	[73]

† High-resistivity silicone. ‡ R-cut sapphire. * Sample abbreviated as YBCO/LAO.

Table 6.1: Superconducting samples.

of the Institute of Physics CAS and the Faculty of Mathematics and Physics. Physical Property Measurement System (PPMS) from Quantum Design Inc was employed to estimate the normal state dc conductance σ_0, and terahertz time-domain spectroscopy (THz-TDS) was utilized to determine the refractive index of the substrate. Transmission measurements were conducted in the laboratory of far-infrared magnetospectroscopy (FIRM) in the Institute of Physics CAS.

Table 6.1 lists the tested samples and their characteristic parameters such as the film thickness d_1, the critical temperature T_c, and the substrate material and thickness d_2. All substrates are of square shape with dimensions of 10 mm × 10 mm. The samples under study are epitaxial crystalline films except for NbN/Si which is polycrystalline. Epitaxial films reveal higher T_c and sharper superconducting transition compared to polycrystalline films of the same material and thickness. However, the critical temperature of very thin films depends considerably on the thickness. The quality of the superconducting layer is greatly influenced not only by conditions of the fabrication process but also by the substrate material on which the film is deposited. For the epitaxial growth, a close matching of the crystalline lattice between the film and the substrate is necessary. Another requirement stemming from transmission experiments is that the substrate is transparent in the FIR spectral region. For the above reasons, the choice of suitable substrates is relatively limited.

Niobium nitride (NbN) is a classical conventional low-temperature superconductor, whose behavior may be clearly explained by the BCS theory. However, there is a large variation of film parameters in the literature [78–81] as shown in Table 6.1. In general, it can be stated that the NbN superconductor is in the dirty limit ($l \ll \xi_0$), due to its relatively short mean-free path of electrons, and in the

critical temperature	T_c	10 – 16	K
optical gap	$2\Delta_0$	3.9 – 4.6	$k_B T_c$
electron scattering time	τ	2 – 5	fs
electron mean-free path	l	0.6 – 0.8	nm
normal dc resitivity	ρ_n	1 – 3	µΩ m
BCS coherence length	ξ_0	4 – 5	nm
magnetic penetration depth	λ_L	~ 176	nm
upper critical field	B_{c2}	~ 26	T

Table 6.2: Typical parameters of NbN thin films [74–81].

local limit ($\xi_0 \ll \lambda_\mathrm{L}$) for a large magnetic penetration depth. A rather high ratio $2\Delta_0/k_\mathrm{B}T_\mathrm{c}$, which exceeds the BCS theory established value $2\Delta_0/k_\mathrm{B}T_\mathrm{c} = 3.53$, indicates a strong coupling mechanism of superconductivity [82].

The NbN film deposited on a high-resistivity silicone substrate was prepared by magnetron sputtering in the Institute of Electrical Engineering, Slovak Academy of Sciences, Bratislava. This sample is a polycrystalline superconductor with randomly oriented crystallites of about 4 to 8 nm in size. The critical temperature of individual grains may vary slightly, which is reflected in a broader superconducting transition. The normal state dc conductivity right above T_c was determined as $\sigma_0 = 0.45 \times 10^6\,\Omega^{-1}\mathrm{m}^{-1}$.

The second NbN film deposited on a R-cut sapphire was fabricated by magnetron sputtering method in the Institute for Micro and Nano Electronics Systems, University of Karlsruhe, Germany. The film is most likely purely epitaxial, because no crystallites were observed by a high resolution transmission electron microscopy. A better sample parameters were confirmed in the dc resistance measurements showing a higher critical temperature and a narrow superconducting transition (Figure 6.2). From the obtained PPMS data, the normal state dc conductivity was estimated as $\sigma_0 = 0.51 \times 10^6\,\Omega^{-1}\mathrm{m}^{-1}$. The R-cut sapphire appears to be a more suitable material for deposition of the NbN superconducting films. On the other hand, sapphire reveals considerable birefringence (see Figure 6.1), which rather complicates the interpretation of experimental data [71]. Our R-cut sapphire substrate is a square-shaped slab with the extraordinary-ray axis in the square diagonal. In this convenient arrangement, when the diagonal and the electric vectors of normally incident waves form an angle of 45°, the horizontally and vertically polarized beams propagate in the same manner despite the anisotropy of the substrate.

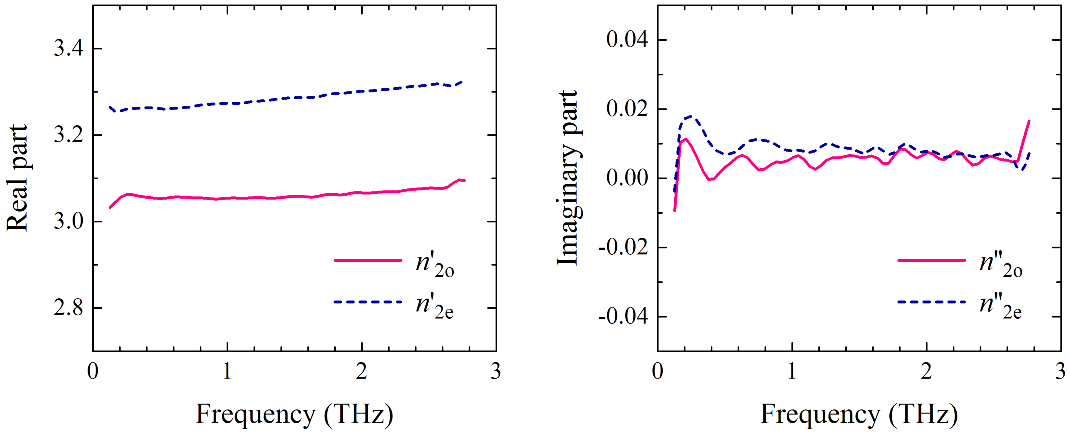

Figure 6.1: Complex refractive indices of the sapphire substrate as obtained by the time-domain terahertz spectroscopy for the ordinary ray $n_{2\mathrm{o}} = n'_{2\mathrm{o}} + i\,n''_{2\mathrm{o}}$ and the extraordinary ray $n_{2\mathrm{e}} = n'_{2\mathrm{e}} + i\,n''_{2\mathrm{e}}$.

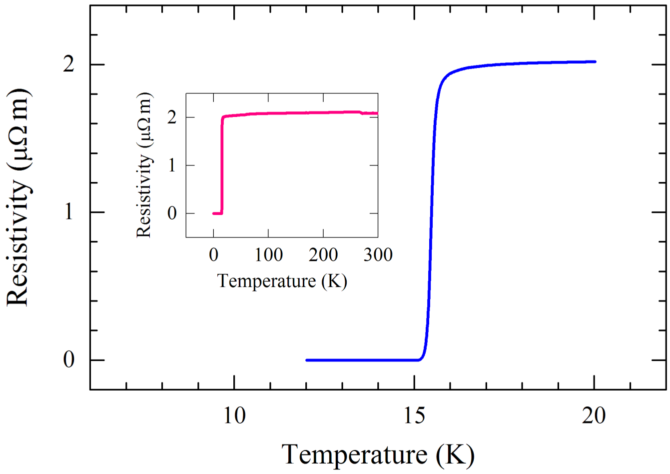

Figure 6.2: Resistivity of the NbN/sapphire sample in a zero magnetic field measured by PPMS. Onset of the superconducting transition is clearly visible at approximately 16 K.

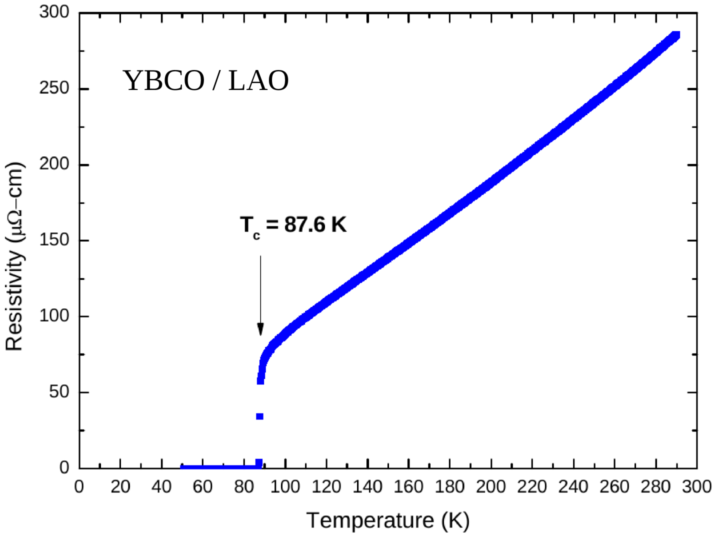

Figure 6.3: Resistivity of the YBCO/LAO sample as measured at NCTU, Taiwan.

Yttrium barium copper oxide (YBCO) is a non-conventional superconductor belonging to a family of high-temperature superconducting (HTS) materials with a perovskite crystal structure. A suitable substrate for epitaxial growth of such superconductors is the lanthanum aluminate (LAO) oriented in (100) plane. The YBCO/LAO sample was deposited from a stochiometric target using a pulsed laser deposition method in National Chiao Tung University (NCTU), Hsinchu, Taiwan. This relatively high quality film, having a thickness of 107 nm, shows the onset of the superconducting transition at a critical temperature $T_c = 87.6\ K$, as evidenced by the resistivity dc measurement in Figure 6.3. Its disadvantage, however, is the LAO material of the substrate, which reveals a weak birefringence. The magnitude of the birefringence can be expressed as the difference between ordinary and extraordinary refractive indices $\Delta n = n_\mathrm{e} - n_\mathrm{o}$. We estimate the maximum value of birefringence to $|\Delta n| \approx 0.08$ from data obtained by the THz time-domain spectroscopy at ambient temperature. The extraordinary-ray axis of the substrate lies in its diagonal as in the above case of the birefringent sapphire substrate.

6.2 Experiments with linear polarization

Experimental results presented in this section were obtained with a slightly different setup than specified in Chapter 4. The older arrangement of the optical path did not include a tunable phase retarder, but a linear wire-grid polarizer was optionally inserted before the sample to ensure horizontal or vertical polarization of the FIR/THz laser lines. For detailed information on the measurement conditions see Ref. [30]. Linearly polarized radiation transmitted through superconducting films was measured as a function of temperature in zero magnetic field and in several magnetic fields in Faraday and Voigt geometry. This type of experiment, known as the *far-infrared laser thermal spectroscopy* [83], is based on the temperature dependence of the optical energy gap of superconductors. A photon energy $\hbar\omega$ is selected appropriately below $2\Delta_0$ and the sample temperature T is swept slowly across the superconducting transition. In this way, the optical gap $2\Delta(T)$ is continuously varied, until it passes through a point of an increased absorption at a temperature T_ω where $2\Delta(T_\omega) = \hbar\omega$. The thermal spectroscopy method is found to be especially useful for studying conventional superconductors whose temperature characteristics are well described by the BCS theory.

To better understand experimental data, let's first analyze a simple example of a free-standing layer of a conventional superconductor in zero magnetic field. Figure 6.4 illustrates the optical properties of such an uncomplicated system using the theoretical expressions for the BCS optical conductivity [21] and general recurrence formulas introduced in Section 3.2 applied for a single layer. Absorbance, reflectance and transmittance are plotted as a function of reduced temperature T/T_c for several terahertz photon frequencies. To provide a qualitative explanation of their behavior we must consider the microscopic nature of superconductivity. At zero temperature, all conduction electrons are bound to form Cooper pairs. At a non-zero temperature, a Cooper pair may be broken when absorbing a thermal phonon, which leads to creation of two thermally excited quasiparticles. With raising temperature, an increased amount of generated quasiparticles results in reduction of superconducting gap. Annihilation of two quasiparticles is also possible by constituting a Cooper pair while emitting the binding energy in a form of a phonon. Another process taking place in the system is scattering of thermally excited quasiparticles. At a finite temperature interval, where $2\Delta(T) > \hbar\omega$, only a balance of thermal excitation and recombination of quasiparticles determines the fraction of superconducting and normal phases, and affects therefore the absorption of FIR radiation. However, for temperatures where $2\Delta(T) \leq \hbar\omega$ the absorption is noticeably increased by creation of two photon-excited quasiparticles. The raised absorption is accompanied by an increase in transmission, which is generally compensated by a drop in reflection.

This behavior indicates that the absorption peak is associated with a partial suppression of superconductivity and can be understood at the microscopic level as a breakdown of the Cooper pairs by absorbing the FIR photons. For the photon frequencies above the zero-temperature optical gap $2\Delta_0 \leq \hbar\omega$, the breaking of Cooper pairs occurs in a full range of temperatures below T_c.

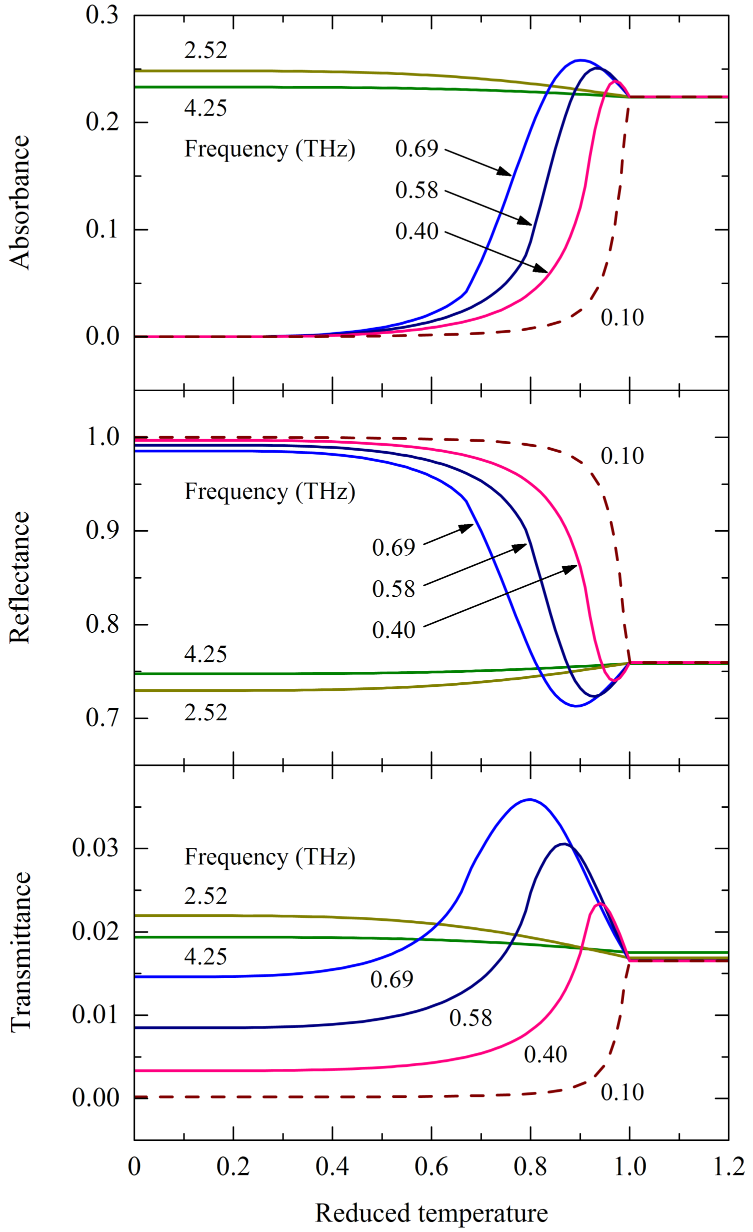

Figure 6.4: Optical properties of a free standing BCS superconductor film of thickness 80 nm, critical temperature $T_\mathrm{c} = 10.8\,\mathrm{K}$, normal state conductivity $\sigma_0 = 0.45 \times 10^6\,\Omega^{-1}\mathrm{m}^{-1}$ electron scattering time $\tau = 10\,\mathrm{fs}$, and BCS optical gap $2\Delta_0 = 3.53\,k_\mathrm{B}T_\mathrm{c}$. Numerical calculation utilizes the expression for the optical complex conductivity of a BCS superconductor according to *Zimmermann et al.* [21]. Calculations were performed for several representative FIR/THz laser frequencies (solid lines) and one microwave frequency (dashed line).

6.2.1 Transmission in zero magnetic field

Temperature dependent transmission of NbN/Si sample was measured in zero magnetic field at linearly polarized FIR laser lines. In this case, exact orientation of the electric vector of the incident wave is not significant since the silicon substrate is an optically isotropic material. In addition, the laser beam is almost perpendicular to the sample surface, which means that the polarizations s and p related to the plane of incidence are not distinguished. This experiment, therefore, represents the simplest configuration favorable for easy interpretation of the obtained data which are presented in Figure 6.5. BCS model calculations, however, did not lead to good quantitative agreement with the measured transmission and did not reproduce correctly the thermal peak observed at the laser line 742.6 µm. Even a large variation of sample parameters used in the theoretical modeling could not explain the experimental data. This discrepancy may be related with the polycrystalline nature of the film. A better agreement is achieved when a broadening of the superconducting transition is considered in the calculation of the complex conductivity. A uniform distribution of the critical temperatures T_c in the individual superconducting grains is assumed in the interval from 9.8 to 10.8 K, but in reality it can be even broader. The most probable value of the optical gap was estimated from literature [78, 79] as $2\Delta_0 = 4.16\,k_\mathrm{B}T_\mathrm{c}$, which, expressed in frequency units, gives a variance of the optical gap for the individual grains from 0.85 to 0.94 THz. Some parameters important for transmission calculation are listed in Table 6.1 others have already been reported in sample description. The normal state dc conductivity $\sigma_0 = 0.45 \times 10^6\,\Omega^{-1}\mathrm{m}^{-1}$ was obtained from the dc resistivity measurements, whereas the scattering time was estimated as $\tau = 5\,\mathrm{fs}$. In fact, a precise value of τ is not so important, since, close to the dirty limit ($\tau = 0$), the calculated conductivity is not significantly affected by this parameter [21]. Refractive index of the silicon substrate was taken from the literature [84].

The NbN epitaxial film on a sapphire substrate was probed at several FIR frequencies near the optical gap with horizontal and vertical polarization of the incident laser beam. Figure 6.6 displays only the data obtained for the horizontally polarized radiation. Since NbN is an isotropic superconductor, the only anisotropy is introduced by the birefringent sapphire substrate. In the special case, when the extraordinary ray axis of the sapphire substrate and the electric vector of the incident beam form an angle of 45°, the horizontally and vertically polarized radiation should give the same result. The difference in transmission observed between the two polarizations was less than 5%, which can be attributed to a slight misalignment of the sample. Even for the 742.6 µm laser line, for which the transmission in the zero-temperature limit is very weak, the relative difference is still within 10%. The sample temperature was swept up and down at a low rate of about 1 K/min, without observable temperature hysteresis. Temperature-independent transmission of the sample in the normal state provides a suitable reference point for the normalization of measured curves. In the superconducting state, the transmission of photons with energies far below the optical gap shows a monotonic behavior. However, when the photon energy is approaching the optical gap, a typical BCS thermal peak appears just below T_c. Closer to the gap, the

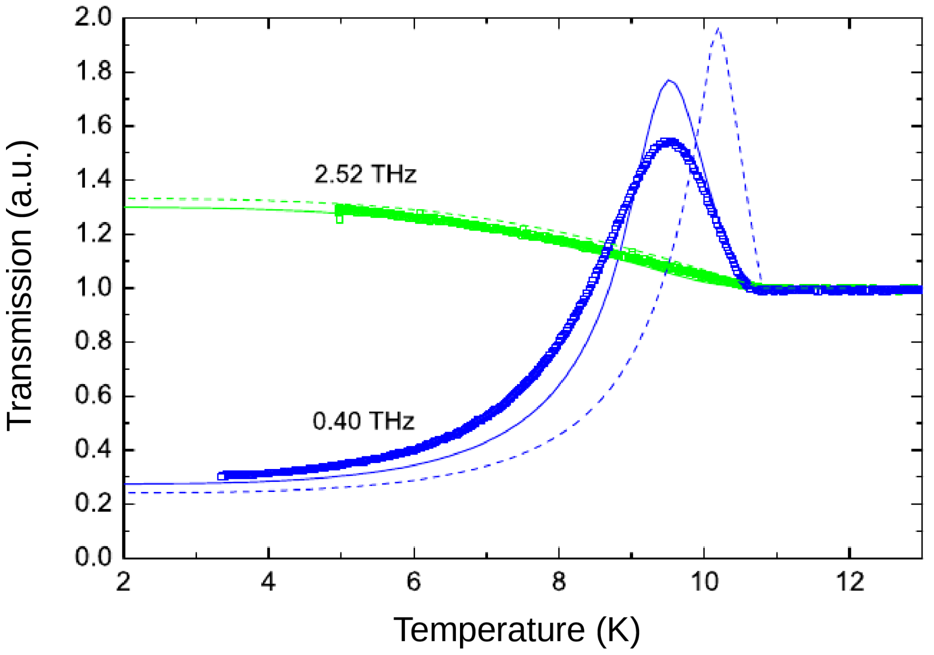

Figure 6.5: Transmission of linearly polarized FIR radiation through a NbN/Si sample measured in zero magnetic field as a function of temperature (points). Theoretical curves are calculated using the BCS optical conductivity with a sharp superconducting transition (dashed lines) and with a broadening of transition (solid lines).

peak becomes wider, while its position moves to lower temperatures. Finally, the peak completely disappears when the photon energy exceeds the optical gap, and, in the infinite-frequency limit, the transmission coincides with its normal-state value over the entire temperature range.

To calculate the theoretical curves shown in Figure 6.6, the theoretical approach of *Zimmermann et al.* [21] was utilized, but their simple analytical function for the gap approximation was replaced by more exact values obtained from numerically solved BCS gap equation. The model parameters T_c and σ_0 are sufficiently well established and their variations within experimental errors do not appreciably influence the calculated transmission. The values of the optical gap $2\Delta_0 = 4.15\,k_B T_c$ and the relaxation rate $\tau = 4\,\text{fs}$ were taken from the literature [78]. In our frequency range, where $\omega\tau < 0.1$, the dirty limit $\tau \to 0$ seems appropriate. As the optical system is anisotropic, calculation of the transmission must take into account birefringent nature of the sapphire substrate [70]. The parameters for sapphire, the ordinary and extraordinary refractive indices and the substrate thickness, were determined from experimental data obtained by the time-domain terahertz spectroscopy (see Figure 6.1). While variations of the film parameters within their experimental errors hardly affect the calculated transmission, the results are much more sensitive to the ordinary and extraordinary indices of the substrate. This is understandable, since the optical thickness of the substrate is responsible for interference effects that can significantly alter the observed sample transmission. To achieve the best agreement between

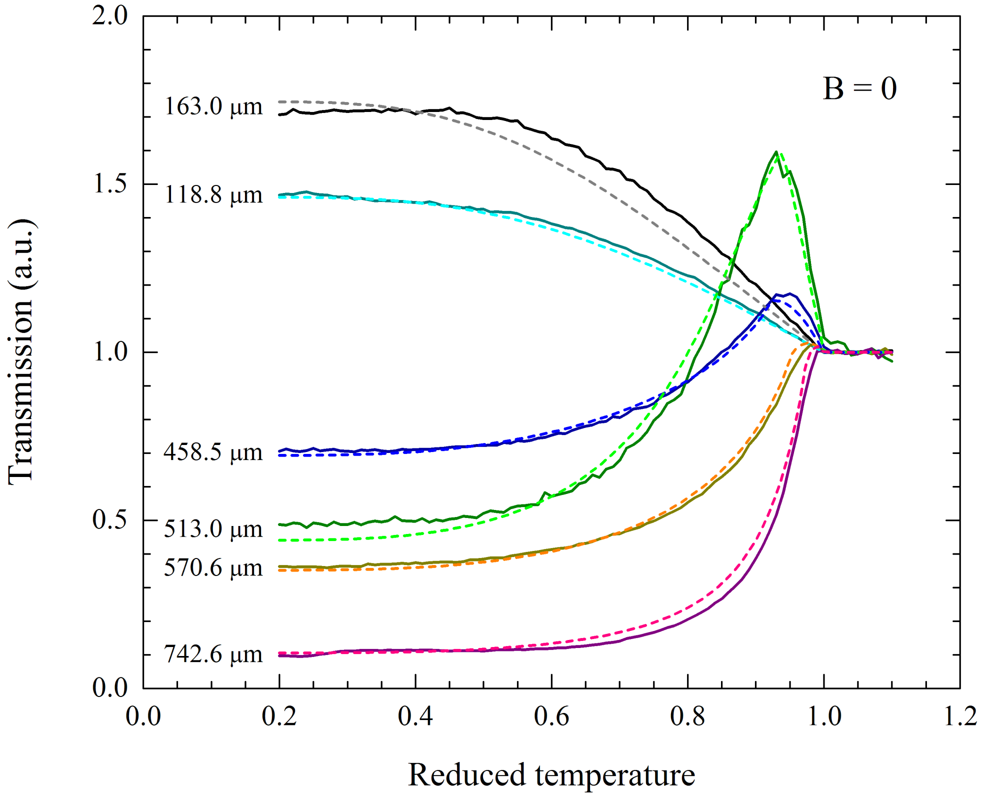

Figure 6.6: Zero-field transmission of the NbN/sapphire sample as a function of temperature. Solid lines represent experimental data obtained at several FIR wavelengths and with a linear polarizer oriented horizontally. Theoretical model based on the BCS optical conductivity [21] is represented by the dashed lines. All curves are plotted relatively to the normal state transmission $\mathcal{T}_{\mathrm{N}}$ and in reduced temperature units T/T_{c}.

calculated and measured data, the substrate parameters were slightly modified within their experimental errors. Optimal numerical simulations of transmission versus temperature are plotted in Figure 6.6 as dashed lines. It is clearly visible that the BCS thermal peak can be faithfully reproduced by the adopted theoretical model. Moreover, a quantitative agreement between the experimental data and the fundamental BCS-based microscopic theory was achieved over the entire range of temperature and frequency, exclusively on the basis of measured physical properties of the NbN film and the sapphire substrate. The importance of accurate knowledge of the substrate parameters becomes clear when we realize that transmission is notably influenced by interference effects in the substrate. The whole sample, including the substrate and the deposited superconducting film, then acts as a Fabry-Perot etalon possessing temperature-dependent surface reflectivity.

6.2.2 Transmission in non-zero magnetic field

Optical properties of type-II superconductors in external magnetic field are substantially affected by nucleation of quantum vortices above the lower critical field B_{c1}. Since the vortices in isotropic superconductors tend to align with the applied field, symmetry of the system is reduced and various geometries of the transmission experiment must be carefully considered. While the laser beam is always oriented normally to the sample plane, an external magnetic field may be applied in different directions. Three fundamental magneto-optical configurations are distinguished in Figure 6.7. In the case of *Faraday geometry*, when the field is colinear with the incident beam k-vector, transmission of an isotropic specimen is not sensitive to the direction of linear polarization. That is understandable, since the superconducting vortices are arranged perpendicularly to the sample and the electric vector of the electromagnetic wave is perpendicular to the vortex lines. However, this configuration may be generally sensitive to handedness of the circular polarization and we shall consider this case later. In the *Voigt geometry*, when the magnetic field is perpendicular to the laser beam, orientation of the linear polarization becomes significant, because the vortex lines are parallel with the film. The electric vector of the incident wave must therefore be resolved in two components with respect to the applied magnetic field, orthogonal $\mathbf{E}^{\perp}$ and parallel $\mathbf{E}^{\parallel}$.

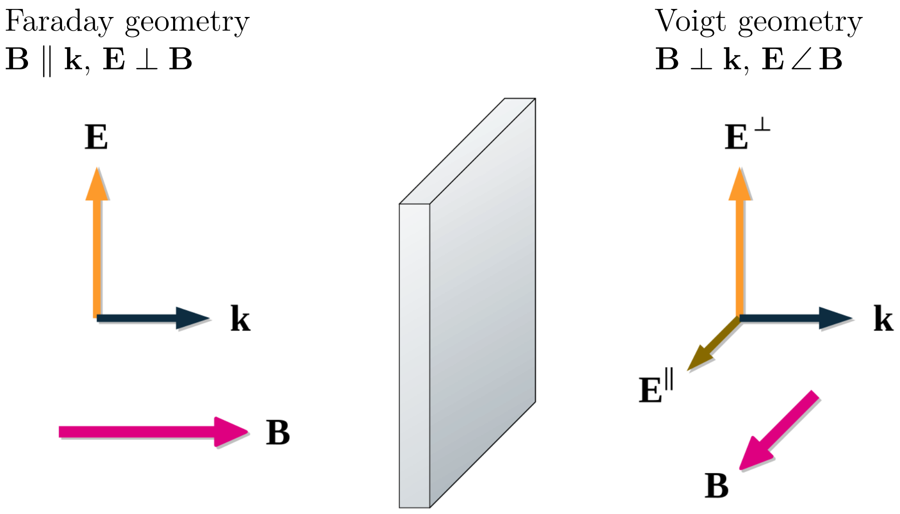

Figure 6.7: Magneto-optical configurations.

Faraday geometry

All the reported samples were examined in Faraday geometry experiments, but only linearly polarized transmission of NbN films is discussed in this section. The NbN polycrystalline film deposited on silicone substrate was measured in magnetic fields up to 9 T for a laser wavelength of 742.6 µm. Transmission data were normalized to their normal-state values and are plotted in Figure 6.8.

At low magnetic fields, the observed transmission shows similar features as in the zero field. Transmission is constant until the sample remains in its normal state, but just below T_c a BCS thermal peak rises. A declination from the flat normal-state value could be roughly understood as an onset of superconducting transition corresponding approximately to a measured dc resistivity drop. This onset point moves to lower temperatures with increasing magnetic field in accordance with the critical behavior of type-II superconductors shown in Figure 2.1. In general, the critical temperature follows a line $B_{\mathrm{c}2}(T) = B_{\mathrm{c}2}(T, J = 0)$ on the upper critical surface below which the specimen is superconducting. An influence of magnetic field on the superconducting optical gap via the critical temperature is clearly visible in Figure 6.8. With the increasing magnetic field, the observed maximum is weaker and broader and finally vanishes in a high-field limit, where the transmission reaches its normal-state value over the entire temperature range. This development of the transmission peak resembles an analogical behavior observed in zero magnetic field with photon energies approaching the high-frequency limit $\hbar\omega/2\Delta_0 \to \infty$ (compare Figure 6.5 and 6.4).

Theoretical modeling of the temperature curves measured in a finite magnetic field was described in [85]. Here we present only a brief overview of the obtained results. According to *Clem* [86], vortices in type-II superconductors are viewed as normal-state cylinders immersed in a superconducting matrix. The normal-state conductivity is assumed to be independent on an applied magnetic field and can be expressed using the Drude formula. The superconducting phase is described by the BCS optical conductivity according to *Zimmerman et al.* [21] but with a field dependent critical temperature $T_\mathrm{c}(B)$. Since the vortex cores are small compared to FIR/THz wavelengths ($\xi_0 \ll \lambda$), the optical parameters of the system can be approximated by their average effective values, such as the effective permittivity, the effective conductivity, and the effective index of refraction. Various methods of estimating the effective properties of inhomogeneous materials were already mentioned in Section 3.3. Important variables that appear in all these theories are the volume fractions of individual materials. However, amount of vortices in type-II superconductor depends on the temperature and on the applied magnetic field. To capture this feature, the volume fraction of vortex normal cores is approximated according to *Ikebe et al.* [79] as $f_n = B/B_{\mathrm{c}2}(T)$. Despite the number of approximations that have been made, the calculated transmission describes the experimental data surprisingly well (see Figure 6.9). A slightly better compliance was achieved rather by the Bruggeman theory than with the theory of Maxwell Garnet (not shown).

Far-infrared transmission of the NbN/sapphire sample was measured in Faraday configuration for fields up to 10 T. With the exception of the applied magnetic field, the experimental conditions remained the same as in the zero-field measurements, which were already discussed in the previous section. The magnetic field was applied when the sample was in its normal state at a temperature sufficiently above T_c and then the transmission was measured during a slow temperature cycle. The sample was cooled from 20 K down to 3 K and then heated again up to 20 K with a sweep rate of 1 K/min. The sample temperature was monitored by an additional calibrated field-independent temperature sensor mounted close to the measured sample. No significant difference was observed between the transmissions obtained in the cooling and heating part of the cycle. This confirms

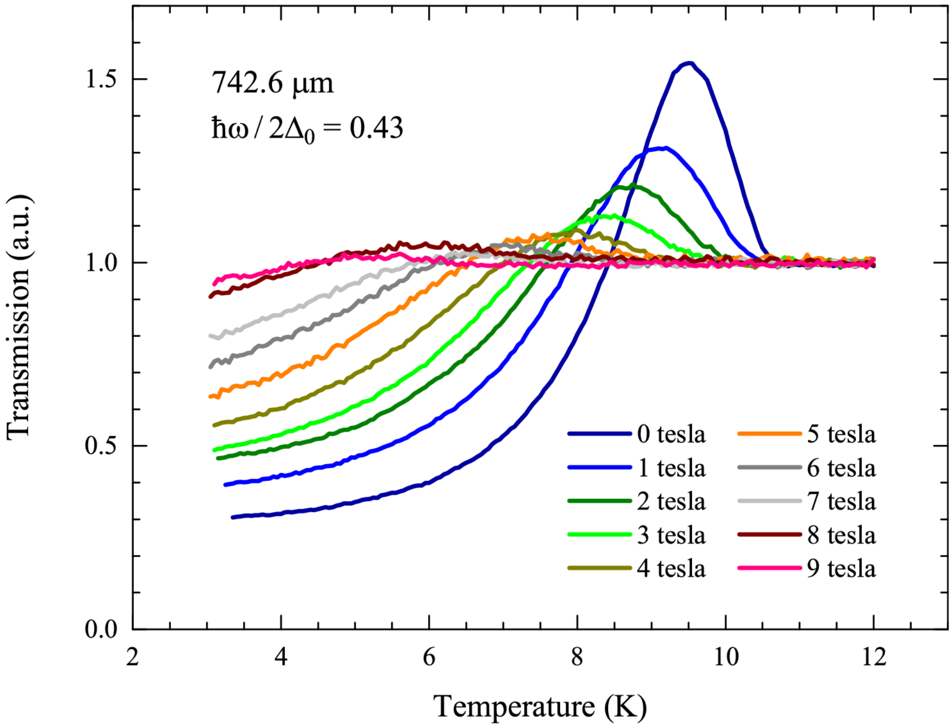

Figure 6.8: Transmission of NbN/Si sample measured in Faraday geometry.

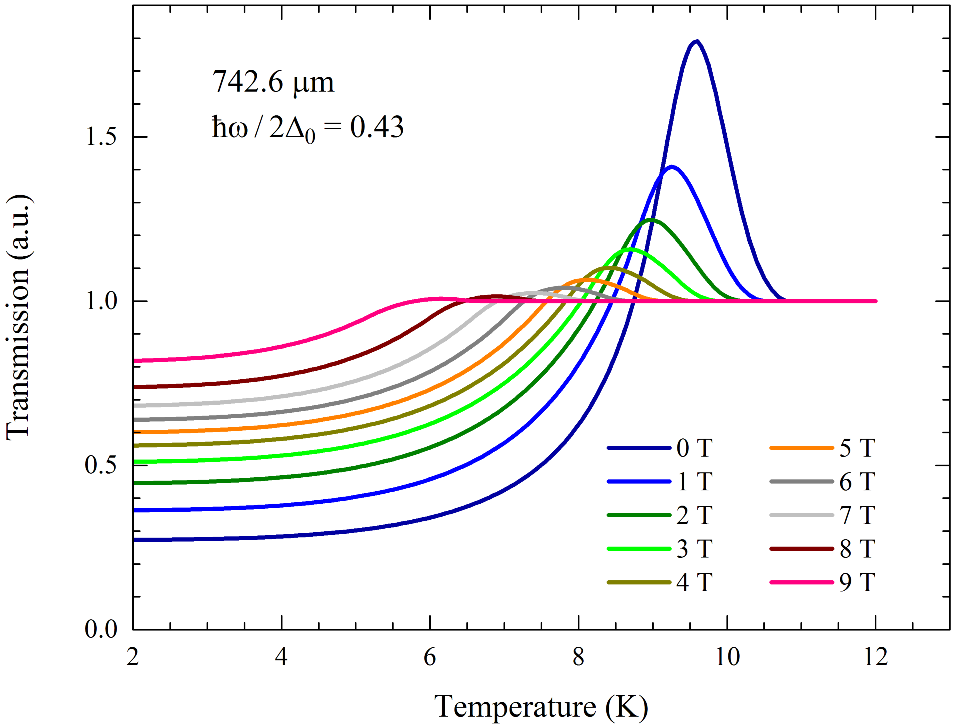

Figure 6.9: Numerical simulation of transmission of NbN/Si sample in Faraday geometry using effective medium approximation according to Bruggeman formula.

that a possible thermal gradient between the sample and the sensor was actually negligible and thus the temperature of the sample was properly determined. From available FIR laser lines, appropriate frequencies near the optical gap $2\Delta_0$ were selected to cover all the most important cases of a photon energy values expressed as a ratio $\hbar\omega/2\Delta_0$. The acquired transmission data are summarized in Figure 6.10 for several FIR laser wavelengths. An exact emission wavelength, however, could not be uniquely assigned to a line 400 µm, since its CO_2 pumping frequency is very close to other pumping lines, which can also excite the nearby FIR lines in the range of 393 − 405 µm. The wavelengths 742.6 µm and 570.6 µm represent the case of photon energies well bellow the optical gap which is reflected in monotonic behavior of transmission in superconducting state. The FIR laser lines 513.6 µm, 400 µm, and 311.6 µm are gradually approaching the optical gap revealing the BCS thermal peak in superconducting sample transmission. Finally the 118.8 µm line shows the case of the photon energy far above the optical gap with a monotonic temperature dependence. At all wavelengths, an influence of magnetic field on the critical temperature and on the superconducting gap is clearly visible. The explanation of these features is similar to the previous case of the NbN/Si sample given above in the description of Figure 6.8.

Voigt geometry

Transmission of the NbN film on a sapphire substrate was examined in a magnetic field applied in the plane of the sample and with two different orientations of the linear polarization (see Figure 6.7). Polarization of the electric vector parallel $\mathbf{E}^{\parallel}$ and perpendicular $\mathbf{E}^{\perp}$ to the applied magnetic field was ensured by an additional wire-grid linear polarizer inserted into the optical path.

In the Voigt geometry, the extraordinary axis of the birefringent substrate makes an angle of 45° with the applied magnetic field. Thus both parallel and perpendicular polarizations form the same angle of 45° with the extraordinary axis and should provide the same relative transmissions in a zero magnetic field. Above the first critical field B_{c1} vortices penetrate the superconducting film and arrange themselves in rows as was directly visualized in thin stripes at low static fields [87]. A difference in transmission due to different orientation of the electric vector with respect to the vortex rows can be expected and was indeed observed in our experiments. Figure 6.11 displays the measured transmission for the FIR wavelengths 513 µm and 458.5 µm. The overall behavior follows qualitatively the BCS scheme as was already discussed in the previous paragraphs. Transmission in the low-temperature limit increases gradually with the applied magnetic field and in a similar way as observed with the Faraday configuration. This increase, however, is more progressive in the perpendicular polarization $\mathbf{E}^{\perp}$ than in the parallel polarization $\mathbf{E}^{\parallel}$. We can therefore conclude that an anisotropy in transmission was found induced by the presence of vortices in a thin superconducting film studied in a parallel magnetic field. Theoretical modeling of the magneto-transmission of superconducting films deposited on an anisotropic substrate is rather complicated and was described in detail in [71]. Numerical simulations of FIR transmission in the Voigt geometry were published in Physica C [72] and the obtained results are illustrated in Figure 6.12.

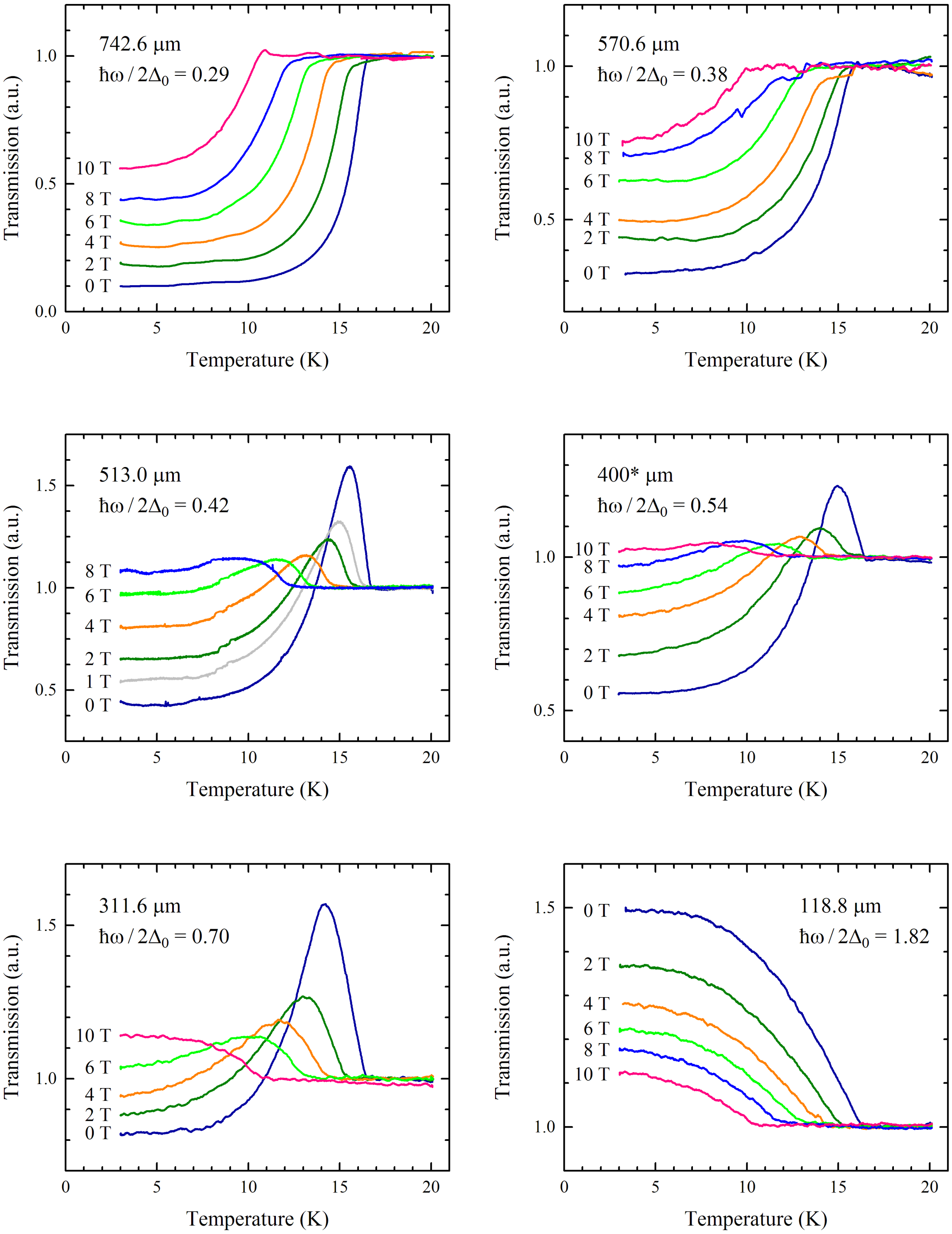

Figure 6.10: Transmission of NbN/sapphire sample measured in Faraday configuration. Formation of the BCS thermal peak is visible for FIR frequencies comparable with the optical gap $2\Delta_0$. Symbol * denotes a single FIR laser line in a cluster of wavelengths from 393 to 405 µm.

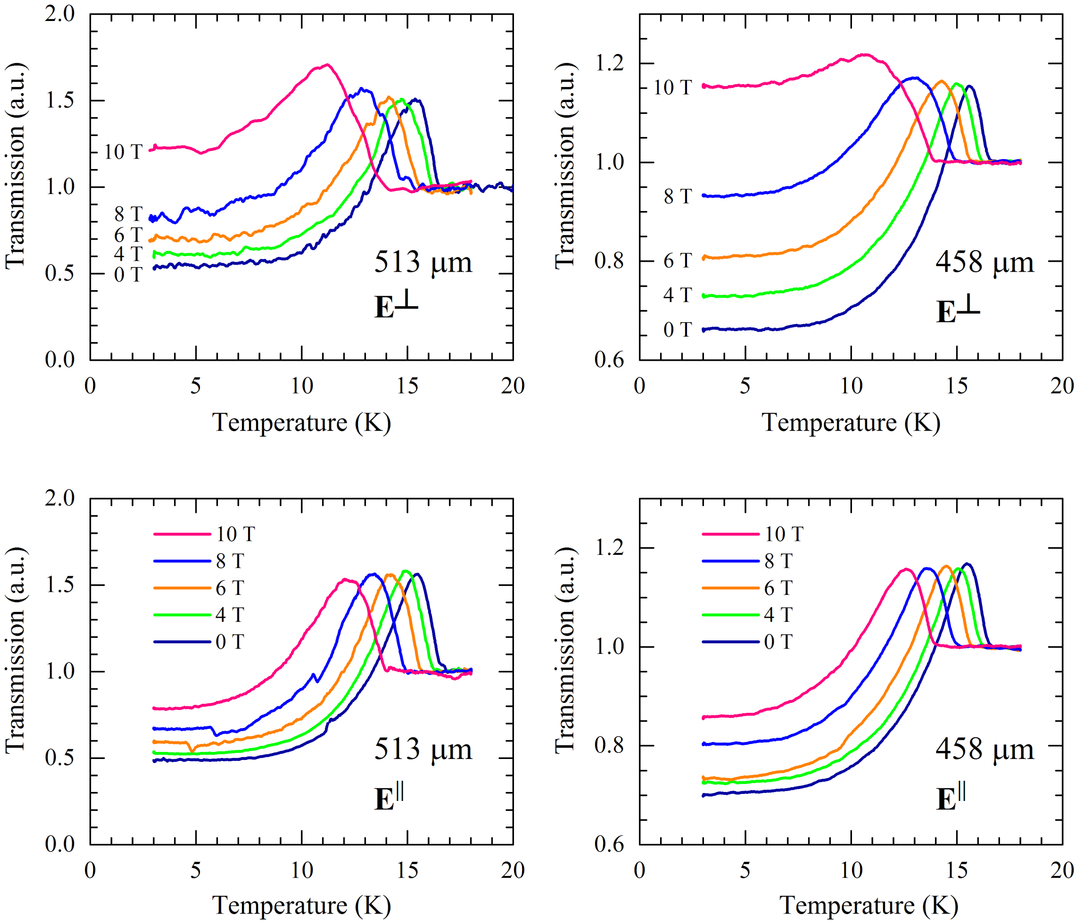

Figure 6.11: Transmission of NbN/sapphire sample in parallel magnetic field.

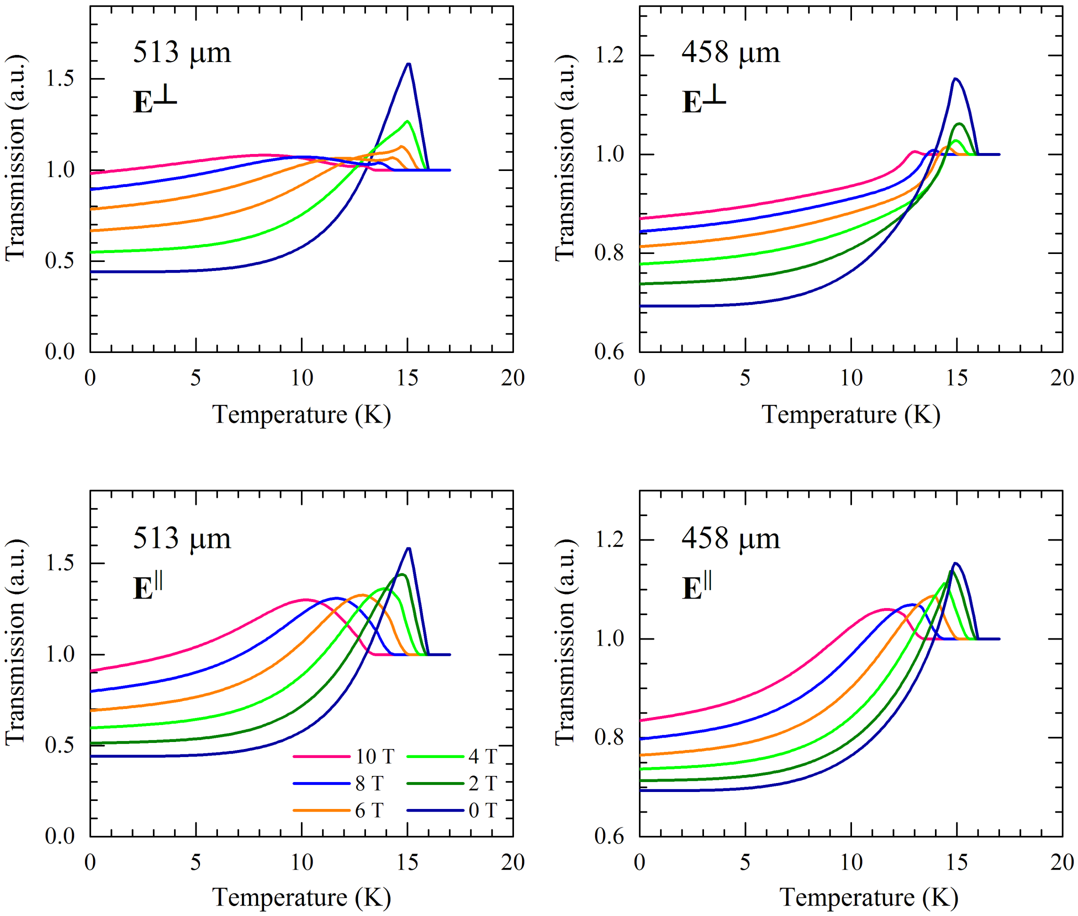

Figure 6.12: Transmission of NbN/sapphire sample in parallel magnetic field as calculated by the theoretical model [72].

6.3 Experiments with circular polarization

Although the experiments described above using a linearly polarized FIR/THz laser beam led to interesting and important results, it was clear that further progress towards fluxonics would require experimental data obtained with a circularly polarized beam that was not available. This prompted us to design and develop the missing part of our laboratory equipment: a terahertz circular polarizer. Functionality of the designed device was experimentally verified by the cyclotron resonance measurements shown in Section 5.7, and there is no doubt that our circular polarizer can be safely employed to study superconducting thin films. The measurement process with the THz circular polarizer involves several successive steps, some of which have already been described in detail in Chapters 4 and 5. First of all, a suitable FIR/THz laser line is tuned and the phase retarder is scanned for adjacent circular-polarization states. Since an actual handedness was not distinguished in the reported experiments, the states with the opposite sense of circular polarization are marked by letters A and B. Fast switching between the two retarder positions while sweeping temperature or magnetic field allows for a simultaneous measurement of transmitted radiation $\mathcal{T}_\mathrm{A}$ and $\mathcal{T}_\mathrm{B}$ for both circular polarization states A and B.

In experiments with the circularly polarized laser beam, a high-temperature superconducting sample YBCO/LAO was examined. The choice of the sample was stimulated by our effort to determine the effective mass of a superconducting vortex or, at the very least, to find out whether the proposed experimental method is suitable for this purpose. Some circular dichroism was already observed in thin films of YBCO, as reported by *Lihn et al.* [88]. However, their experiments were performed with elliptically polarized FIR radiation and they also did not provide a satisfactory explanation of their results. An attempt was made to interpret their data using a new theory of the vortex dynamics by *Koláček et al.* [20]. It was therefore quite natural to perform the test of our method on the thin epitaxial film of $\mathrm{YBa_2Cu_3O_{7-\delta}}$ deposited on a $\mathrm{LaAlO_3}$ substrate, abbreviated as YBCO/LAO, with a critical temperature of $T_\mathrm{c} = 87.6\ K$ (see Table 6.1).

6.3.1 Temperature dependence

Magneto-transmission data presented in this section were obtained by the laser thermal spectroscopy technique [83] in the Faraday geometry (see Figure 4.2 and 6.7). The sample temperature was set well above the critical temperature to ensure firmly defined initial conditions. While the superconducting film was in its normal state, a magnetic field was applied in a direction perpendicular to the sample surface. Subsequently the sample temperature was swept down and then returned to the starting point. A temperature controller ensured a sufficiently smooth and steady decrease of temperature with a sweep rate of 2.5 K/min, and an instantaneous temperature of the sample was recorded together with the measured transmission. The acquired data (see Figure 6.13) were cleaned from a random shot noise, smoothed, and interpolated at equidistant temperature points. Such data processing allows us to easily calculate the ratio $\mathcal{T}_{\mathrm{A}}/\mathcal{T}_{\mathrm{B}}$ of the measured curves.

The resulting temperature dependence of the transmission ratio is shown in Figure 6.14 for the laser line 311 µm and several magnetic fields. The transmission ratio $\mathcal{T}_{\mathrm{A}}/\mathcal{T}_{\mathrm{B}}$ measured in the zero field confirms the expected constant behavior as there is no asymmetry caused by the superconducting vortices. In nonzero fields, however, low-temperature circular dichroism is observed which onsets at approximately 85 K. It can be attributed to formation of superconducting vortices in the sample volume. The effect of differential transmission of A and B circular polarization is enhanced in higher applied fields as clearly seen at low temperatures in Figure 6.14. This increase is understandable, as the amount of vortices is proportional to the applied field.

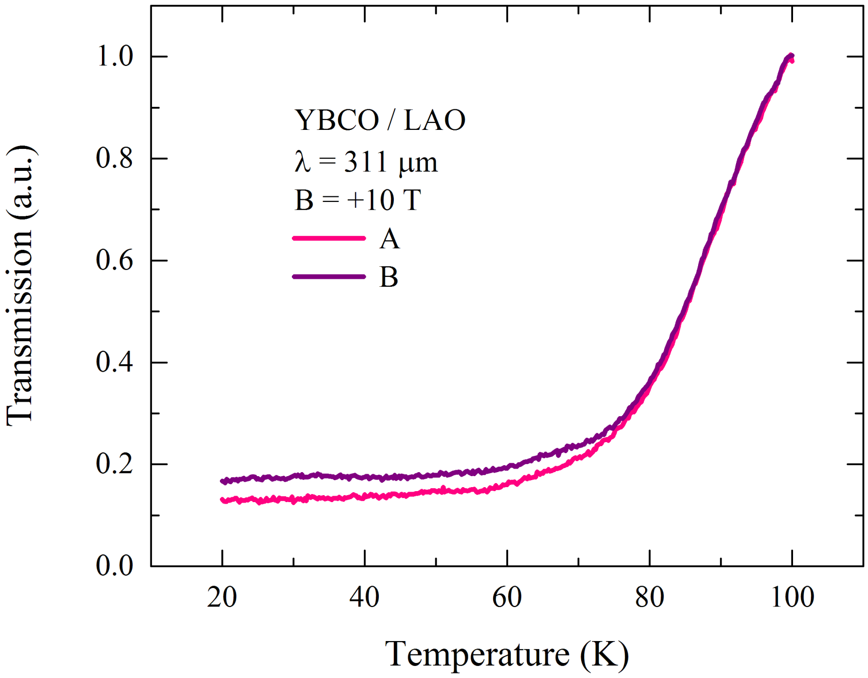

Figure 6.13: Normalized transmission $\mathcal{T}_{\mathrm{A}}$ and $\mathcal{T}_{\mathrm{B}}$ as measured for the A and B circular polarization.

6.3.2 Magnetic field dependence

Transmission of circularly polarized radiation was also measured as a function of magnetic field in the Faraday geometry as shown in Figure 4.2 and Figure 6.7. Since the experimental results depend on the history of the sample, it is necessary to define clearly how its initial state has been reached. The measurements were performed using two scenarios of setting the magnetic field and temperature. In the *field-cooled scenario*, the magnetic field is applied when the sample is in its normal state. Subsequently, the temperature is lowered to a desired value below T_{c}, whereas the applied field remains unchanged. When the sample temperature is sufficiently stabilized the experiment may proceed to the field-dependence

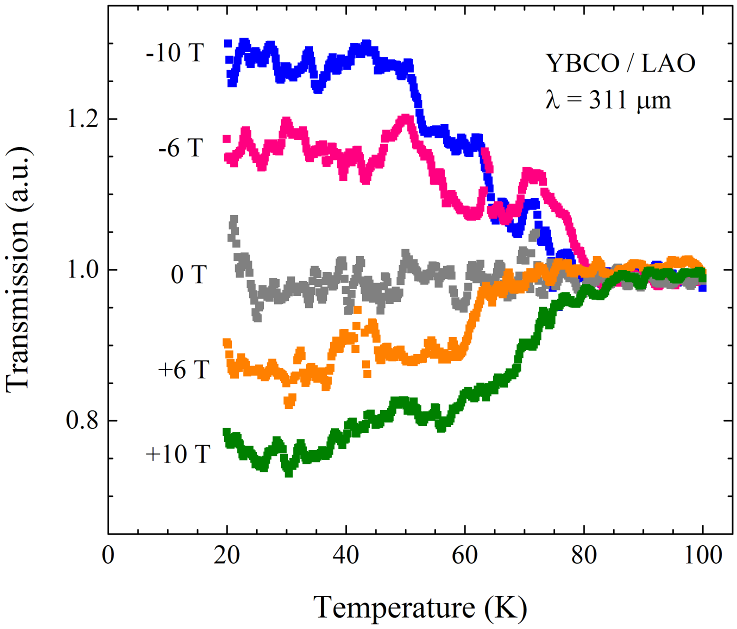

Figure 6.14: Transmission ratio $\mathcal{T}_\mathrm{A}/\mathcal{T}_\mathrm{B}$ measured at several magnetic fields plotted as a function of temperature.

measurement. The magnetic field is swept back and forth within the range of -10 T to +10 T using a ramp rate of 1 T/min. This process of the field cycling is referred to as a slow field oscillation. During the slow field cycling, the sample transmission is measured while fast alternating the sense of circular polarization. In the *zero-field-cooled scenario*, the sample is heated above the critical temperature and then cooled to a target temperature without applied magnetic field. Then the field is swept starting from the zero value and slowly cycled within the limits of -10 T to +10 T using the ramp rate of 1 T/min. The sample transmission is measured simultaneously for both circular polarizations in the same way as mentioned earlier.

A field-cooled measurement is displayed in Figure 6.15 for the FIR/THz laser line 311 µm. The sample was heated up to a temperature of 100 K and then cooled down to 20 K in a magnetic field of -10 T. When stabilized conditions were reached, the slow cycling of the magnetic field started while fast alternating the sense of circular polarization. The acquired data were cleaned from the shot noise, smoothed and normalized to the zero field transmission. The upper two panels of Figure 6.15 plot the resulting transmission data revealing a distinctly different shape for the opposite sense of circular polarization. In positive fields, the transmitted circular polarization A remains nearly unaffected by the applied magnetic field while the opposite polarization B shows an increasing transmission. A ratio $\mathcal{T}_\mathrm{A}/\mathcal{T}_\mathrm{B}$ of the corresponding curves with the opposite sense of circular polarization is displayed in the bottom panel.

Figure 6.16 shows an example of the zero-field-cooled measurement. Field dependence of transmission for the FIR/THz laser line 311 µm was obtained at a temperature of 20 K. The sample was cooled down in the zero field from 100 K

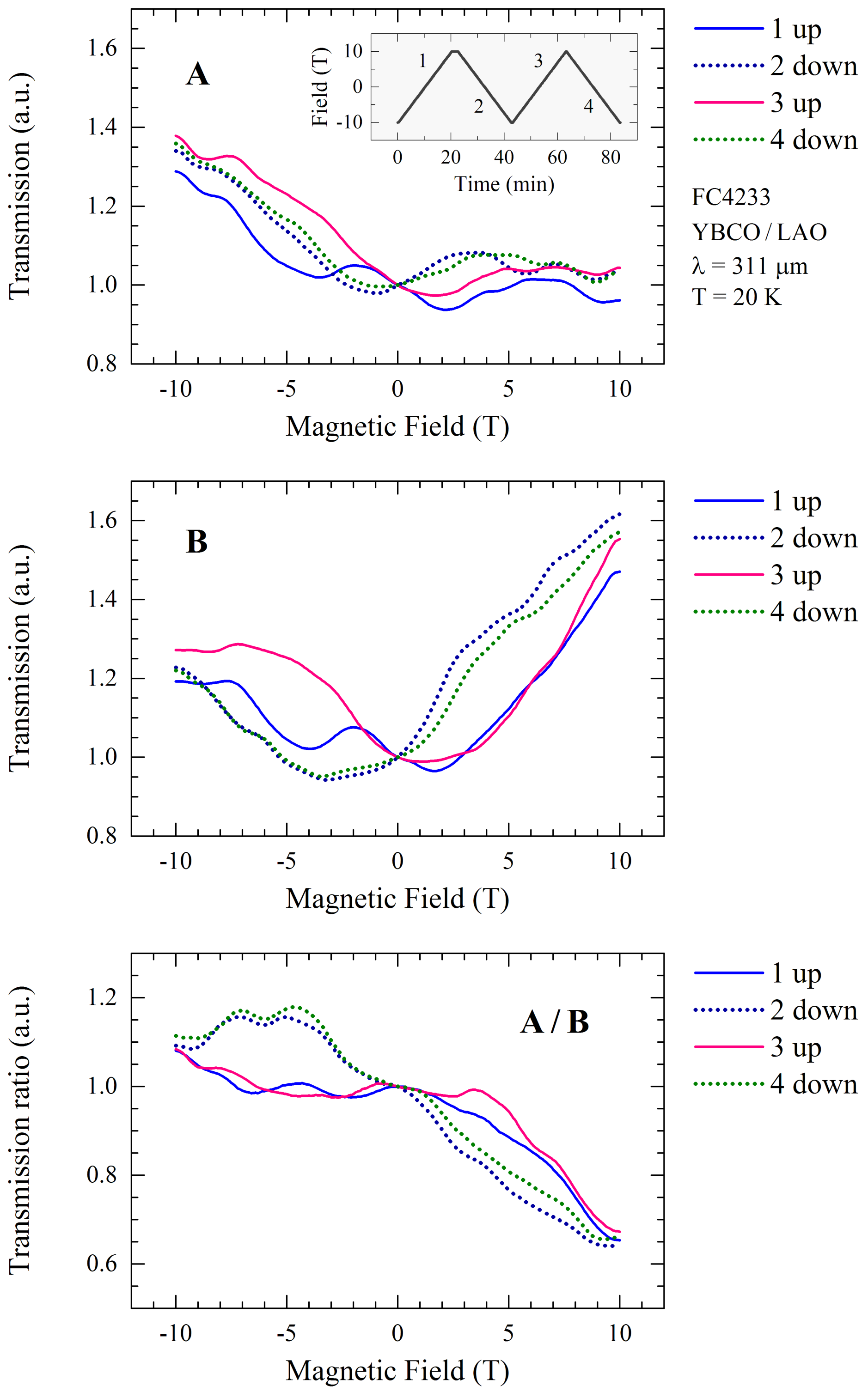

Figure 6.15: Field-cooled behavior of transmission. An YBCO/LAO sample was measured at temperature 20 K using a FIR laser line 311 µm. Symbols A and B denote the circular polarization of opposite handedness. The upper two panels show a normalized transmission $\mathcal{T}_\mathrm{A}$ and $\mathcal{T}_\mathrm{B}$, whereas the bottom panel displays a ratio of transmission curves $\mathcal{T}_\mathrm{A}/\mathcal{T}_\mathrm{B}$.

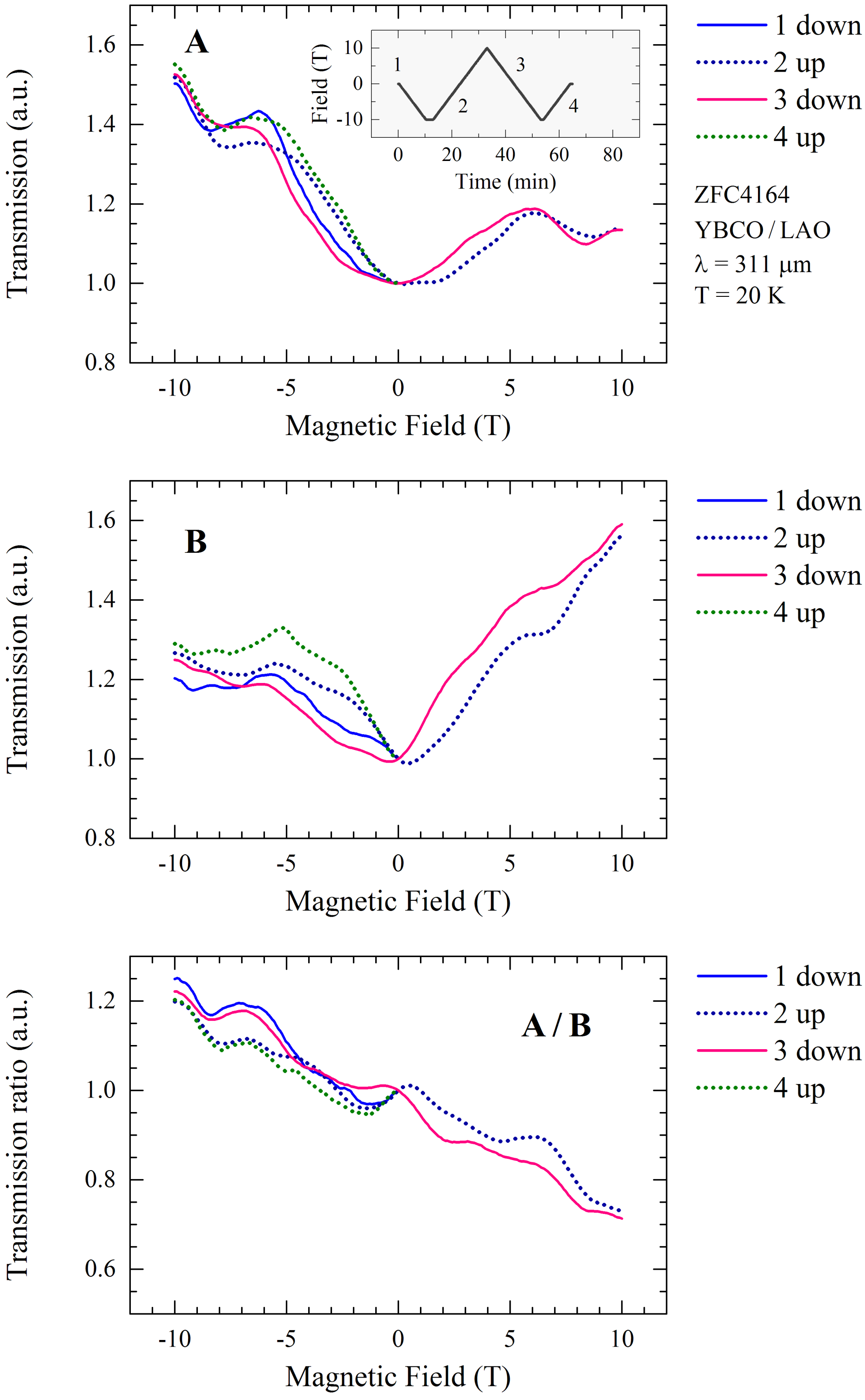

Figure 6.16: Zero-field-cooled behavior of transmission. An YBCO/LAO sample was measured at temperature 20 K using a FIR laser line 311 µm. Symbols A and B denote the circular polarization of opposite handedness. The upper two panels show a normalized transmission $\mathcal{T}_{\mathrm{A}}$ and $\mathcal{T}_{\mathrm{B}}$, whereas the bottom panel displays a ratio of transmission curves $\mathcal{T}_{\mathrm{A}}/\mathcal{T}_{\mathrm{B}}$.

to 20 K. As soon as the sample temperature was sufficiently stabilized, slow magnetic-field oscillations were started. The measured data were processed in the same way as described above, i.e. cleaned from the shot noise, smoothed and normalized to the zero field transmission. The overall transmission behavior is similar to that achieved when the sample is cooled in a magnetic field. Compared to the field-cooled data shown in Figure 6.15, a smaller hysteresis was found which may be explained by a lower amount of vortices penetrating inside the sample during the zero-field cooling scenario.

At first glance, the presented magneto-transmission data may seem confusing and unreproducible. A more detailed qualitative analysis, however, reveals some interesting patterns. *Brandt et al.* [89] showed that the magnetic field penetrating a thin superconducting strip is largely inhomogeneous and that its actual distribution depends strongly on the history of the external magnetic field. The local magnetic field determines the vortex density inside the superconducting film, which affects radiation transmitted through the sample. Therefore, an instantaneous field profile across the sample may provide a clue for interpreting the experimental data.

Let us introduce a coordinate system with the $+z$ axis pointing in the direction of the k-vector of the incident laser beam. In Faraday configuration shown Figure 6.7, it is also the direction along which the magnetic field is applied. In this coordinate system, the magnetic field oriented in the $+z$ axes is positive, while the opposite field is negative. Vortices with the magnetic flux oriented in the $+z$ axes are denoted as vortices, whereas those in $-z$ direction as antivortices. Now we can look closer to data obtained in the field-cooled scenario shown in Figure 6.15. At the beginning, the experiment starts in the negative applied field (-10 T) and a homogeneous distribution of antivortices is present with a density corresponding to the applied field. As the magnitude of magnetic field decreases to zero, antivortex density near the sample edge also decreases, while close to the center it remains unchanged. Even at zero applied field some antivortices are trapped inside the sample. When the applied field passes zero and starts to increase in the $+z$ direction, vortices begin to penetrate from the edge in the interior of the sample and antivortices are gradually annihilated. Vortices reach the sample center only at the so called full penetration field but with a smaller density than near the edge.

The situation is similar to the Bean model in Figure 2.2b but with the inhomogeneous distribution of the vortices corresponding rather to Figure 2.3. For example, in Figure 6.15, only downward parts of the magnetic field cycle, which lead to curves 2 and 4, have the same history with the same development of the field profile across the sample. Since the vortex density follows the local magnetic field distribution, only these two parts should also provide the same transmission. In Figure 6.17, the downward fragments of the field cycle are plotted for both opposite circular polarizations A and B with a suitably selected normalization point. We see that with such processing of measured transmission data, our experiment provides clear and reproducible results. Moreover, a broad transmission minimum become apparent for the circular polarization B in negative fields. It is expected that the minimum occurs at the lowest magnetic flux density where

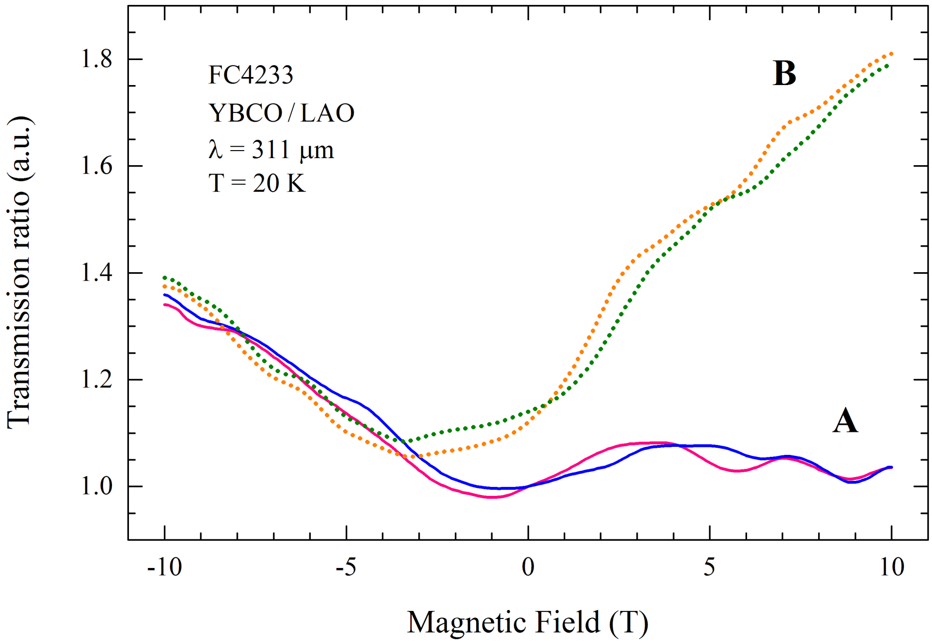

Figure 6.17: Suitably normalized transmission curves of circularly polarized waves of opposite handedness denoted by symbols A and B measured in the downward part of the field cycle.

the superconducting phase prevails. Its position is not observed at zero applied field, but rather shifted to negative values due to a remanence field generated by vortices trapped in the sample during the field cooling procedure. On the contrary, in the zero-field-cooled measurements shown in Figure 6.16, the observed minimum is closer to zero applied field, which can be explained by a lower amount of vortices captured in the sample cooled in the zero field.

Now we focus on the transmission ratio $\mathcal{T}_{\mathrm{A}}/\mathcal{T}_{\mathrm{B}}$ shown in the bottom panel of Figure 6.15. If the transmission is indifferent to the sense of circular polarization, we should obtain a constant value of $\mathcal{T}_{\mathrm{A}}/\mathcal{T}_{\mathrm{B}}$. However, a nonzero slope was observed with a slight hysteresis formed by upward and downward curves. Similar transmission curves were measured at several temperatures up to the normal state and plotted in Figure 6.18 for selected downward parts of the field-cycle. For greater clarity, $\mathcal{T}_{\mathrm{A}}/\mathcal{T}_{\mathrm{B}}$ curves obtained at different temperatures are plotted with a vertical offset. The slope steepness decreases with temperature and disappears in the normal state as clearly visible in Figure 6.19. This behavior is consistent with the observed temperature dependence of $\mathcal{T}_{\mathrm{A}}/\mathcal{T}_{\mathrm{B}}$ shown in Figure 6.14. Since a different transmission of the left and right-handed circular polarization is found in the superconducting state at nonzero magnetic fields, but is not seen in zero field or in the normal state, this phenomenon can be unambiguously associated with the existence of vortices. It has been sufficiently demonstrated that we observe features connected with the superconducting properties of studied films.

Figure 6.20 displays normalized transmission of the left-handed and right-handed circularly polarized radiation measured at the temperature of 40 K as a function of applied magnetic field. Repeated measurements are indicated by

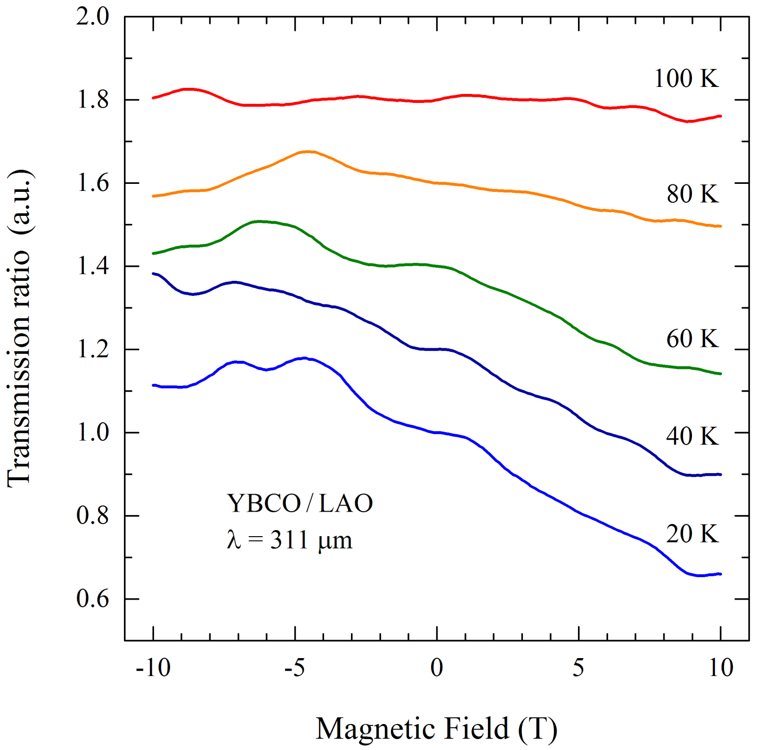

Figure 6.18: Transmission ratio $\mathcal{T}_{\mathrm{A}}/\mathcal{T}_{\mathrm{B}}$ measured at several sample temperatures. The curves are normalized to zero field transmission and shifted vertically by multiples of 0.2. For simplicity, only selected data obtained in the downward part of the field cycle are displayed.

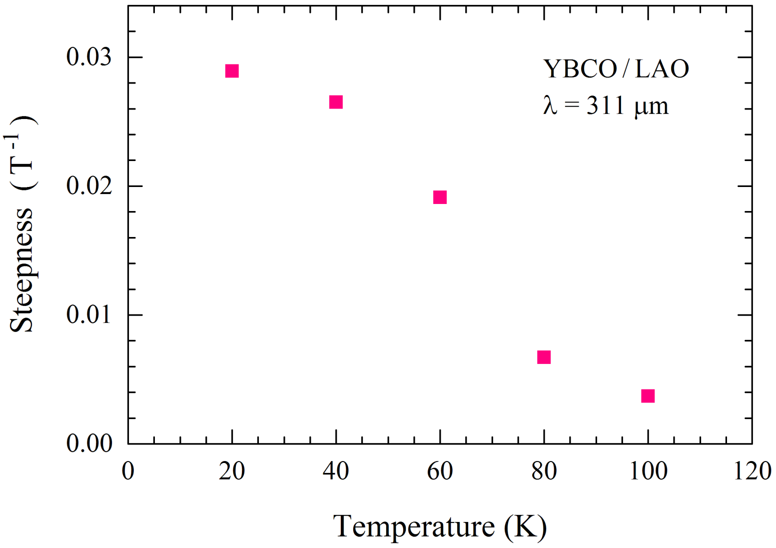

Figure 6.19: Steepness of the field dependent transmission ratio $\mathcal{T}_{\mathrm{A}}/\mathcal{T}_{\mathrm{B}}$ as a function of temperature. Points were obtained from a linear fit of down-field transmission data in Figure 6.18.

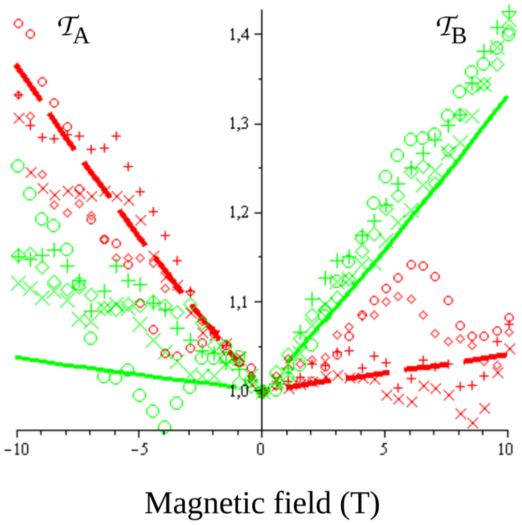

Figure 6.20: Transmission of YBCO/LAO sample at 40 K for two opposite circular polarizations using a FIR/THz laser line 311 µm (points). Theoretical calculations according to [20] are shown as solid and dashed lines.

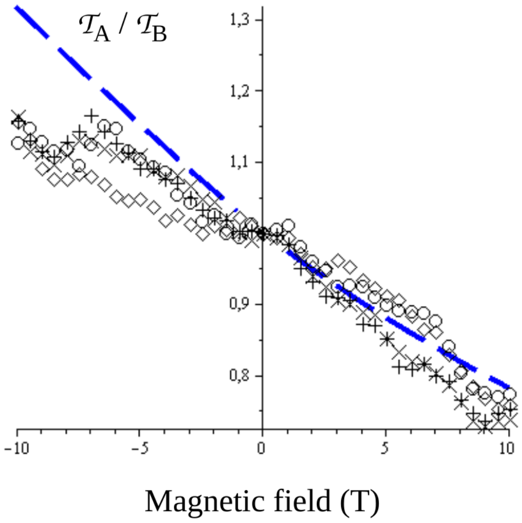

Figure 6.21: Transmission ratio $\mathcal{T}_\mathrm{A}/\mathcal{T}_\mathrm{B}$ for YBCO/LAO sample at 40 K for two opposite circular polarizations using a FIR/THz laser line 311 µm (points). Theoretical calculation according to [20] is shown as a dashed line.

different point symbols, whereas theoretical curves are shown in solid and dashed lines.

We attempted to explain the experimental data using a somewhat controversial theory of high-frequency vortex dynamics [20], which is not yet widely accepted. Some vortex parameters necessary for theoretical calculations of transmission are not well known for the studied sample and must be estimated. In type-II superconductors, a pinning mechanism may constrain the vortex motion to a small area around the pinning centers. However, a depinning frequency of the order of 10 GHz was observed in YBCO thin films with only a weak temperature dependence [90] and thus it seems that in FIR/THz region a zero-pinning limit is appropriate. Another problem is that the vortex motion can be retarded by viscose damping. Already in 1965 *Bardeen and Stephen* [91] suggested a simplified model describing motion of vortices in superconductors and provided a theoretical formula for the viscosity coefficient. However, *Parks et al.* [92] found that the experimental low-temperature viscosity in YBCO thin films was about 20 times smaller than the Bardeen-Stephen theoretical prediction for conventional superconductors. In our calculations, we use a value of $\eta = 7.5 \times 10^{-8}\,\mathrm{kg\,m^{-1}s^{-1}}$, which is approximately 8 times smaller than the viscosity provided by the Bardeen-Stephen model and seems appropriate for our sample at a temperature of 40 K. The calculated transmission curves, and in particular the calculated $\mathcal{T}_\mathrm{A}/\mathcal{T}_\mathrm{B}$ ratio shown in Figure 6.21, strongly depend on the last free parameter, the effective mass of vortices. Reasonable agreement of theoretical estimates with experimental data was found for $m_\mathrm{v} \approx 2.0 \times 10^{-19}\,\mathrm{kg\,m^{-1}} \approx 2.2 \times 10^{11}\,\mathrm{m_e\,m^{-1}}$. However, it is only a preliminary result that does not take into account the above-mentioned problems of field inhomogeneity within the superconducting sample. For this reason, the observed hysteresis loops could not be theoretically reproduced. We are currently solving these problems and preparing a manuscript of the relevant paper. The preliminary estimate of the effective vortex mass has already been presented at the ICSM'2018 conference [73].

The present method allows the measurement of circular dichroism in type-II superconductors and seems to be a suitable tool for collecting experimental data relevant to the high-frequency study of vortex dynamics. The obtained magneto-transmission provides valuable information, from which it is possible to estimate the effective vortex mass in superconducting thin films. As already outlined in the Introduction, it is of utmost importance for future applications in fluxonics. Superconductive digital circuits based on fluxon manipulation and processing will require detailed knowledge of fundamental fluxon parameters. In these new technologies, the effective vortex mass undoubtedly will be of similar importance as the effective electron mass had and still has for conventional semiconductor electronics.

7 Conclusion

Being motivated by the potential use of type II superconductors for future practical applications such as fluxonics, we have investigated some of their physical properties, via their interactions with linearly and circularly polarized THz irradiation, over a broad range of temperatures and externally applied magnetic fields in various geometries. To be able to carry out such a fundamental experimental research, we have built a unique magneto-optical laboratory based on both commercially available components (such as a broadband THz laser, heavy duty optical table, superconducting Helmholtz magnet producing horizontal magnetic field up to 10 T in optical helium bath cryostat, cryogenic insert capable of reaching and stabilizing temperatures down to 1.8 K, vacuum pumps, helium recovery lines, beam splitter, pyroelectric detector, temperature and magnetic field sensors, and lock-in amplifiers) and specially developed hardware and control/measurement/analysis software. The author of this thesis was either fully in charge or took a substantial part in all these developments, as well as in subsequent experiments, data analysis and physical interpretations of the obtained results, reported at international conferences and published in original research articles in international impacted journals such as Physical Review B, Physica B and C and Review of Scientific Instruments.

The most significant physical results are as follows. Transmission of a monochromatic linearly polarized laser beam with frequencies above and below an optical gap was measured both below and above T_c of the thin-film NbN samples deposited on a Si substrate and of a high quality epitaxial film of the NbN superconductor deposited on a birefringent sapphire substrate. For photon energies lower than the optical gap, detailed temperature measurements in zero field provide BCS-like curves with a pronounced peak below the critical temperature T_c. In accordance with the BCS model, the temperature peak disappears as the energy of the incident radiation is increased above the gap. In magnetic fields perpendicular to the sample, i.e., in the Faraday experimental geometry, the temperature dependence of transmission is modified because the gap is suppressed and vanishes at upper critical field. In addition, the presence of quantized vortices in the superconducting film substantially changes the shape of the temperature curves. In the parallel Voigt geometry, a significant difference is found between transmitted intensities of beams linearly polarised parallel with and perpendicular to the direction of applied magnetic field that fixes the direction of the vortex axes in the superconducting thin NbN film. A thorough analysis of the data in frame of the developed theoretical models has been performed and published.

In order to push our research towards possible determination of the effective vortex mass, a precise polarization converting device fully tunable in a broad range of THz frequencies was needed. This device has been designed and developed by the author of this thesis over the last two years, covering at least the band of 0.25 – 7.5 THz and is now fully functioning for linear-to-circular polarization conversion in magneto-optical experiments with the FIR/THz gas laser source. The polarization converter utilizes a scheme with a variable phase retarder composed of a wire-grid polarizer and a parallel moving mirror. A practical method based on detailed analysis of the lock-in signal generated by the rotating analyzer was elaborated for precise circular polarization adjustment. The technique provides independent and effective control of the polarization output of the phase retarder, and it is suitable not only for free-standing grids, but also for grids on substrates. The method is applicable even if the distance between the mirror and the wire-grid polarizer cannot be exactly determined or is biased by an unknown offset and allows one to achieve an ellipticity as high as 0.99, which is very close to perfectly circular polarization. The experimental functionality of the polarizer was verified in practice, via detection of the cyclotron resonance in the two-dimensional electron gas. The presented method of signal analysis is not limited to the THz spectral region, but generally applies to the modulation of the polarized beam with a rotating analyzer.

In Faraday magneto-optical geometry, the device was used for measurements of transmission of the circularly polarized THz beam through a superconducting $YBa_2Cu_3O_{7-\delta}$ thin films in externally applied magnetic fields. The data confirm the presence of measurable circular dichroism, which is most likely caused by motion of the vortex lattice. We believe that, using purposely measured data obtained in systematic studies it will be possible to accurately evaluate the effective vortex mass; a preliminary estimation has already been presented at the ICSM'2018 conference [73].

Bibliography

[1] H. Thomas, A. Marian, A. Chervyakov, S. Stückrad, D. Salmieri, and C. Rubbia, “Superconducting transmission lines – sustainable electric energy transfer with higher public acceptance?,” *Renewable and Sustainable Energy Reviews*, vol. 55, pp. 59 – 72, 2016.

[2] R. P. Feynman, “Simulating physics with computers,” *International Journal of Theoretical Physics*, vol. 21, pp. 467–488, 1982.

[3] Intel Corp., https://newsroom.intel.com/press-kits/quantum-computing/.

[4] IBM Corporation, https://www.research.ibm.com/ibm-q/.

[5] Google LLC, https://ai.google/research/.

[6] D-Wave Systems Inc., https://www.dwavesys.com/.

[7] T. Golod, A. Iovan, and V. M. Krasnov, “Single abrikosov vortices as quantized information bits,” *Nature Communications*, vol. 6, 2015.

[8] FLUXONICS Foundry, http://www.fluxonics.de/fluxonics-home/mission/.

[9] H. Suhl, “Inertial mass of a moving fluxoid,” *Phys. Rev. Lett.*, vol. 14, pp. 226–229, 1965.

[10] E. Šimánek, “Inertial mass of a fluxon in a deformable superconductor,” *Physics Letters A*, vol. 154, pp. 309 – 311, 1991.

[11] J.-M. Duan and E. Šimánek, “Inertial mass of a fluxon in superconductors due to the strain field,” *Physics Letters A*, vol. 190, pp. 118 – 122, 1994.

[12] E. M. Chudnovsky and A. B. Kuklov, “Inertial mass of the abrikosov vortex,” *Phys. Rev. Lett.*, vol. 91, p. 067004, 2003.

[13] J. H. Han, J. S. Kim, M. J. Kim, and P. Ao, “Effective vortex mass from microscopic theory,” *Phys. Rev. B*, vol. 71, p. 125108, 2005.

[14] T. Simula, “Vortex mass in a superfluid,” *Physical Review A*, vol. 97, FEB 6 2018.

[15] L. Bottura, “A practical fit for the critical surface of nbti,” *IEEE Transactions on Applied Superconductivity*, vol. 10, pp. 1054–1057, 2000.

[16] A. A. Abrikosov, “On the magnetic properties of superconductors of the second group,” *Sov. Phys. JETP*, vol. 5, pp. 1174–1182, 1957. [Zh. Eksp. Teor. Fiz. 32, 1442 (1957)].

[17] C. P. Bean, "Magnetization of hard superconductors," *Phys. Rev. Lett.*, vol. 8, pp. 250–253, 1962.

[18] C. P. Bean, "Magnetization of high-field superconductors," *Rev. Mod. Phys.*, vol. 36, pp. 31–39, 1964.

[19] J. I. Vestgården, P. Mikheenko, Y. M. Galperin, and T. H. Johansen, "Nonlocal electrodynamics of normal and superconducting films," *New Journal of Physics*, vol. 15, p. 093001, 2013.

[20] J. Koláček and E. Kawate, "High frequency vortex dynamics and magnetoconductivity of high temperature superconductors," *Physics Letters A*, vol. 260, pp. 300–307, 1999.

[21] W. Zimmermann, E. H. Brandt, M. Bauer, E. Seider, and L. Genzel, "Optical conductivity of BCS superconductors with arbitrary purity," *Physica C: Superconductivity*, vol. 183, no. 1, pp. 99 – 104, 1991.

[22] R. H. Muller, "Definitions and conventions in ellipsometry," *Surface Science*, vol. 16, pp. 14 – 33, 1969.

[23] R. Atkinson and P. H. Lissberger, "Sign conventions in magneto-optical calculations and measurements," *Appl. Opt.*, vol. 31, pp. 6076–6081, 1992.

[24] M. Born and E. Wolf, *Principles of Optics.* Cambridge University Press, 7 ed., 1999.

[25] O. S. Heavens, *Optical Properties of Thin Solid Films.* Dover Publications, 1991.

[26] S. Rytov, "Electromagnetic properties of a finely stratified medium," *Soviet Physics JEPT*, vol. 2, pp. 466–475, 1956.

[27] J. C. M. Garnett, "Colours in metal glasses and in metallic films," *Philosophical Transactions of the Royal Society of London A*, vol. 203, pp. 385–420, 1904.

[28] G. L. Carr, S. Perkowitz, and D. B. Tanner, "Far-infrared properties of inhomogeneous materials," *Infrared and millimeter waves*, vol. 13, pp. 171–263, 1985.

[29] R. Tesař, M. Šindler, J. Koláček, and L. Skrbek, "Terahertz wire-grid circular polarizer tuned by lock-in detection method," 2018. *Review of Scientific Instruments*, in print.

[30] R. Tesař, J. Koláček, Z. Šimša, M. Šindler, L. Skrbek, K. Il'in, and M. Siegel, "Terahertz transmission of NbN superconductor thin film," *Physica C*, vol. 470, pp. 932 – 934, 2010.

[31] W. J. Witteman, *The CO_2 Laser.* Springer Series in Optical Sciences, Springer Berlin Heidelberg, 2013.

[32] K. J. Button, *Infrared and Millimeter Waves V7: Coherent Sources and Applications, Part-II*. Elsevier Science, 1983.

[33] E. R. Mueller, *Optically Pumped Terahertz (THz) Lasers*, pp. 1–22. American Cancer Society, 2016.

[34] K. J. Button, *Reviews of Infrared and Millimeter Waves: Volume 2 Optically Pumped Far-Infrared Lasers*. Reviews of infrared and millimeter waves, Springer US, 2013.

[35] N. G. Douglas, *Millimetre and Submillimetre Wavelength Lasers: A Handbook of cw Measurements*. Springer Series in Optical Sciences, Springer Berlin Heidelberg, 2014.

[36] G. Moruzzi, *Microwave, Infrared, and Laser Transitions of Methanol Atlas of Assigned Lines from 0 to 1258 cm^{-1}*. CRC Press, 2018.

[37] G. Moruzzi, J. C. Silos Moraes, and F. Strumia, "Far infrared laser lines and assignments of CH_3OH: a review," *International Journal of Infrared and Millimeter Waves*, vol. 13, pp. 1269–1312, 1992.

[38] D. Pereira, J. C. S. Moraes, E. M. Telles, A. Scalabrin, F. Strumia, A. Moretti, G. Carelli, and C. A. Massa, "A review of optically pumped far-infrared laser lines from methanol isotopes," *International Journal of Infrared and Millimeter Waves*, vol. 15, pp. 1–44, 1994.

[39] S. C. Zerbetto and E. C. C. Vasconcellos, "Far infrared laser lines produced by methanol and its isotopic species: A review," *International Journal of Infrared and Millimeter Waves*, vol. 15, pp. 889–933, 1994.

[40] J. Gallagher, M. Blue, B. Bean, and S. Perkowitz, "Tabulation of optically pumped far infrared laser lines and applications to atmospheric transmission," *Infrared Physics*, vol. 17, pp. 43 – 55, 1977.

[41] J.-B. Masson and G. Gallot, "Terahertz achromatic quarter-wave plate," *Opt. Lett.*, vol. 31, pp. 265–267, 2006.

[42] J. K. Gansel, M. Thiel, M. S. Rill, M. Decker, K. Bade, V. Saile, G. von Freymann, S. Linden, and M. Wegener, "Gold helix photonic metamaterial as broadband circular polarizer," *Science*, vol. 325, pp. 1513–1515, 2009.

[43] J. Howard, W. A. Peebles, and N. C. Luhmann, "The use of polarization transforming reflectors for far-infrared and millimeter waves," *International Journal of Infrared and Millimeter Waves*, vol. 7, pp. 1591–1603, 1986.

[44] C. Prigent, P. Abba, and M. Cheudin, "A quasi-optical polarization rotator," *International Journal of Infrared and Millimeter Waves*, vol. 9, pp. 477–490, 1988.

[45] A. R. Harvey, "A quasi-optical universal polarizer," *International Journal of Infrared and Millimeter Waves*, vol. 14, pp. 1–16, 1993.

[46] H. Shinnaga, M. Tsuboi, and T. Kasuga, "Quasi-optical reflective polarimeter for wide millimeter-wave band," in *Millimeter and Submillimeter Waves IV*, vol. 3465, SPIE, 1998.

[47] G. Kozlov and A. Volkov, *Coherent source submillimeter wave spectroscopy.* Berlin, Heidelberg: Springer Berlin Heidelberg, 1998.

[48] Y.-S. Lee, *Principles of terahertz science and technology.* Springer, 2009.

[49] D. T. Chuss, E. J. Wollack, R. Henry, H. Hui, A. J. Juarez, M. Krejny, S. H. Moseley, and G. Novak, "Properties of a variable-delay polarization modulator," *Appl. Opt.*, vol. 51, no. 2, pp. 197–208, 2012.

[50] D. T. Chuss, E. J. Wollack, G. Novak, G. Pisano, J. R. Eimer, S. H. Moseley, M. Krejny, and K. U-Yen, "Phase-controlled polarization modulators," in *Millimeter, Submillimeter, and Far-Infrared Detectors and Instrumentation for Astronomy VI*, vol. 8452, SPIE, 2012.

[51] D. T. Chuss, E. J. Wollack, G. Pisano, S. Ackiss, K. U-Yen, and M. wah Ng, "A translational polarization rotator," *Appl. Opt.*, vol. 51, no. 28, pp. 6824–6830, 2012.

[52] N. Amer, W. C. Hurlbut, B. J. Norton, Y.-S. Lee, and T. B. Norris, "Generation of terahertz pulses with arbitrary elliptical polarization," *Applied Physics Letters*, vol. 87, p. 221111, 2005.

[53] A. C. Strikwerda, K. Fan, H. Tao, D. V. Pilon, X. Zhang, and R. D. Averitt, "Comparison of birefringent electric split-ring resonator and meanderline structures as quarter-wave plates at terahertz frequencies," *Opt. Express*, vol. 17, no. 1, pp. 136–149, 2009.

[54] Y. Yu, Z. Yang, M. Zhao, and P. Lu, "Broadband optical circular polarizers in the terahertz region using helical metamaterials," *Journal of Optics*, vol. 13, MAY 2011.

[55] Y. Zhang, Y. Feng, B. Zhu, J. Zhao, and T. Jiang, "Switchable quarter-wave plate with graphene based metamaterial for broadband terahertz wave manipulation," *Opt. Express*, vol. 23, no. 21, pp. 27230–27239, 2015.

[56] A. K. Kaveev, G. I. Kropotov, D. I. Tsypishka, I. A. Tzibizov, I. A. Vinerov, and E. G. Kaveeva, "Tunable wavelength terahertz polarization converter based on quartz waveplates," *Appl. Opt.*, vol. 53, no. 24, pp. 5410–5415, 2014.

[57] D. Wang, L. Zhang, Y. Gu, M. Q. Mehmood, Y. Gong, A. Srivastava, L. Jian, T. Venkatesan, C.-W. Qiu, and M. Hong, "Switchable ultrathin quarter-wave plate in terahertz using active phase-change metasurface," *Scientific Reports*, vol. 5, OCT 7 2015.

[58] B. Zhang and Y. Gong, "Achromatic terahertz quarter waveplate based on silicon grating," *Opt. Express*, vol. 23, no. 11, pp. 14897–14902, 2015.

[59] W. Mo, X. Wei, K. Wang, Y. Li, and J. Liu, “Ultrathin flexible terahertz polarization converter based on metasurfaces,” *Opt. Express*, vol. 24, no. 12, pp. 13621–13627, 2016.

[60] L. Wang, S. Ge, W. Hu, M. Nakajima, and Y. Lu, “Tunable reflective liquid crystal terahertz waveplates,” *Opt. Mater. Express*, vol. 7, no. 6, pp. 2023–2029, 2017.

[61] Y. Jiang, L. Wang, J. Wang, C. N. Akwuruoha, and W. Cao, “Ultra-wideband high-efficiency reflective linear-to-circular polarization converter based on metasurface at terahertz frequencies,” *Opt. Express*, vol. 25, no. 22, pp. 27616–27623, 2017.

[62] E. Palik, *Handbook of Optical Constants of Solids.* Academic Press, 1998.

[63] H.-J. Hagemann, W. Gudat, and C. Kunz, “Optical constants from the far infrared to the x-ray region: Mg, Al, Cu, Ag, Au, Bi, C, and Al_2O_33,” *J. Opt. Soc. Am.*, vol. 65, no. 6, pp. 742–744, 1975.

[64] R. Vogelgesang, “Lock-in amplifier theory,” Stuttgart, 2004.

[65] T. C. Choy, *Effective Medium Theory: Principles and Applications.* Oxford University Press, 2015.

[66] Tydex J.S.Co., URL: www.tydex.com.

[67] G. Bartsch, *Optically detected cyclotron resonance in a single GaAs/AlGaAs heterojunction.* PhD thesis, Technical university Dortmund, 2011.

[68] W. Nakwaski, “Effective masses of electrons and heavy holes in GaAs, InAs, AlAs and their ternary compounds,” *Physica B*, vol. 210, no. 1, pp. 1 – 25, 1995.

[69] M. Šindler, R. Tesař, J. Koláček, L. Skrbek, and Z. Šimša, “Far-infrared transmission of a superconducting NbN film,” *Phys. Rev. B*, vol. 81, p. 184529, 2010.

[70] R. Tesař, M. Šindler, K. Il’in, J. Koláček, M. Siegel, and L. Skrbek, “Terahertz thermal spectroscopy of a NbN superconductor,” *Phys. Rev. B*, vol. 84, p. 132506, 2011.

[71] M. Šindler, R. Tesař, J. Koláček, and L. Skrbek, “Interpretation of transmission through type ii superconducting thin film on dielectric substrate as observed by laser thermal spectroscopy,” *Physica C: Superconductivity*, vol. 483, pp. 127 – 135, 2012.

[72] M. Šindler, R. Tesař, J. Koláček, and L. Skrbek, “Anisotropic behaviour of transmission through thin superconducting NbN film in parallel magnetic field,” *Physica C*, vol. 533, pp. 154 – 157, 2017.

[73] R. Tesař, J. Koláček, and M. Šindler, “Circular dichroism in thin YBaCuO film observed in the terahertz range,” 2018. International Conference on Superconductivity and Magnetism, Antalya, poster.

[74] M. Šindler, R. Tesař, J. Koláček, P. Szabó, P. Samuely, V. Hašková, C. Kadlec, F. Kadlec, and P. Kužel, “Far-infrared electrodynamics of thin superconducting NbN film in magnetic fields,” *Superconductor Science and Technology*, vol. 27, p. 055009, 2014.

[75] M. P. Mathur, D. W. Deis, and J. R. Gavaler, “Lower critical-field measurements in NbN bulk and thin-films,” *Journal of Applied Physics*, vol. 43, p. 3158, 1972.

[76] Z. Wang, A. Kawakami, Y. Uzawa, and B. Komiyama, “Superconducting properties and crystal structures of single-crystal niobium nitride thin films deposited at ambient substrate temperature,” *Journal of Applied Physics*, vol. 79, pp. 7837–7842, 1996.

[77] A. Engel, A. D. Semenov, H.-W. Huebers, K. Il’in, and M. Siegel, “Fluctuation effects in superconducting nanostrips,” *Physica C*, vol. 444, pp. 12–18, 2006.

[78] A. Semenov, B. Günther, U. Böttger, H.-W. Hübers, H. Bartolf, A. Engel, A. Schilling, K. Ilin, M. Siegel, R. Schneider, D. Gerthsen, and N. A. Gippius, “Optical and transport properties of ultrathin NbN films and nanostructures,” *Phys. Rev. B*, vol. 80, p. 054510, 2009.

[79] Y. Ikebe, R. Shimano, M. Ikeda, T. Fukumura, and M. Kawasaki, “Vortex dynamics in a NbN film studied by terahertz spectroscopy,” *Phys. Rev. B*, vol. 79, p. 174525, 2009.

[80] M. Beck, M. Klammer, S. Lang, P. Leiderer, V. V. Kabanov, G. N. Gol’tsman, and J. Demsar, “Energy-gap dynamics of superconducting NbN thin films studied by time-resolved terahertz spectroscopy,” *Phys. Rev. Lett.*, vol. 107, p. 177007, 2011.

[81] K. I. Sim, Y. C. Jo, T. Ha, J. H. Kim, J. H. Kim, and H. Yamamori, “Terahertz electrodynamics and superconducting energy gap of NbN,” *Journal of the Korean Physical Society*, vol. 71, pp. 571–574, 2017.

[82] M. Tinkham, *Introduction to Superconductivity.* Dover Books on Physics Series, Dover Publications, 2004.

[83] G. D. Holah and S. Perkowitz, “Far infrared laser thermal spectroscopy of superconductors,” *International Journal of Infrared and Millimeter Waves*, vol. 2, pp. 581–586, 1981.

[84] E. V. Loewenstein, D. R. Smith, and R. L. Morgan, “Optical constants of far infrared materials. 2: Crystalline solids,” *Appl. Opt.*, vol. 12, pp. 398–406, 1973.

[85] M. Šindler, *Properties of superconductors in the terahertz region.* PhD thesis, Faculty of Mathematics and Physics, Charles University in Prague, 2012.

[86] J. R. Clem, “Simple model for the vortex core in a type II superconductor,” *Journal of Low Temperature Physics*, vol. 18, pp. 427–434, 1975.

[87] R. B. G. Kramer, G. W. Ataklti, V. V. Moshchalkov, and A. V. Silhanek, “Direct visualization of the Campbell regime in superconducting stripes,” *Phys. Rev. B*, vol. 81, p. 144508, 2010.

[88] H.-T. S. Lihn, S. Wu, H. D. Drew, S. Kaplan, Q. Li, and D. B. Fenner, “Measurement of the far-infrared magnetoconductivity tensor of superconducting YBaCuO thin films,” *Phys. Rev. Lett.*, vol. 76, pp. 3810–3813, 1996.

[89] E. H. Brandt and M. Indenbom, “Type-II-superconductor strip with current in a perpendicular magnetic field,” *Phys. Rev. B*, vol. 48, pp. 12893–12906, 1993.

[90] M. Golosovsky, M. Tsindlekht, H. Chayet, and D. Davidov, “Vortex depinning frequency in YBaCuO superconducting thin films: Anisotropy and temperature dependence,” *Phys. Rev. B*, vol. 50, pp. 470–477, 1994.

[91] J. Bardeen and M. J. Stephen, “Theory of the motion of vortices in superconductors,” *Phys. Rev.*, vol. 140, pp. A1197–A1207, 1965.

[92] B. Parks, S. Spielman, J. Orenstein, D. T. Nemeth, F. Ludwig, J. Clarke, P. Merchant, and D. J. Lew, “Phase-sensitive measurements of vortex dynamics in the terahertz domain,” *Phys. Rev. Lett.*, vol. 74, pp. 3265–3268, 1995.

List of abbreviations

Abbreviations

YBCO	yttrium barium copper oxide, $YBa_2Cu_3O_{7-\delta}$
LAO	lanthanum aluminate, $LaAlO_3$
HTS	high-temperature superconductor
LTS	low-temperature superconductor
BCS	Bardeen-Cooper-Schrieffer (theory)
IR	infrared
FIR	far infrared
RHC, RHCP	right-hand circular (polarization)
LHC, LHCP	left-hand circular (polarization)

Fundamental physical constants

$c = 2.997\,925 \times 10^{8}\,\mathrm{m\,s^{-1}}$	speed of light in vacuum
$e = 1.602\,176\,6 \times 10^{-19}\,\mathrm{C}$	elementary charge
$h = 6.626\,070\,040 \times 10^{-34}\,\mathrm{J\,s}$	Planck constant
$\hbar = \frac{h}{2\pi} = 1.054\,571\,800 \times 10^{-34}\,\mathrm{J\,s\,rad^{-1}}$	reduced Planck constant
$\Phi_0 = \frac{h}{2e} = 2.067\,833\,831 \times 10^{-15}\,\mathrm{Wb}$	magnetic flux quantum
$k_\mathrm{B} = 1.380\,648\,52 \times 10^{-23}\,\mathrm{JK^{-1}}$	Boltzmann constant
$m_\mathrm{e} = 9.109\,383\,56 \times 10^{-31}\,\mathrm{kg}$	electron rest mass

Symbols

E	electric vector
k	k-vector
ω	angular frequency
t	time
$\mathcal{T}$	transmission
$\mathcal{R}$	reflection
$\mathcal{A}$	absorption
B	applied magnetic field
H_a	applied magnetic field
H_p	full penetration magnetic field
m_v	effective vortex mass
T	temperature
T_c	critical temperature
B_c1	lower critical field
B_c1	upper critical field
Δ_0	BCS energy gap at zero temperature

Selected publications

1. R. Tesař, M. Šindler, J. Koláček, and L. Skrbek, Terahertz wire-grid circular polarizer tuned by lock-in detection method, *Review of Scientific Instruments* (2018), in print.

2. M. Šindler, R. Tesař, J. Koláček, L. Skrbek, Anisotropic behaviour of transmission through thin superconducting NbN film in parallel magnetic field, Physica C **533** (2017) 154 - 157.

3. M. Šindler, R. Tesař, J. Koláček, P. Szabó, P. Samuely, V. Hašková, C. Kadlec, F. Kadlec, P. Kužel, Far-infrared electrodynamics of thin superconducting NbN film in magnetic fields, Supercond. Sci. Tech. 27 (2014) 05500(1) - 05500(8).

4. M. Šindler, R. Tesař, J. Koláček, L. Skrbek, Interpretation of transmission through type II superconducting thin film on dielectric substrate as observed by laser thermal spectroscopy, Physica C **483** (2012) 127 - 135.

5. R. Tesař, M. Šindler, K. Il'in, J. Koláček, M. Siegel and L. Skrbek, Terahertz thermal spectroscopy of a NbN superconductor, Phys. Rev. B **84** (2011) 132506(1) - 132506(4).

6. R. Tesař, J. Koláček, Z. Šimša, M. Šindler, L. Skrbek, K. Il'in, M. Siegel, Terahertz transmission of NbN superconductor thin film, Physica C **470** (2010) 932 - 934.

7. M. Šindler, R. Tesař, J. Koláček, L. Skrbek, Z. Šimša, Far-infrared transmission of a superconducting NbN film, Phys. Rev. B **81** (2010) 184529(1) - 184529(5).